Title
A Computational Stress-Deformation Analysis of Arterial Wall Tissue

Author
Krone, Ryan Taylor

Publication Date
2010

A Computational Stress-Deformation Analysis of Arterial Wall Tissue

by

Ryan Taylor Krone

A dissertation submitted in partial satisfaction of the
requirements for the degree of
Doctor of Philosophy

in

Mechanical Engineering

in the

GRADUATE DIVISION
of the
UNIVERSITY OF CALIFORNIA, BERKELEY

Committee in charge:
Professor David Steigmann, Co-chair
Professor Tarek Zohdi, Co-chair
Professor John Strain

Fall 2010

A Computational Stress-Deformation Analysis of Arterial Wall Tissue

Abstract

A Computational Stress-Deformation Analysis of Arterial Wall Tissue

by

Ryan Taylor Krone
Doctor of Philosophy in Mechanical Engineering

University of California, Berkeley

Professor David Steigmann, Co-chair
Professor Tarek Zohdi, Co-chair

Understanding the mechanical behavior of arterial walls under various physiological loading and boundary conditions is essential for achieving the following: (1) improved therapeutics that are based on mechanical procedures (e.g. arterial segmenting and suturing), (2) study of mechanical factors that may trigger the onset of arterial aneurysms (i.e. focal blood-filled dilatations of the vessel wall caused by disease) and (3) investigations on tissue variations due to health, age, hypertension and atherosclerosis, all of which hold immense clinical relevance. In general, the physiological conditions on an any arterial segment can include axial stretch, torsional twist and transmural (internal, radial) pressure which often provoke large wall-tissue deformations that require theories of continuum hyperelasticity. Further, the presence of collagen fibers throughout the two structural layers (media, adventitia) of the arterial wall require anisotropic strain energy functions for more histological accurate models. Nonlinear computational methods are therefore essential for this class of boundary-value-problems (BVPs) which often do not contain closed-form solutions.

We begin by modeling the arterial vessel wall as a thin sheet in the form of a circular cylinder in the reference configuration. We seek to employ a bio-type strain energy function on this constitutive framework to investigate the onset of non-linear instabilities in a thin-walled, hyperelastic tube under (remote) axial stretch and internal pressure. Viscoelastic effects are also considered in this model. We then build to investigating the effects of various combinations of axial stretch and transmural pressure on the global deformation and through-thickness stress and strain fields of an arterial segment modeled as a two-layer, fiber-reinforced composite and idealized as a thick-walled cylinder in the reference configuration. We further consider (in both models) the presence of local tissue lesions, or portions of the arterial wall having either stiffer (i.e. thrombosis or scar tissue) or softer (i.e. diseased tissue) material characteristics, relative to the surrounding tissue. We account for this by appropriately scaling the elastic constants of the strain energy

functions for regions with a lesion and without. For the three-dimensional model, we employ the strain energy function of Holzapfel et al. [1] which has been modified by constraints on the principal invariants by Balzani et al. [2] in order to ensure material polyconvexity. We choose a particular vessel, the human common carotid (HCC) artery, with appropriate geometric and material properties found from various experimentally-based studies (e.g. Fung et al. [3]). We focus on distinct elastic constants for each layer (media, adventitia) that have been obtained through biaxial (i.e. not simply uniaxial data - reasons for this are discussed later) testing of *in vitro* HCC arteries. The loading conditions are combinations of axial extension and transmural pressure, in the presence and absence of material lesions. The loading is consistent with *in vivo* conditions on a general segment of the vessel wall.

We find that as a two-dimensional surface, the overall deformation from internal pressure (i.e. the bulge) depends on the magnitude and, more importantly, the *rate* of axial stretch and transmural pressure, the elastic material parameters of the bio-strain energy function, and of course local inhomogeneities in the material description of the tissue. When modeled as a three-dimensional solid undergoing pure axial stretch, the majority of the stress is in the medial tissue, which displays a significant gradient in the axial direction, whereas the stress in the adventitia is constant throughout the length of the vessel. For supra-physiological pressures (i.e. 20-30 kPa, or about 50% higher than *in-vivo* conditions) the adventitia contributes to the load sharing and the gradient in the medial layer evens out. For narrow (2% of the length), stiff (100x stiffer than surrounding tissue), ring-like lesions under the same pressures and axial stretch, the overall vessel deformation is considerably smaller in the radial direction. The overall segment shape is stabilized by this type of material abnormality. For local spot-like stiff (100x stiffer than surrounding tissue) lesions, the deformation leads to an inward bulge (i.e. a clot) that will likely affect fluid flow characteristics, hence growth and remodeling of the tissue at the wall. For these loading conditions, when the spot-like and ring-like lesions are approximately two-times *softer* than the surrounding tissue, no significant differences appear in the stress and strain fields.

Contents

List of Figures

List of Tables

Acknowledgments

I would like to thank professor David Steigmann and professor Tarek Zohdi for their patient and informed guidance on this project. Also, to the FAA, Powley Fund and Army for their support. My lab mates Doron Klepach, George Mseis and Matthew Barham for saving me many hours of debugging in providing me sanity-checks and brainstorming support at essential moments of mental stagnation. My father Gary for supporting me emotionally during this long, difficult journey of six years of concurrent school and work as a mechanical engineer at LLNL. The culmination of this work and degree would not have been possible without his consistent love, advise and support. And my mother Pamela, who through a long and courageous battle with leukemia, inspired me to simply endure, work harder than I ever thought I could, and maintain a positive attitude in achieving my goal of a PhD in mechanical engineering from UC Berkeley.

Chapter 1

Introduction

That mechanics plays crucial role in cardiovascular health and disease has been known for centuries (e.g. see Roy [9]), though it has been only since the mid-1970's that we have understood the importance of wall stresses in predicting the development and influences of vessel wall lesions (e.g. local abnormalities in the vessel wall). Most stress analyses have assumed idealized geometries, i.e. an axisymmetric, uniform-wall cylinder, and are generally based on either Laplace's equation of $\sigma = \frac{Pr}{2t}$, where, σ is the uniform in-plane wall Cauchy stress, P is the transmural (internal, radial) pressure, r the pressurized inner-radius and t the associated wall thickness (see McGiffin et al. [10]; Marston et al. [11]), axisymmetric membrane theory (e.g. Elger et al. [12]; Fu et al. [13]) or linear-elastic finite element analyses (see Di et al. [14]; Elger et al. [12]; Wang et al. [15]; Stringfellow et al. [16]; Inzoli et al. [17]; Vorp et al. [18]; Mower et al. [19]). As biological tissue has inherent nonlinear material behavior and encounters large strains on the order of 20-40% (see He and Roach [20]; Raghaven et al. [21]), linear analyses are clearly inappropriate and only in more recent years has there been efforts to employ nonlinear finite element methods for their analysis. Until recently, the most accurate models use patient-specific geometry (Fillinger et al. [22]; Raghavan et al. [23]) and treat the arterial wall as nonlinearly elastic, albeit isotropic, homogeneous, uniformly thick and incompressible.

More recently have authors incorporated anisotropy into the material response of the artery wall. Vande Geest et al. [6] proposed a Choi-Vito-type, two-dimensional phenomenological model obtained from biaxial tests on a series of human aortic samples. This exponential strain energy function assumes two in-plane (of the tissue wall) preferred directions; longitudinal and circumferential. Another phenomenological and exponential-type, anisotropic strain energy function is proposed by Chuong and Fung [7] and [24] which adds a third preferred direction to the material response by including the radial, through-thickness strain. Holzapfel et al. [1] introduces a more physiologically-accurate approach by modeling the arterial tissue as a thick-walled, fiber-reinforced composite thereby including the effects of the helically arranged collagen fibers in both the medial and adventitia layers. They further propose an additive decomposition of the invariant-based strain energy function into isotropic and anisotropic terms. The Holzapfel et al. model [1] is transversely isotropic in that the matrix, or ground-substance of the wall tissue (elastin) is treated as an isotropic continuum and the in-plane, helically symmetric collagen fibers are accounted for with structural tensors. Balzani et al. [2] modifies the Holzapfel model by developing conditions on the principal deformation invariants that make the transversely isotropic strain energy function polyconvex (i.e. convex in all of it's deformation arguments). The fiber-reinforced, thick-walled, two-layer cylinder proposed by Holzapfel et al. [8] and augmented by Balzani et al. [2] is the model used in the second part of this study. For a general introduction to the invariant formulation of anisotropic strain energy functions with isotropic tensor functions see e.g. Boehler [25] and for more specific model problems see e.g. Schröder [26]. Theoretical, experimental and clinical principles related to arteries can be found in the text by Nichols and O'Rourke [27]. For the most comprehensive sources on the general theories of cardiovascular solid mechanics, specifically arterial wall mechanics, the reader is referred to the texts by Humphrey [28] and Fung [29].

In this study, we present the following two models of an arterial wall under various deformation states:

1. A two-dimensional membrane formulation suitable for rate-dependent axial stretch and pressure-driven stability analyses. This model employs a more idealized mathematical model of the arterial wall (i.e. as an arbitrarily thin sheet) with simpler numerical methods (i.e. finite difference methods applied to a one-dimensional nodal network). It's primary utility is a more numerically-simple, hence a possibly more physically insightful, approach to investigating rate, stretch and pressure-driven material instabilities that lead to large deformations in the arterial wall with a hyperelastic, isotropic, incompressible bio-strain energy function. Physical (as opposed to numerical) viscoelastic parameters are included in this model.

2. A three-dimensional, two-layer (media, adventitia), fiber-reinforced composite model under the dynamic response of both uniaxial stretch and transmural pressure. We further investigate the time-dependent overall vessel deformation and wall stress and strain fields in the presence of local material inhomogeneities (or "lesions") characterized by locally stiff or soft portions of the tissue wall (i.e. modeling, for example, scared or diseased tissue). We use a hyperelastic, transversely isotropic, polyconvex strain energy function (proposed by Holzapfel et al. [1] and made polyconvex by Balzini et al. [2]) that describes two-families of helically arranged fibers in each layer of the

tissue wall. This material model is clearly a more physiologically-accurate representation of the matrix of elastin and embedded collagen fibers in each structural layer of the arterial wall. We employ a numerically robust nonlinear total Lagrange formulation (i.e. over the reference configuration of the body) of finite element method with each constituent layer (media, adventitia) having a *unique* numerical meshing. We do not account for the presence of residual wall stresses in this study; ,i.e., the reference configuration is both load and stress-free (reasons for which are discussed later).

Chapter 2

Arterial Histology

The microstructure of the arterial wall varies with the location along the arterial tree, age, species and disease; therefore, it is necessary to focus on a particular vessel and condition of interest. Nevertheless, the mechanical analysis of one particular class of vessels yields both specific and detailed information but also a more general philosophical approach to theoretical investigation that may be useful throughout cardiovascular solid mechanics. Given this, arteries can be categorized into two major groups: *elastic arteries* (e.g. the aorta, main pulmonary arteries, common carotids (the vessel of interest in this study - see Fig. 2.1), common iliac, etc.) and *muscular arteries* (e.g. the coronaries, cerebrals, femoral and renal arteries, etc.) - see Rhodin [30] . Elastic arteries tend to be larger diameter vessels located closer to the heart, whereas muscular arteries are most distally located and smaller in diameter. Regardless of type, the normal arterial wall consists of three layers: the intima, media and adventitia. The innermost layer, or intima, consists of a monolayer of subendothelial cells attached to a membrane (approximately 0.2 - 0.5 μm thick) composed of mainly type IV collagen and laminin; the middle layer, or media, consists of smooth muscle cells embedded in an extracellular matrix of elastin, multiple types of collagen (types I, III and V) and proteoglycans; the outermost layer consists of fibroblasts embedded in an extensive diagonally-to-axially oriented type I collagen, admixed elastic fibers, nerves and in some cases its own vasculature. It is thought that the adventitia serves, in part, as a protective sheath that prevents acute over-distension of the media (as with all muscle, smooth muscle contracts with maximum force at a certain length; above or below which the contractions are less forceful). It is generally accepted that due to the relative thinness and make-up of the intimal layer, only the media and adventitia contribute to the *structural* behavior of the artery (neglecting growth, remodeling and chemo-dynamic effects). Therefore, the three-dimensional model we will employ is a two-layered structure composed of only the media and adventitia layers. Fig. 2.2 shows the physiology and constituents of a typical artery.

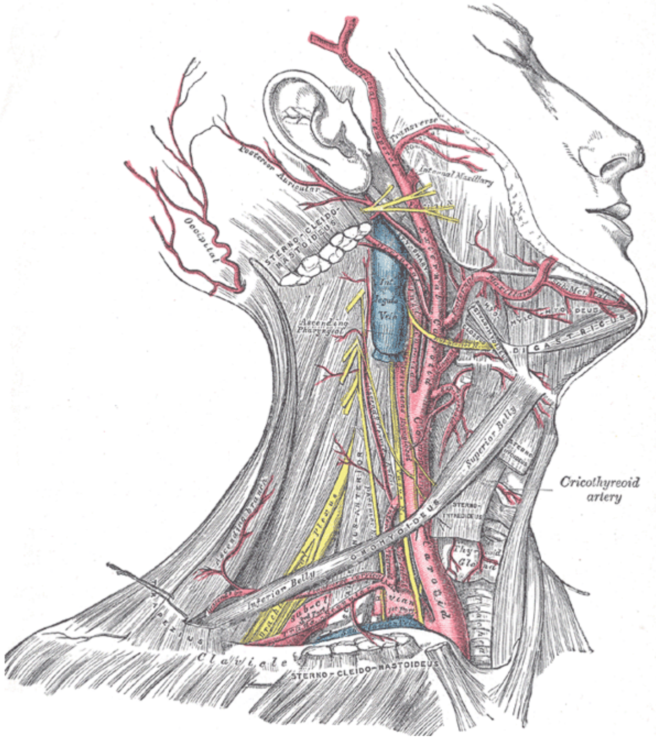

Figure 2.1: Human Common Carotid (HCC) Artery (copied from Gray's Anatomy, [4])

This investigation will focus primarily on a representative, though idealized, section of the Human Common Carotid (HCC) artery (*A. Corotis Communis*); the principal arteries that supply blood to the head and neck (Fig. 2.1). We will investigate the vessel behavior under large deformations that are induced by various combinations of transmural pressure and axial and stretch.

The material models (i.e. hyperelastic strain energy functions) for aortic tissue used in this study have been extracted from the literature and are constructed from basic principals of hyperelastic continuum mechanics. In other words, the strain energy functions used here are *not* specific to the actual microstructure of the tissue, rather are based on first principals of continuum mechanics and regression of experimental data (for the material constants). Although the material models may not conform to the tissue microstructure, they provide simple and approximate descriptions of the material behavior and can be applied to three-dimensional stress analyses. Many previous researchers in vascular mechanics have applied this approach (e.g. Fung et al. [31]; Vaishnav et al. [32]; Vito et al. [33]; Vorp et al. [34]).

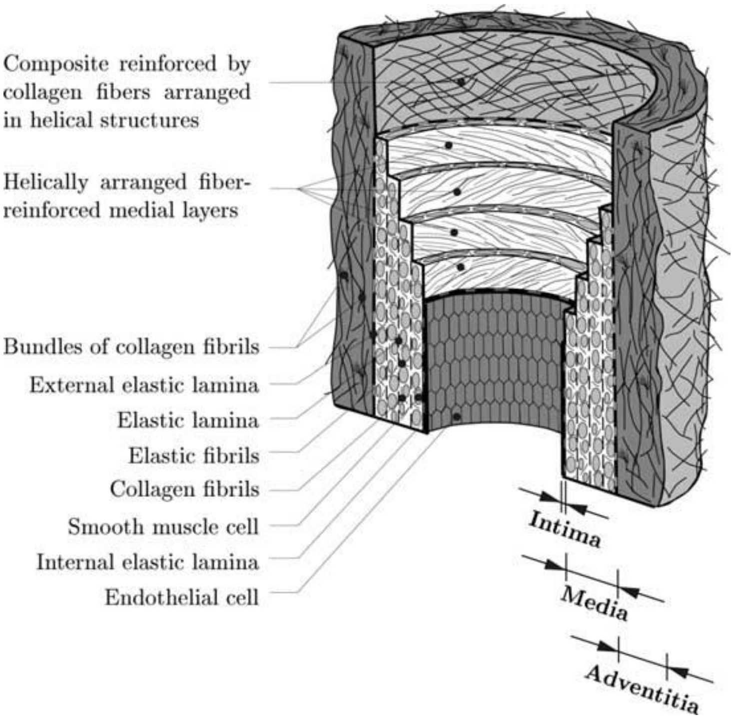

Figure 2.2: Physiology of the arterial wall (copied from Holzapfel et al. [1])

Chapter 3

The Arterial Wall as a Thin Sheet

As a building block to understanding the full three-dimensional behavior of an artery, we begin by modeling the arterial vessel wall as a two-dimensional mathematical surface (i.e. membrane or thin sheet). We seek to employ a bio-type strain energy function on this constitutive framework to investigate the onset of nonlinear instabilities in a thin-walled, hyperelastic tube under (remote) axial stretch and internal pressure. We then investigate the conditions in which a bifurcation of the mechanical stability leads to a bulge of the vessel wall. This model clearly can not capture the geometric contributions to instabilities of a three-dimensional body (e.g. Euler buckling), however, it leads to simpler numerical methods and is useful in testing various bio-type strain energy functions.

The mathematical framework for our first model assumes the following:

- A two-Dimensional thin sheet formed as a circular cylinder in the reference configuration
- Plain stress conditions
- Rate-dependent (viscoelastic and physical) stress response to in-plane strain
- An isotropic, hyperelastic, polyconvex bio-strain energy function

The numerical method for this model uses the following:

- The finite-difference method applied to a one-dimensional network of nodes that is revolved to form an axisymmetric tube
- A novel spatial midpoint method that provides adequate numerical stability and high accuracy
- A fixed-point time-iteration whereby a specified tolerance is met before advancing to the next time step

3.1 Two-Dimensional Constitutive Framework

Consider a membrane wrapped into a right circular cylinder (note this is a *developable surface* where no strain is required to unravel or flatten the surface back out; in other words the reference configuration is stress-free). Also consider a convected coordinate system on the surface of the cylinder, say $\{\theta^{\alpha}\}$, where $\alpha = 1, 2$ and $\theta^1 = \theta, \theta^2 = z$.

A material point on the surface in the reference configuration Ω_o is parametrized by the following,

$$\mathbf{R}\left(\theta, z\right) = R\mathbf{e_r}\left(\theta\right) + z\mathbf{k} \tag{3.1}$$

The same material point in the current configuration is then parameterized by the following (see Fig. (3.1)),

$$\mathbf{r}\left(\theta, z\right) = r(z)\mathbf{e_r}\left(\theta\right) + \zeta(z)\mathbf{k} \tag{3.2}$$

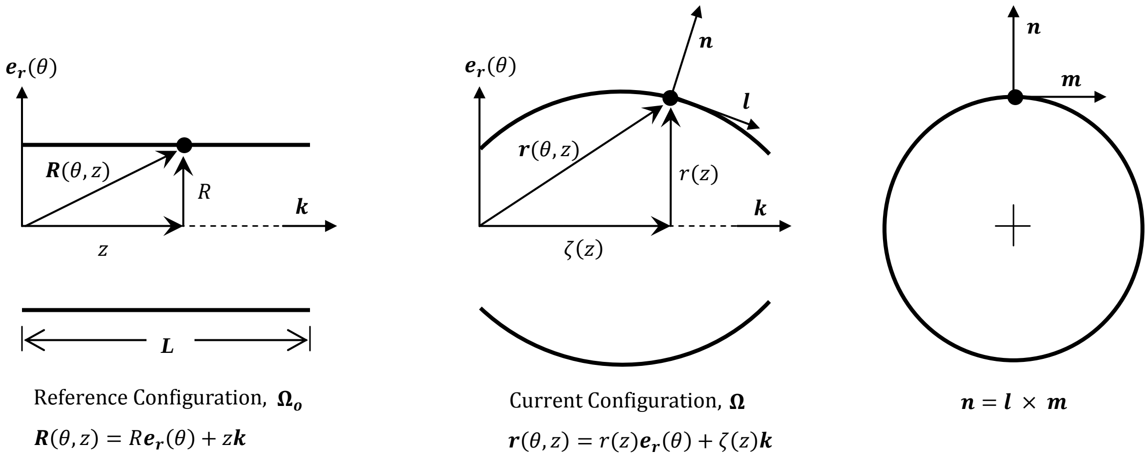

Figure 3.1: 2D membrane coordinates

Define a set of "contravariant" bases, characterized by (3.1), on the *undeformed* surface as,

$$\mathbf{A}_1 = \frac{\partial \mathbf{R}}{\partial \theta^1} = \frac{\partial \mathbf{R}}{\partial \theta} = R\frac{\partial \mathbf{e_r}(\theta)}{\partial \theta} = R\mathbf{e}_{\theta} \tag{3.3}$$

$$\mathbf{A}_2 = \frac{\partial \mathbf{R}}{\partial \theta^2} = \frac{\partial \mathbf{R}}{\partial z} = \mathbf{k} \tag{3.4}$$

Define the dual set of "covariant" bases to our contravariant bases, on the same surface (these vectors have inverse components to the contravariant basis vectors), as,

$$\mathbf{A}^1 = \frac{1}{R}\mathbf{e}_\theta \tag{3.5}$$

$$\mathbf{A}^2 = \mathbf{k} \tag{3.6}$$

The dot product of these bases form a set of scalars for which the components are, $A_{\alpha\beta}$ and $A^{\alpha\beta}$, respectively (where $\alpha,\beta = 1,2$), are defined as $A_{\alpha\beta} \equiv \mathbf{A}_\alpha \cdot \mathbf{A}_\beta$ and $A^{\alpha\beta} \equiv \mathbf{A}^\alpha \cdot \mathbf{A}^\beta$.

Similarly, on the surface in the deformed configuration, where a material point is parameterized by (3.2), we have the transformed contravariant bases,

$$\mathbf{a}_1 = \frac{\partial \mathbf{r}}{\partial \theta^1} = \frac{\partial \mathbf{r}}{\partial \theta} = r\frac{\partial \mathbf{e}_\mathbf{r}(\theta)}{\partial \theta} = r\mathbf{e}_\theta \tag{3.7}$$

$$\mathbf{a}_2 = \frac{\partial \mathbf{r}}{\partial \theta^2} = \frac{\partial \mathbf{r}}{\partial z} = r'(z)\mathbf{e}_\mathbf{r}(\theta) + \zeta'(z)\mathbf{k} \tag{3.8}$$

Where the covariant bases are then,

$$\mathbf{a}^1 = \frac{1}{r}\mathbf{e}_\theta \tag{3.9}$$

$$\mathbf{a}^2 = \frac{1}{r'(z)}\mathbf{e}_\mathbf{r}(\theta) + \frac{1}{\zeta'(z)}\mathbf{k} \tag{3.10}$$

Similarly, we have the following set of scalars from the dot products of our current configuration bases, $a_{\alpha\beta} \equiv \mathbf{a}_\alpha \cdot \mathbf{a}_\beta$ and $a^{\alpha\beta} \equiv \mathbf{a}^\alpha \cdot \mathbf{a}^\beta$.

For deformations in-plan of our surface, we can define the two-dimensional deformation gradient as the following,

$$\begin{aligned}
\mathbf{f} &\equiv \mathbf{a}_\alpha \otimes \mathbf{A}^\alpha \\
&= \mathbf{a}_1 \otimes \mathbf{A}^1 + \mathbf{a}_2 \otimes \mathbf{A}^2 \\
&= r\mathbf{e}_\theta \otimes \frac{1}{R}\mathbf{e}_\theta + (r'(z)\mathbf{e}_\mathbf{r}(\theta) + \zeta'(z)\mathbf{k}) \otimes \mathbf{k} \\
&= \frac{r}{R}\mathbf{e}_\theta \otimes \mathbf{e}_\theta + (r'(z)\mathbf{e}_\mathbf{r}(\theta) + \zeta'(z)\mathbf{k}) \otimes \mathbf{k} \qquad (3.11)
\end{aligned}$$

It is useful to further define an orthogonal basis at our material point in the reference configuration as $\{\mathbf{L}, \mathbf{M}, \mathbf{N}\}$ and current configuration as $\{\mathbf{l}, \mathbf{m}, \mathbf{n}\}$ (see Fig. (3.1)). In the reference and current configurations, respectively, $\mathbf{L}$ and $\mathbf{l}$ point along the surface in the longitudinal direction of the cylinder, $\mathbf{M}$ and $\mathbf{m}$ point along the meridian of the cylinder (i.e. tangent at a material point around the circumference) and **N** and **n** are the outward unit normals to the surface.

We can define the deformed orthogonal basis vectors that lie in the surface (**l** and **m**) as some scalar multiple (say λ and μ, respectively) of our contravariant bases,

$$\lambda \mathbf{l} = r'(z)\mathbf{e_r}(\theta) + \zeta'(z)\mathbf{k} \tag{3.12}$$

$$\mu \mathbf{m} = \frac{r}{R}\mathbf{e}_\theta \tag{3.13}$$

Therefore, we can represent the 2D deformation gradient (noting that in the reference configuration, $\mathbf{M} = \mathbf{e_r}$ and $\mathbf{L} = \mathbf{k}$) as the following,

$$\mathbf{f} = \mu\mathbf{m} \otimes \mathbf{M} + \lambda\mathbf{l} \otimes \mathbf{L} \tag{3.14}$$

We further identify the hoop and longitudinal stretches, respectively, as,

$$\mu = \frac{r}{R} \tag{3.15}$$

$$\lambda = ((r'(z))^2 + (\zeta'(z))^2)^{1/2} \tag{3.16}$$

It is useful to define the outward unit normal for a material point in the current configuration using the following relationship,

$$J\mathbf{n} = \mu\mathbf{m} \times \lambda\mathbf{l} \tag{3.17}$$

Where, J is the Jacobian of the deformation (i.e. $J = \mu\lambda = [det(\mathbf{F}^T\mathbf{F})]^{1/2}$). It will be useful later to have this relationship expressed in the following form,

$$\begin{aligned} J\mathbf{n} &= \mu\mathbf{m} \times \lambda\mathbf{l} \\ &= \frac{r}{R}\mathbf{e}_\theta \times (r'(z)\mathbf{e_r} + \zeta'(z)\mathbf{k}) \\ &= -\frac{r}{R}r'(z)\mathbf{k} + \frac{r}{R}\zeta'(z)\mathbf{e_r} \\ &= \frac{r}{R}(\zeta'(z)\mathbf{e_r} - r'(z)\mathbf{k}) \\ &= \mu(\zeta'(z)\mathbf{e_r} - r'(z)\mathbf{k}) \end{aligned} \tag{3.18}$$

To avoid dealing with different systems of units, we will non-dimensionalize the problem by dividing through by the reference configuration radius, R. Recalling the [already] dimensionless radial coordinate, $\mu = \frac{r}{R}$, we further define a dimensionless axial coordinate (say x) in the reference configuration and a dimensionless axial stretch (say $\bar{\zeta}$) in the current configuration, respectively, as the following,

$$x = \frac{z}{R} \tag{3.19}$$

$$\bar{\zeta} = \frac{\zeta}{R} \tag{3.20}$$

Since the formulation of our equilibrium equations involves the derivative with respect to the undeformed axial coordinate (which has dimensions of length), z, it is useful to check the derivatives of the new dimensionless quantities.

$$r'(z) = \frac{dr}{dz} = \frac{dr}{dx}\frac{dx}{dz} = \frac{d(\mu R)}{dx}\frac{1}{R} = \frac{d\mu}{dx} = \mu'(x) \tag{3.21}$$

$$\zeta'(z) = \frac{d\zeta}{dz} = \frac{d\zeta}{dx}\frac{dx}{dz} = \frac{d(\bar{\zeta} R)}{dx}\frac{1}{R} = \frac{d\bar{\zeta}}{dx} = \bar{\zeta}'(x) \tag{3.22}$$

So clearly, $r'(z) = \mu'(x)$ and $\zeta'(z) = \bar{\zeta}'(x)$. Also, it is useful to note the dimensionless form of the longitudinal stretch as, $\lambda = ((\mu')^2 + (\bar{\zeta}')^2)^{1/2}$. Henceforth, consider derivatives marked with a prime to have the definition $(\,)' \equiv \frac{d(\,)}{dx}$.

3.2 Three-Dimensional Constitutive Framework

To motivate the forthcoming definition of our two-dimensional stress measures, we will briefly review the fundamental concepts of three-dimensional non-linear continuum mechanics.

3.2.1 Deformation

Let $\Omega_0 \subset \Re^3$ be an open set defining a continuum body (an arterial layer) with smooth, continuous boundary surface $\partial\Omega_0$ in three-dimensional Euclidean space $\Re^3$. We refer to Ω_0 as the reference configuration of the body at fixed reference time, $t = 0$. The body undergoes a motion χ during some closed time interval, $t \in [0, T]$. The motion is expressed via the mapping $\chi : \widetilde{\Omega_0} \times [0, T] \rightarrow \Re^3$, where $\widetilde{\Omega_0} = \Omega_0 \cup \partial\Omega_0$ denotes the closure of the open set, Ω_0. The motion transforms a reference point $\mathbf{X} \in \widetilde{\Omega_0}$ into a spatial point $\mathbf{x} = \chi(\mathbf{X}, t) \in \widetilde{\Omega}$ for any subsequent time, where of course $\widetilde{\Omega} = \Omega \cup \partial\Omega$. The motion therefore gives $\chi(\mathbf{X}, t) = \mathbf{X} + \mathbf{u}(\mathbf{X}, t)$, with the Lagrangian description of the displacement field $\mathbf{u}(\mathbf{X}, t)$. Further, we define the three-dimensional deformation gradient $\mathbf{F}(\mathbf{X}, t) = \partial\chi(\mathbf{X}, t)/\partial\mathbf{X} = \mathbf{I} + \partial\mathbf{u}/\partial\mathbf{X}$ which describes the deformation of a material line element (otherwise defined as $d\mathbf{x} = \mathbf{F}d\mathbf{X}$, where the material line segment $d\mathbf{X}$, tangent at a material point to the curve C_o in the reference configuration, is mapped to the current material line segment $d\mathbf{x}$, tangent to the deformed curve, C) and the Jacobian, $J(\mathbf{X}, t) = det\mathbf{F}$ which characterizes the volume change due to the deformation (see Figure 3.2).

Since we wish to use the Lagrangian description of the constitutive model, an appropriate deformation tensor is the right Cauchy-Green tensor $\mathbf{C}(\mathbf{X}, t) = \mathbf{F}^T\mathbf{F}$.

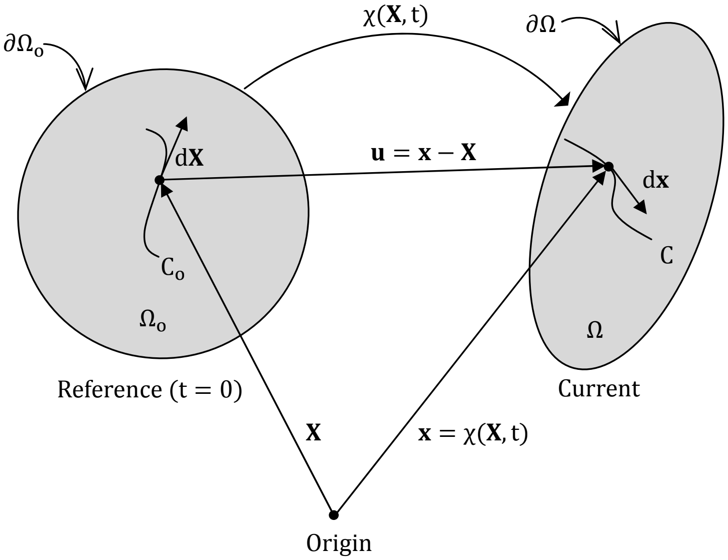

Figure 3.2: Deformation diagram

3.2.2 Stresses and the Viscoelastic Response

The first Piola-Kirchhoff, in-plane stresses (i.e. the principal stresses) for our hyperelastic, incompressible, isotropic material are traditionally found by taking the derivative of the strain energy density with respect to each of the principal stretches. Since, by definition of a viscoelastic material, we seek an expression of stress that is strain-rate dependent, we will modify our stresses by simply adding a term that is rate-dependent (allowed by superposition).

First we postulate a hyperelastic *three-dimensional* incompressible, isotropic, and strain-rate sensitive material then we will project this onto our two-dimensional surface. We assume the following constitutive function for the nominal stress (suspend standard summation convention for repeated indices and simply note that $i = 1, 2$ or 3),

$$\hat{\mathbf{P}} = \sum_{i=1}^{3} \frac{\partial \bar{W}(\lambda_1, \lambda_2, \lambda_3)}{\partial \lambda_i} \mathbf{v}_i \otimes \mathbf{u}_i - q\mathbf{F}^* + \frac{1}{2}\bar{\nu}\mathbf{F}\dot{\mathbf{C}} \tag{3.23}$$

Notice that we have introduced a dimensionless strain energy density, $\bar{W}$, that depends on all three generalized principal stretches, λ_1, λ_2 and λ_3. Our dimensionless Lagrange multiplier, $-q$, coupled with $\mathbf{F}^*$ incorporates our incompressibility constraint. We use $\bar{\nu}$ to represent our dimensionless kinematic viscosity (a constant), where $\nu = G\bar{\nu}$ and again, G is the shear modulus (note that for ν, in 3D and 2D, respectively, the units are mass/(length*time) and mass/time). We can define our 3D deformation gradient and it's cofactor, respectively, as,

$$\mathbf{F} = \sum_{i=1}^{3} \lambda_i \mathbf{v}_i \otimes \mathbf{u}_i \tag{3.24}$$

and,

$$\mathbf{F}^* = \sum_{i=1}^{3} \mu_i \mathbf{v}_i \otimes \mathbf{u}_i \tag{3.25}$$

Where, $\mu_1 = \lambda_2\lambda_3$, $\mu_2 = \lambda_1\lambda_3$ and $\mu_3 = \lambda_1\lambda_2$.

We define the right Cauchy stretch tensor and its time derivative (provided $\dot{\mathbf{u}}_i = \mathbf{0}$), respectively as,

$$\mathbf{C} = \mathbf{F}^T\mathbf{F} = \sum_{i=1}^{3} \lambda_i^2 \mathbf{u}_i \otimes \mathbf{u}_i \tag{3.26}$$

$$\dot{\mathbf{C}} = 2\sum_{i=1}^{3} \lambda_i \dot{\lambda}_i \mathbf{u}_i \otimes \mathbf{u}_i \tag{3.27}$$

Combining terms yields,

$$\hat{\mathbf{P}} = \sum_{i=1}^{3} \left(\frac{\partial \bar{W}(\lambda_1, \lambda_2, \lambda_3)}{\partial \lambda_i} - q\mu_i + \bar{\nu}\lambda_i^2\dot{\lambda}_i \right) \mathbf{v}_i \otimes \mathbf{u}_i \tag{3.28}$$

According to our formulation of plane stress (i.e. our membrane model), we know that the stress in the direction normal to the surface, say the $\mathbf{u}_3$-direction, is zero which can be expressed by $\hat{\mathbf{P}}\mathbf{u}_3 = \mathbf{0}$. Substituting (3.28) into this condition yields a useful relation,

$$\begin{aligned}\left(\left(\frac{\partial \bar{W}(\lambda_1,\lambda_2,\lambda_3)}{\partial \lambda_3} - q\mu_3 + \bar{\nu}\lambda_3^2\dot{\lambda_3}\right)\mathbf{v}_3 \otimes \mathbf{u}_3\right)\mathbf{u}_3 &= \mathbf{0} \\ \frac{\partial \bar{W}(\lambda_1,\lambda_2,\lambda_3)}{\partial \lambda_3} = q\mu_3 - \bar{\nu}\lambda_3^2\dot{\lambda_3} & \end{aligned} \tag{3.29}$$

Since we seek the "new"(i.e. viscoelastic) in-plane principle stresses, it is useful to first define a 2D identity tensor as the 3D identity tensor minus the out-of-plane tensor component, or,

$$\mathbf{1} = \mathbf{I} - \mathbf{k} \otimes \mathbf{k} \tag{3.30}$$

Again, from plane stress (i.e. $\hat{\mathbf{P}}\mathbf{k} = \mathbf{0}$), we can say the following,

$$\begin{aligned}\hat{\mathbf{P}} &= \hat{\mathbf{P}}\mathbf{I} \\ &= \hat{\mathbf{P}}\mathbf{1} + \hat{\mathbf{P}}\mathbf{k} \otimes \mathbf{k} \\ &= \hat{\mathbf{P}}\mathbf{1}\end{aligned} \tag{3.31}$$

Forming this product gives the following,

$$\hat{\mathbf{P}}\mathbf{1} = \sum_{\alpha=1}^{2}\left(\frac{\partial \bar{W}(\lambda_1,\lambda_2,\lambda_3)}{\partial \lambda_\alpha} - q\mu_\alpha + \bar{\nu}\lambda_\alpha^2\dot{\lambda_\alpha}\right)\mathbf{v}_\alpha \otimes \mathbf{u}_\alpha \tag{3.32}$$

Due to incompressibility, we can equate $\bar{W}(\lambda_1,\lambda_2,\lambda_3)$ to some other arbitrary strain energy density that is only a function of the first two (generalized) principal stretches,

$$\bar{W}(\lambda_1,\lambda_2,\lambda_3) = \bar{\omega}(\lambda_1,\lambda_2) \;\; with \;\; \lambda_3 = \left(\lambda_1\lambda_2\right)^{-1} \tag{3.33}$$

Using (3.29), we can show the following,

$$\begin{aligned}\frac{\partial\bar{\omega}}{\partial\lambda_1} &= \frac{\partial\bar{W}}{\partial\lambda_1}+\left(\frac{\partial\bar{W}}{\partial\lambda_3}\right)\left(\frac{\partial\lambda_3}{\partial\lambda_1}\right)\\ &= \frac{\partial\bar{W}}{\partial\lambda_1}+\left(q\mu_3-\bar{\nu}\lambda_3^2\dot{\lambda}_3\right)\left(\frac{-1}{\lambda_1^2\lambda_2}\right)\\ &= \frac{\partial\bar{W}}{\partial\lambda_1}-\frac{q}{\lambda_1}+\left(\frac{\bar{\nu}}{\lambda_1^2\lambda_2}\right)\lambda_3^2\dot{\lambda}_3 \qquad (3.34)\end{aligned}$$

Using the same development, the second in-plane stress is the following,

$$\begin{aligned}\frac{\partial\bar{\omega}}{\partial\lambda_2} &= \frac{\partial\bar{W}}{\partial\lambda_2}+\left(\frac{\partial\bar{W}}{\partial\lambda_3}\right)\left(\frac{\partial\lambda_3}{\partial\lambda_2}\right)\\ &= \frac{\partial\bar{W}}{\partial\lambda_2}+\left(q\mu_3-\bar{\nu}\lambda_3^2\dot{\lambda}_3\right)\left(\frac{-1}{\lambda_1\lambda_2^2}\right)\\ &= \frac{\partial\bar{W}}{\partial\lambda_2}-\frac{q}{\lambda_2}+\left(\frac{\bar{\nu}}{\lambda_1\lambda_2^2}\right)\lambda_3^2\dot{\lambda}_3 \qquad (3.35)\end{aligned}$$

Therefore, in general,

$$\frac{\partial\bar{W}}{\partial\lambda_\alpha}=\frac{\partial\bar{\omega}}{\partial\lambda_\alpha}+\frac{q}{\lambda_\alpha}-\frac{\bar{\nu}}{\lambda_\alpha}\lambda_3\dot{\lambda}_3 \qquad (3.36)$$

Hence, if we plug (3.36) into (3.32) with some manipulation we obtain the in-plane viscoelastic stress tensor components $\hat{P}_\alpha$ of the tensor $\hat{\mathbf{P}}$ as,

$$\begin{aligned}\hat{P}_\alpha &= \frac{\partial\bar{\omega}}{\partial\lambda_\alpha}+\frac{q}{\lambda_\alpha}-q\mu_\alpha+\bar{\nu}\lambda_\alpha^2\dot{\lambda}_\alpha-\frac{\bar{\nu}}{\lambda_\alpha}\lambda_3\dot{\lambda}_3\\ &= \frac{\partial\bar{\omega}}{\partial\lambda_\alpha}+\frac{\bar{\nu}}{\lambda_\alpha}\left(\lambda_\alpha^3\dot{\lambda}_\alpha-\lambda_3\dot{\lambda}_3\right) \qquad (3.37)\end{aligned}$$

Where,

$$\hat{\mathbf{P}}=\sum_{\alpha=1}^{2}\hat{P}_\alpha\mathbf{v}_\alpha\otimes\mathbf{u}_\alpha \qquad (3.38)$$

It is useful to note the following,

$$\dot{\lambda}_3 = \dot{\overline{\left(\lambda_1\lambda_2\right)}}^{-1}\left(\dot{\lambda}_1\lambda_2 + \lambda_1\dot{\lambda}_2\right) \tag{3.39}$$

Therefore, to specialize this result using our previous notation, we substitute $\lambda_1 = \mu$ and $\lambda_2 = \lambda$, so the two principal stresses are,

$$\hat{P}_1 = \frac{\partial\bar{\omega}}{\partial\mu} + \frac{\bar{\nu}}{\mu}\left(\mu^3\dot{\mu} - \lambda_3\dot{\lambda}_3\right) \tag{3.40}$$

and,

$$\hat{P}_2 = \frac{\partial\bar{\omega}}{\partial\lambda} + \frac{\bar{\nu}}{\lambda}\left(\lambda^3\dot{\lambda} - \lambda_3\dot{\lambda}_3\right) \tag{3.41}$$

With,

$$\dot{\lambda}_3 = \dot{\overline{\left(\mu\lambda\right)}}^{-1}\left(\dot{\mu}\lambda + \mu\dot{\lambda}\right) \tag{3.42}$$

The only remaining issue is the matter of the material derivative which we have denoted by $\dot{(\,)} \equiv \frac{\partial}{\partial t}(\,)$. Since taking this derivative introduces another time parameter in the denominator (i.e. $\dot{(\,)} = \left[\frac{1}{time}\right]$), we must introduce a non-dimensional time parameter, $\bar{t}$, defined by $t = \tau\bar{t}$, where τ carries the dimensions of time. Therefore, $\dot{(\,)} = \frac{\partial}{\partial t}(\,) = \frac{\partial}{\partial\bar{t}}\frac{\partial\bar{t}}{\partial t}(\,) = \frac{1}{\tau}\frac{\partial}{\partial\bar{t}}(\,)$. Henceforth, all time derivatives will be in terms of the dimensionless $\bar{t}$.

To show that we have consistently constructed all non-dimensional quantities, note the following unit cancellation (where $[\,] = \ units\ of$) in the second term on the right-hand-side of the stresses $\hat{P}_\alpha$ ($\alpha = 1,2$): $\frac{[\bar{\nu}]}{[\lambda_\alpha]}\left([\lambda_\alpha^3][\dot{\lambda}_\alpha] - [\lambda_3][\dot{\lambda}_3]\right) = \frac{[\nu]}{[G]}\left([\frac{1}{\tau}]\right) = \frac{(mass/time)}{(force/length)}\left(\frac{1}{time}\right) = \left(\,-\,\right)$. Therefore, our stresses are truly dimensionless.

3.2.3 Kinematic Viscosity Coefficient for Arterial Tissue, ν

To implement our viscoelastic model, we need appropriate *physical* values for the kinematic viscosity coefficient, ν. We will refer to the study by Busse et al. [35] on the effects of elastic and viscous properties of arterial wall tissue on stress states and use an average of the experimentally derived values of viscosity reported therein (Table 1 of [35]). The material parameters reported are for excised sections of rat abdominal aorta (which we assume to have comparable material characteristics to a human artery). We find the average to be $\nu = 81.9$ kPa·sec.

3.3 Potential Energy

So far we have characterized our surface, developed a measure of deformation and stress, and defined some fundamental quantities for a vessel modeled as a thin sheet. Our next step is to set up the equations of motion for our vessel in order to solve some very simple initial boundary value problems. We proceed in this vein by introducing definitions for the potential and kinetic energies that allow us to formulate our equilibrium conditions and equations of motion.

The total potential energy, E, of our material is simply the sum of the total strain energy, W (i.e. the measure of the work done by internal material forces) and the work done by the external pressure, P, on a unit of *current* material surface area. Assuming a unit of *current* material volume is given by, v, we may write the total strain energy as the following,

$$E = W - Pv \tag{3.43}$$

Where the negative sign indicates work being done *on* the material by the pressure and the total strain energy is defined over a unit area in the reference configuration, $\partial\Omega_o$, as,

$$W \equiv \int\limits_{\partial\Omega_o} \omega(\lambda, \mu) dA \tag{3.44}$$

The volume in the current configuration, Ω, can be found by the following formula (recalling that $\mathbf{r}$ is the location of a material point in the current configuration defined by (3.2)),

$$v = \frac{1}{3} \int\limits_{\Omega} div(\mathbf{r}) dv \tag{3.45}$$

We will assume the domain, Ω is closed, bounded and smooth; hence, we can use Gauss's divergence theorem to bring the integral to a unit current area. Since our Jacobian can be expressed as a volume ratio, $J = \frac{dv}{dV}$, we can pull-back the integral to a unit area of the reference configuration.

$$\begin{aligned} v &= \frac{1}{3} \int\limits_{\partial\Omega} \mathbf{n} \cdot \mathbf{r} da \\ &= \frac{1}{3} \int\limits_{\partial\Omega_o} J\mathbf{n} \cdot \mathbf{r} dA \end{aligned} \tag{3.46}$$

We can now represent our total strain energy as the following,

$$\begin{aligned} E &= \int_{\partial\Omega_o} \omega(\lambda,\mu)dA - \frac{P}{3}\int_{\partial\Omega_o} J\mathbf{n}\cdot\mathbf{r}dA \\ &= \int_{\partial\Omega_o} \Big(\omega(\lambda,\mu) - \frac{P}{3}J\mathbf{n}\cdot\mathbf{r}\Big)dA \end{aligned} \tag{3.47}$$

Noting that the reference configuration of our domain is a right circular cylinder with an element of differential surface area of $dA = 2\pi R dz$, we can represent the integral over the reference axial length (L_o) (and move the $2\pi R$ outside the integral as R is of course constant),

$$E = 2\pi R \int_{L_o} \Big(\omega(\lambda,\mu) - \frac{P}{3}J\mathbf{n}\cdot\mathbf{r}\Big)dz \tag{3.48}$$

We first focus on the right-hand portion of the integrand. Recalling the formulation (3.18) and the definition of the current radius in (3.2), we can form the inner product, $J\mathbf{n}\cdot\mathbf{r}$, as the following,

$$\begin{aligned} J\mathbf{n}\cdot\mathbf{r} &= \mu(\zeta'(z)\mathbf{e_r}(\theta) - r'(z)\mathbf{k})\cdot(r\mathbf{e_r}(\theta) + \zeta\mathbf{k}) \\ &= \mu(r\zeta'(z) - r'(z)\zeta) \end{aligned} \tag{3.49}$$

Therefore,

$$E = 2\pi R \int_{L_o} \Big(\omega(\lambda,\mu) - \frac{P}{3}\mu(r\zeta'(z) - r'(z)\zeta)\Big)dz \tag{3.50}$$

In order to manipulate the equations more easily, we will generalize the integrand as some function, say $F(r, r'(z), \zeta, \zeta'(z))$ (Note that we have noticed that the integrand is a function of the variables $(r, r'(z), \zeta, \zeta'(z))$ because the arguments of $\omega(\lambda,\mu)$ are $\mu = \frac{r}{R}$ and $\lambda = ((r'(z))^2 + (\zeta'(z))^2)^{1/2}$.),

$$F(r, r'(z), \zeta, \zeta'(z)) = \omega(\lambda,\mu) - \frac{P}{3}\mu(r\zeta'(z) - r'(z)\zeta) \tag{3.51}$$

Therefore,

$$E = 2\pi R \int_{L_o} F(r, r'(z), \zeta, \zeta'(z))dz \tag{3.52}$$

Furthermore, we define a dimensionless integrand (suppressing the arguments),

$\bar{F}$ as $F = G\bar{F}$. With definition (3.51), our dimensionless quantities (3.19) and (3.20) and using the relationships between the derivatives shown in (3.21) and (3.22), we have,

$$\begin{aligned}
\bar{F} &= \frac{\omega}{G} - \frac{P}{3G}\mu(r\zeta'(z) - r'(z)\zeta) \\
&= \bar{\omega} - \frac{P}{3G}\mu(\mu R\bar{\zeta}'(x) - \mu'(x)R\bar{\zeta}) \\
&= \bar{\omega} - \frac{PR}{3G}\mu(\mu\bar{\zeta}'(x) - \mu'(x)\bar{\zeta}) \\
&= \bar{\omega} - \bar{P}(\mu^2\bar{\zeta}'(x) - \mu\mu'(x)\bar{\zeta}) \qquad (3.53)
\end{aligned}$$

Where, in (3.53_4), we have defined the dimensionless pressure as $\bar{P} = \frac{PR}{3G}$.

Therefore, if we change our domain of integration using $dz = Rdx$, our total potential energy equation (3.52) becomes the following,

$$\begin{aligned}
\frac{E}{2\pi R} &= GR\int\limits_{L_o} \bar{F}(\mu, \mu'(x), \bar{\zeta}, \bar{\zeta}'(x))dx \\
\frac{E}{2\pi GR^2} &= \int\limits_{L_o} \bar{F}(\mu, \mu'(x), \bar{\zeta}, \bar{\zeta}'(x))dx \qquad (3.54)
\end{aligned}$$

We will define a "normalized" total potential energy, say $\bar{E}$,

$$\bar{E} = \frac{E}{2\pi GR^2} \qquad (3.55)$$

Therefore, we have the final form of our dimensionless total potential energy as,

$$\bar{E} = \int\limits_{L_o} \bar{F}(\mu, \mu'(x), \bar{\zeta}, \bar{\zeta}'(x))dx \qquad (3.56)$$

Equation (3.56) is the form we will use in all subsequent analysis.

3.4 Kinetic Energy

The total kinetic energy of the system can be represented by the following equation,

$$K = \int_{L_o} \frac{\rho}{2}\Big((\dot{r})^2 + (\dot{\zeta})^2\Big)dz \tag{3.57}$$

Where, ρ is the density (mass per unit reference length, L_o) and we recall that r and ζ are the deformed radial and axial coordinates, respectively.
Using the same dimensionless quantities previously defined, as well as the explicit form of the time derivative, we can show kinetic energy as the following,

$$K = \int_{L_o} \frac{\rho R^3}{2}\left(\left(\frac{d\mu}{dt}\right)^2 + \left(\frac{d\bar{\zeta}}{dt}\right)^2\right)dx \tag{3.58}$$

Recall we have introduced a dimensionless time, $\bar{t}$, defined by, $t \equiv \tau\bar{t}$, where τ has units of time. Therefore, our equation becomes,

$$K = \int_{L_o} \frac{\rho R^3}{2\tau^2}\left(\left(\frac{d\mu}{d\bar{t}}\right)^2 + \left(\frac{d\bar{\zeta}}{d\bar{t}}\right)^2\right)dx \tag{3.59}$$

Finally, we define our dimensionless total kinetic energy, say $\bar{K}$, as $K \equiv \left(\frac{\rho R^3}{\tau^2}\right)\bar{K}$ and we therefore have the following,

$$\bar{K} = \frac{1}{2}\int_{L_o} \left(\left(\frac{d\mu}{d\bar{t}}\right)^2 + \left(\frac{d\bar{\zeta}}{d\bar{t}}\right)^2\right)dx \tag{3.60}$$

Note that the quantity $\left(\frac{\rho R^3}{\tau^2}\right)$ has units of energy (e.g. Joules). The [dimensionless] *total* energy in the system is simply the sum, $E_{total} \equiv \bar{K} + \bar{E}$.

3.5 The Principle of Minimum Potential Energy

In this section we will derive the equilibrium (so called "Euler-Lagrange") equations for our system by applying the Principle of Minimum Potential Energy (PMPE). In the absence of kinetic energy, the state of *minimum* total potential energy is equivalent to a state of static equilibrium of the system. Therefore, if we minimize our total potential energy $\bar{E}$ given by (3.56) (here, a functional), we can identify the equilibrium equations of this system. To do this we will employ the theory of calculus of variations.

Since we have two dimensionless coordinates, $(\mu, \bar{\zeta})$ that *uniquely* define a material point in the *deformed* configuration (in which our functional 3.56 depends upon), we will get two Euler-Lagrange (or equilibrium) conditions - one for μ and one for $\bar{\zeta}$.

The development of the Euler-Lagrange equations depends on the fundamental theorem of calculus of variations in which we assume (we note that this is a strong assumption and weaker assumption makes the proof more complicated but we attain the same result) that the integrand of our functional, i.e. $\bar{F}(\mu, \mu'(x), \bar{\zeta}, \bar{\zeta}'(x))$, has continuous first partial derivatives in x over some arbitrary interval, $x \in [a, b]$. We will also assume that the boundary conditions are defined on that interval; for example,

$$\begin{aligned} \mu(a) &= c \\ \mu(b) &= d \\ \zeta(\bar{a}) &= e \\ \zeta(\bar{b}) &= f \end{aligned} \tag{3.61}$$

where, c, d, e, f are some known, arbitrary constants.

Over our interval, the functional we seek to minimize is thus,

$$\bar{E} = \int_a^b \bar{F}(\mu, \mu'(x), \bar{\zeta}, \bar{\zeta}'(x))dx \tag{3.62}$$

In the following, we will develop the Euler-Lagrange equation for the μ coordinate because the the steps are identical for the $\bar{\zeta}$ coordinate.

If μ optimizes (i.e. minimizes or maximizes) the "cost" functional, $\bar{E}$, subject to the boundary conditions (3.61), then a slight perturbation of μ that preserves the boundary values must either increase (if μ is a minimizer) or decrease $\bar{E}$ (if μ is a maximizer).

Let some function, say $g(x) = \mu(x) + \epsilon\eta(x)$, represent a prescribed perturbation of $\mu(x)$, where another function $\eta(x)$ is a differentiable function of x satisfying $\eta(a) = \eta(b) = 0$ (i.e. it adds nothing to the boundaries) and ϵ is the scalar value of the perturbation. Then define the total potential energy in terms of our perturbation as,

$$\bar{E}(\epsilon) = \int_a^b \bar{F}(x, g(x), g'(x))dx \tag{3.63}$$

Now calculate the total derivative of the potential energy (i.e. with respect to ϵ) while suppressing the dependency on x and keeping in mind that $(\,)' \equiv \frac{d}{dx}(\,)$,

$$\begin{aligned}\frac{\partial \bar{E}}{\partial \epsilon} &= \frac{\partial}{\partial \epsilon}\Big(\int_a^b \bar{F}(x, g, g')dx\Big)\\ &= \int_a^b \frac{\partial}{\partial \epsilon}\Big(\bar{F}(x, g, g')\Big)dx\\ &= \int_a^b \Big(\frac{\partial \bar{F}}{\partial x}\frac{\partial x}{\partial \epsilon} + \frac{\partial \bar{F}}{\partial g}\frac{\partial g}{\partial \epsilon} + \frac{\partial \bar{F}}{\partial g'}\frac{\partial g'}{\partial \epsilon}\Big)dx \end{aligned}\tag{3.64}$$

Where we note that $g' = \mu' + \epsilon\eta'$ (and therefore $\frac{\partial g'}{\partial \epsilon} = \eta'$) and $\frac{\partial x}{\partial \epsilon} = 0$ so,

$$\frac{\partial \bar{E}}{\partial \epsilon} = \int_a^b \Big(\frac{\partial \bar{F}}{\partial g}\eta + \frac{\partial \bar{F}}{\partial g'}\eta'\Big)dx \tag{3.65}$$

We notice that when our perturbation is zero (i.e. $\epsilon = 0$), that $g(x) = \mu(x)$. Since $\mu(x)$ represents an extrema for our system (i.e. a maximum or minimum value), we can see that the derivatives in the integrand (at $\epsilon = 0$) must be the following,

$$\begin{aligned}\Big(\frac{\partial \bar{F}}{\partial g}\Big)_{\epsilon=0} &= \frac{\partial \bar{F}}{\partial \mu} = 0\\ \Big(\frac{\partial \bar{F}}{\partial g'}\Big)_{\epsilon=0} &= \frac{\partial \bar{F}}{\partial \mu'} = 0\end{aligned}\tag{3.66}$$

Hence,

$$\Big(\frac{\partial \bar{E}}{\partial \epsilon}\Big)_{\epsilon=0} = \int_a^b \Big(\frac{\partial \bar{F}}{\partial \mu}\eta + \frac{\partial \bar{F}}{\partial \mu'}\eta'\Big)dx = 0 \tag{3.67}$$

We can of course split the integral into two parts and carry out the integration separately. Then, we can use integration by parts on the second integral to obtain the following,

$$\int_a^b \frac{\partial\bar{F}}{\partial\mu}\eta dx + \left[\frac{\partial\bar{F}}{\partial\mu'}\eta\right]_a^b - \int_a^b \left(\frac{\partial\bar{F}}{\partial\mu'}\right)'\eta dx = 0$$

$$\int_a^b \left(\frac{\partial\bar{F}}{\partial\mu}\eta - \left(\frac{\partial\bar{F}}{\partial\mu'}\right)'\eta\right)dx + \left[\frac{\partial\bar{F}}{\partial\mu'}\eta\right]_a^b = 0$$

$$\int_a^b \left(\frac{\partial\bar{F}}{\partial\mu} - \left(\frac{\partial\bar{F}}{\partial\mu'}\right)'\right)\eta(x)dx = 0 \tag{3.68}$$

The last equation is due to the fact that $\left[\frac{\partial\bar{F}}{\partial\mu'}\eta(x)\right]_a^b = 0$ from $\eta(a) = \eta(b) = 0$, as defined earlier (note we are showing the explicit x-dependence to show that $\eta(x)$ must remain inside the integral). If we define another function, say $G(x) = \frac{\partial\bar{F}}{\partial\mu} - \left(\frac{\partial\bar{F}}{\partial\mu'}\right)'$, then,

$$\int_a^b G(x)\eta(x)dx = 0 \tag{3.69}$$

Assuming that $G(x)$ is continually differentiable on the interval $[a, b]$ and again using $\eta(a) = \eta(b) = 0$, by the Fundamental Lemma of the Calculus of Variations, $G(x) = 0$.

Therefore, our equilibrium (Euler-Lagrange) equation for $\mu(x)$ is the following,

$$\frac{\partial\bar{F}}{\partial\mu} - \left(\frac{\partial\bar{F}}{\partial\mu'}\right)' = 0 \tag{3.70}$$

Following the same development for the $\bar{\zeta}(x)$ coordinate we have the following,

$$\frac{\partial\bar{F}}{\partial\bar{\zeta}} - \left(\frac{\partial\bar{F}}{\partial\bar{\zeta}'}\right)' = 0 \tag{3.71}$$

3.6 From Equilibrium to Equations of Motion

Since we will seek to include rate-effects in our model (developed in later sections), it is useful to employ the equations of motion instead of merely the equations of equilibrium shown in (3.70) and (3.71). This will enable us to use the method of *dynamic relaxation* that updates our numerical solution only when the the dynamic effects have dampened out, giving us a "new" and stable equilibrium state. To this end, we will simply add an inertial term (as our damping has been accounted for already in the formulation of the in-plane nominal stress measures, (3.40) and (3.41)) to each of the equations (3.70) and (3.71). Hence, our equations of motion are,

$$\begin{aligned}\frac{\partial\bar{F}}{\partial\mu}-\left(\frac{\partial\bar{F}}{\partial\mu'}\right)' &= \bar{\rho}\ddot{\mu}\\ \frac{\partial\bar{F}}{\partial\bar{\zeta}}-\left(\frac{\partial\bar{F}}{\partial\bar{\zeta}'}\right)' &= \bar{\rho}\ddot{\bar{\zeta}} \qquad (3.72)\end{aligned}$$

Where, $\bar{\rho}$ is the dimensionless density and $\ddot{(\,)} \equiv \frac{\partial^2}{\partial t^2}(\,)$.

3.7 Development of Euler-Lagrange Equation Components

In this section we will explicitly develop each part of the two Euler-Lagrange equations. This allows us to highlight the principal stresses and gives a platform to incorporate the strain-rate dependence into our stress expressions (using (3.40) and (3.41)) later on.
We will start with the first term in (3.70). Using the definition of $\bar{F}$ as shown in (3.53) as well as our definition of the principle in-plane stresses in (3.40) and (3.41) we have,

$$\begin{aligned}\frac{\partial\bar{F}}{\partial\mu} &= \frac{\partial}{\partial\mu}\Big(\bar{\omega}-\bar{P}\Big(\mu^2\bar{\zeta}'(x)-\mu\mu'(x)\bar{\zeta}\Big)\Big)\\ &= \frac{\partial\bar{\omega}}{\partial\mu}-\bar{P}\Big(2\mu\bar{\zeta}'(x)-\mu'(x)\bar{\zeta}\Big)\\ &= \hat{P}_1-\frac{\bar{\nu}}{\mu}\Big(\mu^3\dot{\mu}-\lambda_3\dot{\lambda}_3\Big)-\bar{P}\Big(2\mu\bar{\zeta}'(x)-\mu'(x)\bar{\zeta}\Big) \qquad (3.73)\end{aligned}$$

Similarly, we can develop the second term in the first EL equation as,

$$\begin{aligned}
\frac{\partial \bar{F}}{\partial \mu'} &= \frac{\partial}{\partial \mu'}\Big(\bar{\omega} - \bar{P}\Big(\mu^2\bar{\zeta}'(x) - \mu\mu'(x)\bar{\zeta}\Big)\Big) \\
&= \frac{\partial \bar{\omega}}{\partial \mu'} + \bar{P}\mu\bar{\zeta} \\
&= \Big(\frac{\partial \bar{\omega}}{\partial \lambda}\Big)\Big(\frac{\partial \lambda}{\partial \mu'}\Big) + \bar{P}\mu\bar{\zeta} \\
&= \Big(\hat{P}_2 - \frac{\bar{\nu}}{\lambda}\Big(\lambda^3\dot{\lambda} - \lambda_3\dot{\lambda}_3\Big)\Big)\Big(\frac{\mu'}{\lambda}\Big) + \bar{P}\mu\bar{\zeta} \qquad (3.74)
\end{aligned}$$

Notice how we have used the chain rule in the development to allow the derivative of the strain energy density, $\bar{\omega}$, with respect to one of the principal stretches, λ.

Similarly, we can show that the first term in (3.71) is the following,

$$\begin{aligned}
\frac{\partial \bar{F}}{\partial \bar{\zeta}} &= \frac{\partial}{\partial \bar{\zeta}}\Big(\bar{\omega} - \bar{P}\Big(\mu^2\bar{\zeta}'(x) - \mu\mu'(x)\bar{\zeta}\Big)\Big) \\
&= \bar{P}\mu\mu'(x) \qquad (3.75)
\end{aligned}$$

Note that $\frac{\partial \bar{\omega}}{\partial \bar{\zeta}} = 0$.

The second term in (3.71) is,

$$\begin{aligned}
\frac{\partial \bar{F}}{\partial \bar{\zeta}'} &= \frac{\partial}{\partial \bar{\zeta}'}\Big(\bar{\omega} - \bar{P}\Big(\mu^2\bar{\zeta}'(x) - \mu\mu'(x)\bar{\zeta}\Big)\Big) \\
&= \frac{\partial \bar{\omega}}{\partial \bar{\zeta}'} - \bar{P}\mu^2 \\
&= \Big(\frac{\partial \bar{\omega}}{\partial \lambda}\Big)\Big(\frac{\partial \lambda}{\partial \bar{\zeta}'}\Big) - \bar{P}\mu^2 \\
&= \Big(\hat{P}_2 - \frac{\bar{\nu}}{\lambda}\Big(\lambda^3\dot{\lambda} - \lambda_3\dot{\lambda}_3\Big)\Big)\Big(\frac{\bar{\zeta}'}{\lambda}\Big) - \bar{P}\mu^2 \qquad (3.76)
\end{aligned}$$

3.8 Hyperelasticity and Polyconvexity

Recall that the definition of a Green-elastic (Hyperelastic) material is one in which we assume the existence of a Helmholtz free energy function that is itself a function of a strain or deformation tensor. If the material is isotropic (which we are assuming here), this *strain energy function* can be represented in terms of the principal invariants or stretches, generically, as $\omega = \tilde{\omega}(i_1, i_2, i_3) = \bar{\omega}(\lambda_1, \lambda_2, \lambda_3)$. if we define this strain energy function per unit reference volume, we have a strain energy density, ω. The principal invariants are defined in terms of the right Cauchy stretch tensor **U** and the (general) principal stretches as,

$$\begin{aligned} i_1 &= tr(\mathbf{U}) = \boldsymbol{\lambda_1} + \lambda_2 + \boldsymbol{\lambda_3} \\ i_2 &= tr(\mathbf{U}^*) = \boldsymbol{\lambda_1}\lambda_2 + \lambda_2\boldsymbol{\lambda_3} + \boldsymbol{\lambda_1}\boldsymbol{\lambda_3} \\ i_3 &= det(\mathbf{U}) = \boldsymbol{\lambda_1}\lambda_2\boldsymbol{\lambda_3} \end{aligned} \tag{3.77}$$

We will assume incompressibility for this model, therefore we can relate the principal stretches in the following way,

$$\begin{aligned} det(\mathbf{U}) &= \boldsymbol{\lambda_1}\lambda_2\boldsymbol{\lambda_3} = \mathbf{1}, \\ \lambda_3 &= (\lambda_1\lambda_2)^{-1} \end{aligned} \tag{3.78}$$

Furthermore, due to our incompressibility constraint, we can represent our isotropic strain energy function as, $\omega = \tilde{\omega}(i_1, i_2)$.
We say that our material is *polyconvex* by ensuring the strain energy density is a jointly convex and non-decreasing function of both arguments; namely,

$$\frac{\partial \omega}{\partial i_1} > 0, \frac{\partial \omega}{\partial i_2} > 0 \tag{3.79}$$

Additionally, if we are to perturb either argument (i_1, i_2) we require (for our polyconvex strain energy density) the following condition,

$$\omega(i_1 + \Delta i_1, i_2 + \Delta i_2) - \omega(i_1, i_2) \geq \frac{\partial \omega}{\partial i_1}\Delta i_1 + \frac{\partial \omega}{\partial i_2}\Delta i_2 \tag{3.80}$$

Further implying the following two conditions (see Steigmann [36]),

$$\begin{gathered} \frac{\partial^2 \omega}{\partial i_1^2} \geq 0, \frac{\partial^2 \omega}{\partial i_2^2} \geq 0 \\ \left(\frac{\partial^2 \omega}{\partial i_1^2}\right)\left(\frac{\partial^2 \omega}{\partial i_2^2}\right) - \frac{\partial^2 \omega}{\partial i_1 \partial i_2} \geq 0 \end{gathered} \tag{3.81}$$

3.9 Bio-strain Energy Functions

Much like a Neo-Hookean model for rubber-like (i.e. hyperelastic), isotropic, incompressible materials, we will assume a strain energy density that depends only on the first principal invariant of the Cauchy stretch tensor, i_1. There are various polynomial forms of rubber-like, isotropic strain energy density functions for isotropic materials (e.g. Ogden, Mooney-Rivlin, Neo-Hookean, Varga, etc.)

but here we assume an *exponential* form of our strain energy density that may help capture the nonlinear stiffening of our material under large strains more effectively. We propose the following potential for the membrane model of our artery,

$$\omega(i_1) = \frac{G}{2\gamma}\Big(e^{f(i_1)} - 1\Big) \tag{3.82}$$

Where G is the shear modulus (units $[G] = energy/area$ or $force/length$) and $\gamma \in [0, 1]$ is a dimensionless constant representing the "health" of the material ($\gamma = 1.0$ being healthy tissue). Furthermore, assume $f(i_1) \equiv \gamma(i - 3)$. With our incompressibility constraint, the first principal invariant (dropping the subscript to simplify the notation) becomes, $i = \lambda_1 + \lambda_2 + (\lambda_1\lambda_2)^{-1}$. So our strain energy density becomes the following,

$$\omega(\lambda_1, \lambda_2) = \frac{G}{2\gamma}\Big(e^{\gamma(i-3)} - 1\Big) \tag{3.83}$$

Up to this point, we have generalized the principal stretches as λ_1, λ_2. Considering the change of stretch variables to those of our current problem (i.e. $\lambda_1 \equiv \lambda$ and $\lambda_2 \equiv \mu$) we have,

$$\omega(\lambda, \mu) = \frac{G}{2\gamma}\Big(e^{\gamma(i-3)} - 1\Big) \tag{3.84}$$

Where now $i = \lambda + \mu + (\lambda\mu)^{-1}$.

Since we have formed the strain energy density in terms of the in-plane principal stretches (λ, μ), our model can be applied to a 2D surface (i.e. a Cosserat surface) where the out-of-plane thickness is negligible compared to the shortest in-plane length. As such, the units of our strain energy density are $[\omega] = energy/area$ or $force/length$.

We can define a dimensionless strain energy density, $\bar{\omega}$ as, $\omega = G\bar{\omega}$ and therefore,

$$\bar{\omega}(\lambda, \mu) = \frac{1}{2\gamma}\Big(e^{\gamma(i-3)} - 1\Big) \tag{3.85}$$

3.9.1 Material stability

By applying the rules of finite elasticity (see, for example, Ogden [37]) we can further analyze the material stability of (3.85) based on variations of principal stretches, μ, λ, internal pressure, P and the material parameter, γ.
We start by recalling the total potential energy in the membrane (i.e. equations 3.43 and 3.44). Substituting we have the following,

$$E(\lambda,\mu) = \int_{\partial\Omega_o} \omega(\lambda,\mu) dA - Pv. \tag{3.86}$$

We note that $\int_{\partial\Omega_o} dA = 2\pi RL$, where R, L is the undeformed radius and length of the tube, respectively. The current volume is defined as $v = \pi r^2 l$, where r, l are the deformed radius and length. Therefore,

$$E(\lambda,\mu) = \omega(\lambda,\mu) 2\pi RL - P\pi r^2 l. \tag{3.87}$$

Equilibrium corresponds to the following two conditions conditions,

$$\begin{aligned} (1)\ \frac{\partial E(\lambda,\mu)}{\partial\mu} &= 0 \Rightarrow 2\Big(\frac{\partial\omega}{\partial\mu}\Big) = 2PR\mu\lambda \\ (2)\ \frac{\partial E(\lambda,\mu)}{\partial\lambda} &= 0 \Rightarrow 2\Big(\frac{\partial\omega}{\partial\lambda}\Big) = PR\mu^2 \end{aligned} \tag{3.88}$$

Solving for our pressure then yields,

$$\begin{aligned} (1)\ P &= \Big(\frac{\partial\omega}{\partial\mu}\Big)\frac{1}{R\mu\lambda} \\ (2)\ P &= \Big(\frac{\partial\omega}{\partial\lambda}\Big)\frac{2}{R\mu^2} \end{aligned} \tag{3.89}$$

If we choose to look at the relationship between pressure and radial stretch, μ, (i.e. 3.89 - (2)) we can get a fair idea how the cylinder deforms as we increase the internal pressure for a fixed value of axial stretch. This is physically less-useful as it would require the ends of the vessel to be be allowed to expand radially (e.g. on rollers) yet the axial stretch remain fixed. Along these lines, if we plot the pressure versus the radial stretch, μ, for a given axial stretch, $\lambda = 1.25$, and we vary the biological "health" parameter, γ, we see the behavior shown in figure (3.3).

For each value γ, the region of the plot with a negative slope corresponds to an unstable equilibrium and the cylinder will "snap-through" to a new radial stretch and stable equilibrium. As expected, the lower values of γ (corresponding to "poor" material strength) coincide with a "snap-through" at lower internal pressures. Conversely, the "healthier" material will not experience an unstable equilibrium point (i.e. inflection point). In the context of modeling an arterial section, we can say that at a certain internal pressure, this snap-through is when a bulge, or aneurysm, would suddenly appear. Further, the plot shows an intuitive response of a rubber-like material in that the cylinder is at first more difficult to inflate

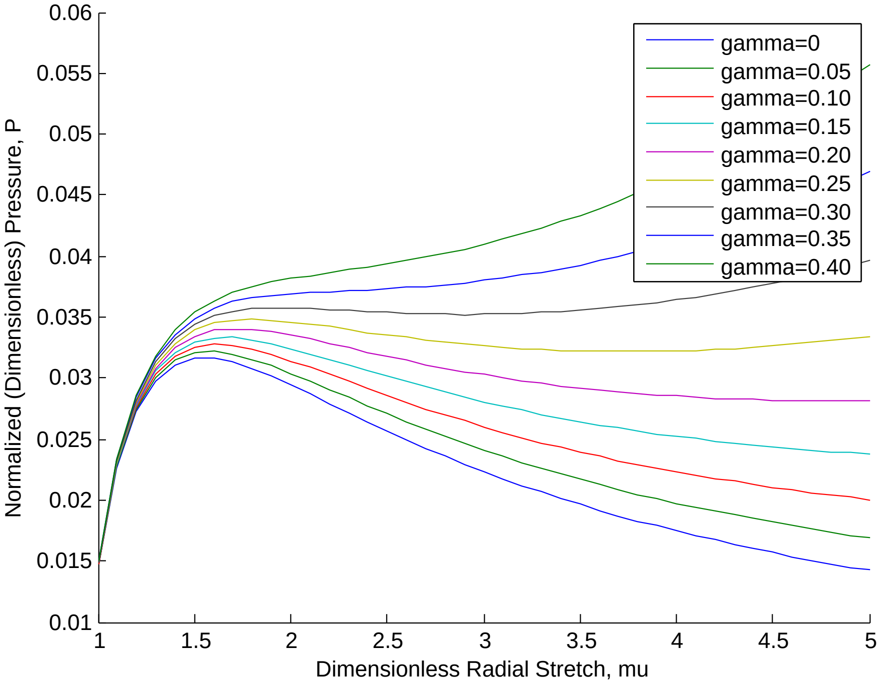

Figure 3.3: Modeling diseased tissue; pressure versus radial stretch for ”healthy” and ”unhealthy” tissue

(large initial positive slope) and as it grows, becomes increasingly less resistant to the pressure. Although this behavior is indicative of polymers and rubber-like materials undergoing large deformations, it is unfortunately not a characteristic of an arterial wall under supraphysiological deformations. For arteries, the collagen fibers in the adventitia layer provide increasing stiffness to deformations past a certain point (hence the need for a more histological model, as in the following chapter). Nevertheless, this simple membrane model can provide a useful scaffold to various strain energy functions reported in terms of principal material stretches.

We can also fix γ and plot the pressure versus radial stretch for a range of axial stretches. Figure (3.4) shows how at a value of $\gamma = 0.20$, for large axial stretch (e.g. $\lambda = 5.0$,$\lambda = 10.0$) the slope is immediately negative indicating an unstable equilibrium state where the cylinder will initially bulge to a larger radius given any increment in pressure.

To capture realistic boundary conditions where the ends are not allowed to radially expand but are held fixed, we must satisfy simultaneously both equations in (3.89).

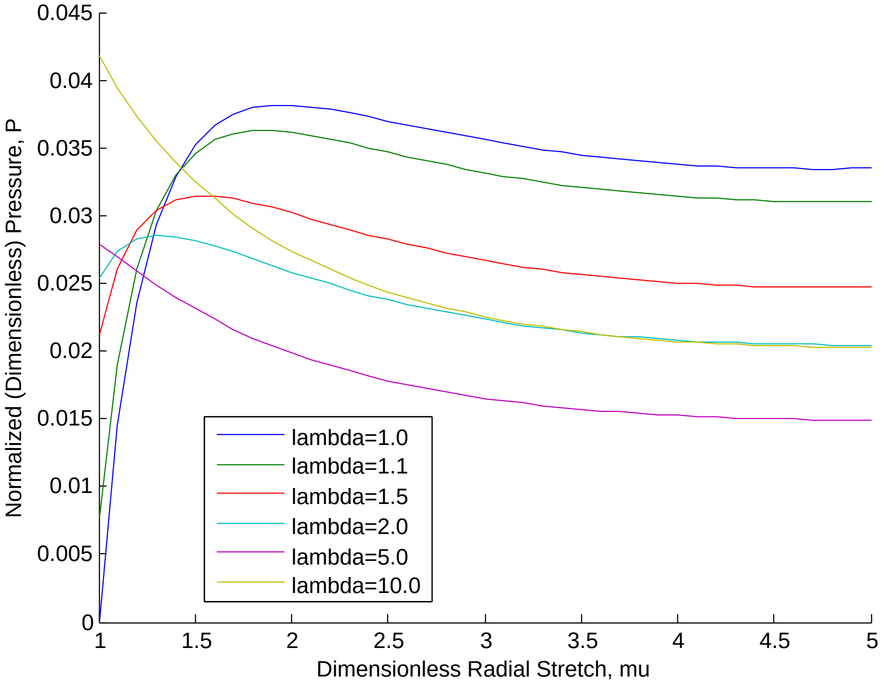

Figure 3.4: Modeling supraphysiological deformations; pressure versus radial stretch at very large axial stretch

3.9.2 Popular 2D bio-strain energy functions

We shall compare our potential (3.84) to three types of material models reported in Fu et al. [13]: Varga, Ogden and Gent, for which the strain energy functions are given, respectively, by,

$$\omega_V = 2G\Big(\lambda + \mu + \frac{1}{\lambda\mu}\Big), \tag{3.90}$$

$$\omega_O = \sum_{r=1}^{3} \frac{G_r}{\alpha_r}\Big(\lambda^{\alpha_r} + \mu^{\alpha_r} + \Big(\frac{1}{\lambda\mu}\Big)^{\alpha_r} - 3\Big), \tag{3.91}$$

$$\omega_G = -\frac{1}{2}GJ_m ln\Big(1 - \frac{J_1}{J_m}\Big), \quad J_1 = \lambda^2 + \mu^2 + \Big(\frac{1}{\lambda\mu}\Big)^2, \tag{3.92}$$

where G is again the shear modulus for infinitesimal deformations, J_m is a material constant between values of 0.422 and 3.93 (for human arteries, found experimentally by Horgan et al. [38]). For the Ogden model (see [37]), $\alpha_1 = 1.3$, $\alpha_2 = 5.0$, $\alpha_3 = -2.0$, $G_1 = 1.491$, $G_2 = 0.003$, $G_3 = -0.023$, are the material constants.

To summarize which two-dimensional models we will use as well as the elastic constants, see Table (3.1).

2D Potential	Material Constants	Reference
$\omega = \frac{G}{2\gamma}\left(e^{\gamma(i-3)} - 1\right)$	$\gamma = [0,1]$ $i = \lambda + \mu + (\lambda\mu)^{-1}$	Fung et al. [31]
$\omega_V = 2G\left(\lambda + \mu + \frac{1}{\lambda\mu}\right)$	-	Fu et al. [13]
$\omega_O = \sum_{r=1}^{3} \frac{G_r}{\alpha_r}\left(\lambda^{\alpha_r} + \mu^{\alpha_r} + \left(\frac{1}{\lambda\mu}\right)^{\alpha_r} - 3\right)$	$G_1 = 1.491, G_2 = 0.003, G_3 = -0.023$ $\alpha_1 = 1.3, \alpha_2 = 5.0, \alpha_3 = -2.0$	Ogden et al. [37]
$\omega_G = -\frac{1}{2}GJ_m ln\left(1 - \frac{J_1}{J_m}\right)$	$J_m = [0.422, 3.93]$ $J_1 = \lambda^2 + \mu^2 + \left(\frac{1}{\lambda\mu}\right)^2$	Horgan et al. [38]

Table 3.1: Summary of common 2D potentials and constants for modeling arterial wall tissue

3.10 Numerical Methods - A Finite-Difference Model of the Discretized Membrane Equations

We propose a time-dependent, finite-difference model of the discretized membrane formulation with various hyperelastic strain energy functions for assessing the overall deformation of a right-circular cylinder.

From the equations of motion defined in (3.108), we can isolate the principal stretches, μ and λ, and develop an expression for each. To solve these expressions numerically, we can use a spatial discretization where we consider a 1D array of nodes that represent a cross-section of the membrane wall along the length of the tube (Fig. 3.5). We may then specify the boundary conditions and and update the stretches at each time-step.

3.10.1 Time Discretization

It is evident that equations (3.108) define the motion of a discrete material particle (or here, a node in our membrane mesh) in time. As a template for developing the expression for the time-discretization of our nodal network, consider first the simplest case: the dynamics of a simple particle moving in one dimension. The equation of motion is the following,

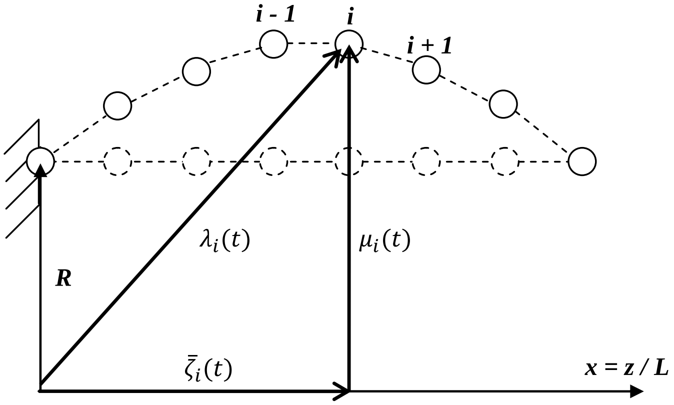

Figure 3.5: Numerical methods: a 1D nodal array

$$m\frac{d}{dt}(\dot{u}) = F \tag{3.93}$$

where, F is the total force on the particle, m is its mass and $\dot{u}$ is it's velocity. Expand $\dot{u}$ in a Taylor-series about time $(t + a\Delta t)$. This gives the following,

$$\dot{u}(t+\Delta t) = \dot{u}(t + a\Delta t) + \frac{d}{dt}(\dot{u})|_{t+a\Delta t}(1-a)\Delta t + \frac{1}{2}\frac{d^2}{dt^2}(\dot{u})|_{t+a\Delta t}(1-a)^2\Delta t^2 + \vartheta(\Delta t)^3 \tag{3.94}$$

and,

$$\dot{u}(t) = \dot{u}(t + a\Delta t) - \frac{d}{dt}(\dot{u})|_{t+a\Delta t}a\Delta t + \frac{1}{2}\frac{d^2}{dt^2}(\dot{u})|_{t+a\Delta t}a^2\Delta t^2 + \vartheta(\Delta t)^3 \tag{3.95}$$

Subtract the two expressions and let $a = \frac{1}{2}$ to yield the following,

$$\frac{d}{dt}(\dot{u})|_{t+a\Delta t} = \frac{\dot{u}(t+\Delta t) - \dot{u}(t)}{\Delta t} + \vartheta(\Delta t)^2 \tag{3.96}$$

Substitute (3.96) into the equation of motion (3.93) giving,

$$m\left(\frac{\dot{u}(t+\Delta t) - \dot{u}(t)}{\Delta t} + \vartheta(\Delta t)^2\right) = F \tag{3.97}$$

or,

$$\dot{u}(t + \Delta t) = \dot{u}(t) + \frac{\Delta t}{m} F(t + a\Delta t) + \vartheta(\Delta t)^2 \tag{3.98}$$

Define a weighted sum of $\dot{u}(t)$ and $\dot{u}(t + \Delta t)$ as,

$$\dot{u}(t + a\Delta t) = a\dot{u}(t + \Delta t) + (1 - a)\dot{u}(t) + \vartheta(\Delta t)^2 \tag{3.99}$$

where, $a \in [0, 1]$.
Similarly expand the position of the particle, $u(t)$, about time $(t + a\Delta t)$,

$$u(t + \Delta t) = u(t + a\Delta t) + \frac{d}{dt}(u)|_{t+a\Delta t}(1 - a)\Delta t + \frac{1}{2}\frac{d^2}{dt^2}(u)|_{t+a\Delta t}(1 - a)^2\Delta t^2 + \vartheta(\Delta t)^3 \tag{3.100}$$

and,

$$u(t) = u(t + a\Delta t) - \frac{d}{dt}(u)|_{t+a\Delta t} a\Delta t + \frac{1}{2}\frac{d^2}{dt^2}(u)|_{t+a\Delta t} a^2\Delta t^2 + \vartheta(\Delta t)^3 \tag{3.101}$$

Again, subtract the two expressions and let $a = \frac{1}{2}$ to yield the following,

$$\frac{u(t + \Delta t) - u(t)}{\Delta t} = \frac{d}{dt}(\dot{u})|_{t+a\Delta t} + \vartheta(\Delta t)^2 \tag{3.102}$$

Insert the weighted sum (3.99) into (3.102) giving,

$$u(t + \Delta t) = u(t) + \Big(a\dot{u}(t + \Delta t) + (1 - a)\dot{u}(t)\Big)\Delta t + \vartheta(\Delta t)^2 \tag{3.103}$$

Using the definition for $\dot{u}(t + \Delta t)$ given in equation (3.99),

$$u(t + \Delta t) = u(t) + a\Big(\dot{u}(t) + \frac{\Delta t}{m} F(t + a\Delta t) + \vartheta(\Delta t)^2\Big)\Delta t + (1 - a)\dot{u}(t)\Delta t + \vartheta(\Delta t)^2 \tag{3.104}$$

or,

$$u(t + \Delta t) = u(t) + \dot{u}(t)\Delta t + \frac{a(\Delta t)^2}{m} F(t + a\Delta t) + o(\Delta t)^2 \tag{3.105}$$

where, $o(\Delta t)^2 \equiv \vartheta(\Delta t)^3$.
Assume a weighted sum approximation for $F(t + a\Delta t)$ (for more rigorous discussion see Zohdi []),

$$F(t + a\Delta t) \approx aF\Big(u(t + \Delta t)\Big) + (1 - a)F\Big(u(t)\Big) \tag{3.106}$$

Therefore, we reach our final result for the updated position of the particle at time $(t + \Delta t)$ as a function of the weighted averages of the total force at time, t and $(t + \Delta t)$,

$$u(t+\Delta t) = u(t) + \dot{u}(t)\Delta t + \frac{a(\Delta t)^2}{m}\Big(aF\big(u(t+\Delta t)\big) + (1-a)F\big(u(t)\big)\Big) + o(\Delta t)^2 \tag{3.107}$$

Our time-stepping scheme is then chosen as the following,

- $a = 1$: Backward Euler (Implicit), "A-stable" (see []) and the local truncation error (committed per time step) is $\vartheta(\Delta t)$,
- $a = 0$: Forward Euler (Explicit), conditionally stable and locally $\vartheta(\Delta t)^2$, or,
- $a = \frac{1}{2}$: Midpoint-Rule (Implicit), "A(α)-stable" (see []), locally $\vartheta(\Delta t)^3$.

To extend this simple example to (3.108), explicitly, we can see,

$$\begin{aligned} \underbrace{\frac{\partial \bar{F}}{\partial \mu} - \left(\frac{\partial \bar{F}}{\partial \mu'}\right)'}_{F_1} &= \underbrace{\bar{\rho}\ddot{\mu}}_{m\frac{d}{dt}(\dot{\lambda_1})} \\ \underbrace{\frac{\partial \bar{F}}{\partial \bar{\zeta}} - \left(\frac{\partial \bar{F}}{\partial \bar{\zeta}'}\right)'}_{F_2} &= \underbrace{\bar{\rho}\ddot{\bar{\zeta}}}_{m\frac{d}{dt}(\dot{\lambda_2})} \end{aligned} \tag{3.108}$$

where it is clear that we can make the analogy that "F" $= F_{1,2}$ and "u" $= \lambda_{1,2}$ and of course $\lambda_1 = \mu$ and $\lambda_2 = \bar{\zeta}$.

Fig. (3.5) shows a schematic of the one-dimensional nodal network and the stretches we will be tracking (i.e. μ and $\bar{\zeta}$) as our numerical scheme progresses in time (note spatial derivatives, as indicated in our equations by $(\,)' = \frac{d}{dx}$, are found using a Taylor-series expansion around node, i).

Time-Stepping - The CFL Condition

A requirement for numerical stability (specifically for an explicit formulation although we will use this a fraction of this critical time-step in our implicit models as well) is that the time-step be sufficiently small to ensure the grid velocity, or the speed at which the equations are updated, does not exceed the sound speed of the material. This restriction on the time-step is called the Courant-Freidrichs-Levvy (CFL) Condition and has the following representation,

$$\Delta t_C < \frac{\Delta x C}{v} \tag{3.109}$$

Where, Δt_C is the critical time-step, Δx is the minimum grid spacing between the nodes (here in 1D), $C < 1.0$ is a constant called the Courant number and v is the sound speed in the material. For an isotropic material (which we have here), the sound-speed is defined through the material elastic constants C_{ij} (Young's modulus and bulk modulus are typical choices) and the density, ρ. We will use the following definition for material sound-speed, $v = \sqrt{E/\rho}$.

3.11 Results

Before we employ our IBVP on the 1D finite-difference model, we must validate that the model (i.e. the computer code) is working correctly. To do this, we have constructed a number of simple tests to convince ourselves that its behavior is consistent with both phenomenological and analytical predictions. The following is a series of such validations.

3.11.1 Numerical Model Validations

Total Energy

Because we have included rate-effects into our formulation, we expect that following an increment in either the pressure or the stretch of the tube, the total energy of the system (i.e. potential + kinetic) must decrease to a constant value (the rate at which it does this and the amount of overshoot is dictated by the degree of damping we have). Although this is a fairly trivial idea, it is quite useful in validating that the numerical computation is correct; namely, if we have an *increase* in the total energy after incremental deformation, the numerical implementation is flawed. This criteria was checked and the total energy in the system does decrease to a constant value after an increment in the pressure or axial stretch.

The Euler Condition

A useful check that we correctly numerically implemented our membrane formulation is by employing the so-called Euler Condition. This is a necessary condition and stems from equating the two Euler-Lagrange (equilibrium) equations (3.70,3.71) (as they are both zero).

$$\frac{\partial \bar{F}}{\partial \mu} + \frac{\partial \bar{F}}{\partial \bar{\zeta}} = \left(\frac{\partial \bar{F}}{\partial \mu'}\right)' + \left(\frac{\partial \bar{F}}{\partial \bar{\zeta}'}\right)' \tag{3.110}$$

where again $\left(\,\right)' = \frac{d}{dx}$ and x is the dimensionless axial coordinate. If we integrate along the axial direction we have,

$$\int_x \left(\frac{\partial \bar{F}}{\partial \mu} + \frac{\partial \bar{F}}{\partial \bar{\zeta}}\right) dx - \frac{\partial \bar{F}}{\partial \mu'} - \frac{\partial \bar{F}}{\partial \bar{\zeta}'} = Constant \tag{3.111}$$

which becomes,

$$\bar{F} - \mu'\left(\frac{\partial \bar{F}}{\partial \mu'}\right) - \bar{\zeta}'\left(\frac{\partial \bar{F}}{\partial \bar{\zeta}'}\right) = Constant. \tag{3.112}$$

In other words, the LHS of (3.112) is independent of the axial coordinate, x. Successive runs of the membrane model show that the LHS of (3.112) is indeed a constant (i.e. when plotted against x) +/- a tolerance that is within our numerical error (i.e. $< \vartheta(h)^2$, where h is the grid spacing).

Necking

We expect, intuitively, that the membrane will gradually narrow or neck midspan as one end is held fixed and the other is pulled axially (i.e. the ”soap bubble effect”). Fig. (3.6) show a series of 1D axial stretches that show this behavior and validate that our viscoelastic bio-tissue material model is globally deforming as we assume.

Cylinder to Pressurized Cylinder

A rather easy-to-check analytical result that we may use to validate whether our numerical model is working correctly is obtained by the following procedure.

1. Recall the (dimensionless) total potential energy, $\bar{E}$ as defined in (3.56) with the integrand explicitly shown is the following,

$$\bar{E}(\lambda, \mu) = \int_{x=0}^{x=L/R} \left(\bar{\omega} - \bar{P}(\mu^2\bar{\zeta}'(x) - \mu\mu'(x)\bar{\zeta})\right) dx \tag{3.113}$$

2. Now assume that the deformed equilibrium configuration of our tube is a cylinder with a constant (in axial length, x) *radial* stretch, μ^*. Therefore, $\mu'(x) = 0$ and hence $\lambda = ((\mu'(x))^2 + (\bar{\zeta})^2)^{1/2} = \bar{\zeta}$. Equation (3.113) then becomes,

$$\bar{E}(\lambda, \mu) = \frac{L}{R}\left(\bar{\omega} - \bar{P}\mu^2\lambda\right) \tag{3.114}$$

3. We know from equations (3.88) that the equilibrium condition (with λ fixed) is,

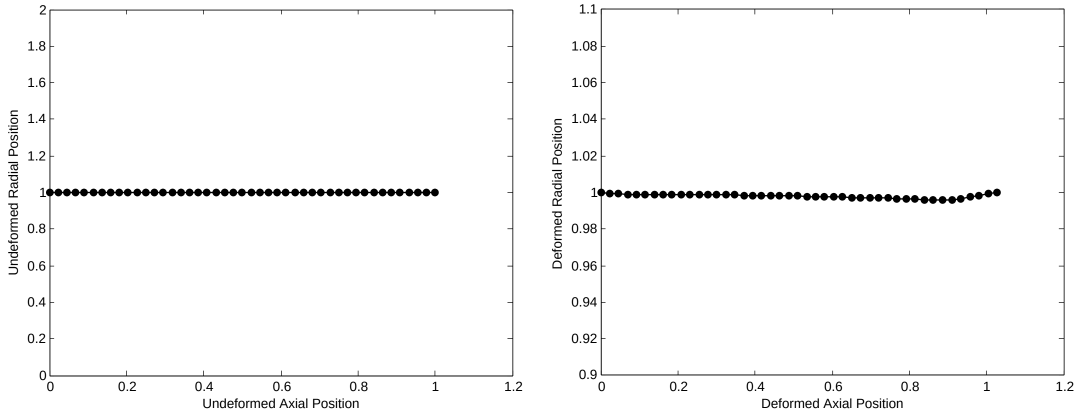

(a) $\lambda = 1.000$

(b) $\lambda = 1.025$

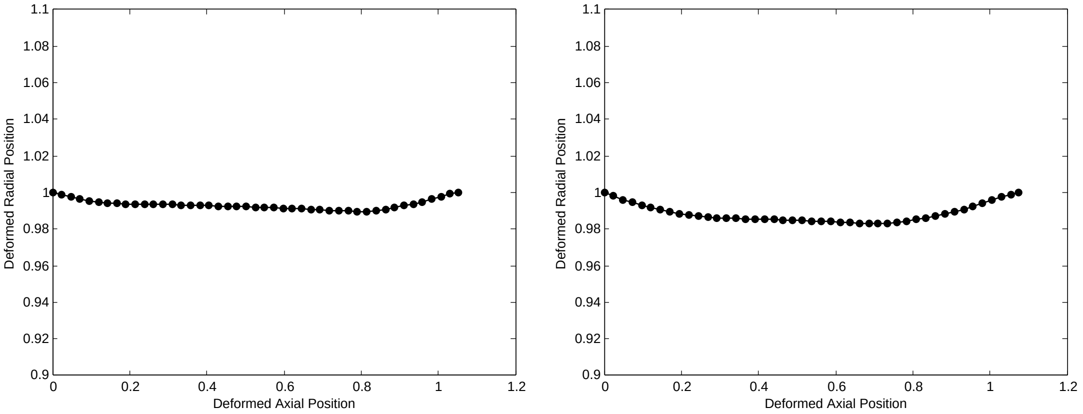

(c) $\lambda = 1.050$

(d) $\lambda = 1.075$

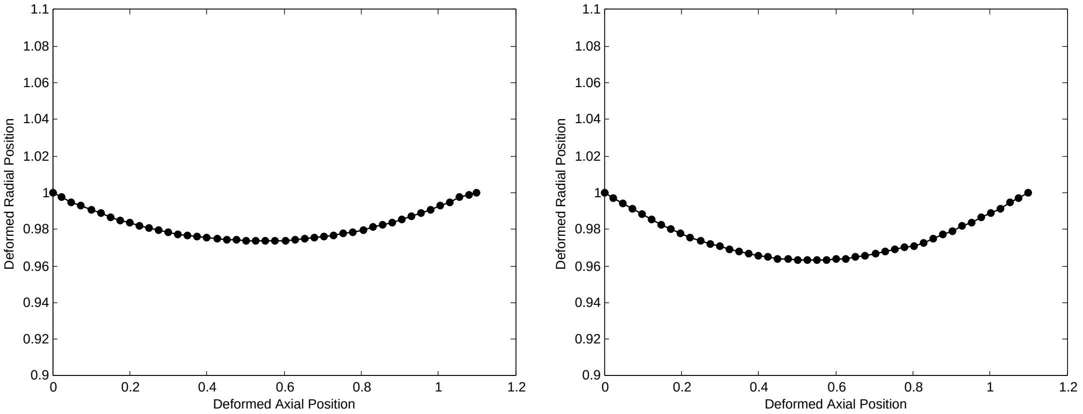

(e) $\lambda = 1.100$

(f) $\lambda = 1.100$, equilibrium

Figure 3.6: Model validation; necking from pure axial stretch

$$\frac{\partial \bar{E}(\lambda,\mu)}{\partial \mu} = \frac{L}{R}\Big(\frac{\partial \bar{\omega}}{\partial \mu} - 2\bar{P}\mu\lambda\Big) = 0, \tag{3.115}$$

and solving for our dimensionless pressure, $\bar{P}$ substituting our prescribed radial stretch, μ^* we have,

$$\bar{P} = \frac{1}{2\lambda\mu^*}\Big(\frac{\partial \bar{\omega}}{\partial \mu}\Big)_{\mu=\mu^*}. \tag{3.116}$$

4. Now we can prescribe axial and constant radial stretches (e.g. $\lambda = 1.1$ and $\mu^* = 1.1$) and given a strain energy function (e.g. equation (3.85)) and material constants, we can solve for $\bar{P}$. To check our numerical tool, we simply apply the axial stretch, then increment the pressure $\bar{P}$, wait until we have reached equilibrium (i.e. the transients have dampened out) and check that our deformed configuration is a *cylinder* with constant radial stretch $\mu^* = 1.1$.

We find that in performing this procedure we get and error of approximately 1.2% (i.e. $\mu^* = 1.1$+/-0.013) which is acceptable considering the rate dependency of the problem and the error tolerances of our numerical schemes (i.e. forward and backward Euler).

3.11.2 Various Initial Boundary Value Problems (IBVP's)

The following is a set of IBVP's investigating the behavior of our membrane under various conditions.

Investigation 1 - Fixed axial stretch and pressure, track the volume at various γ over time

Increment the axial stretch to $\lambda = 1.1$. When equilibrium is reached (to within a prescribed tolerance), inflate to a fixed pressure of $\bar{P} = 0.50$. As the tube inflates, track the volume at each time step for different values of the material parameter, γ from the constitutive equation (3.85) - i.e. $\bar{\omega}(\lambda,\mu) = \frac{1}{2\gamma}\Big(e^{\gamma(i-3)} - 1\Big)$. Figure (3.7) shows that for smaller values of γ, the tube expands to a larger volume; i.e. the material is weaker and stretches more radially to the same fixed internal pressure. This is consistent with intuitive predictions. Notice that the initial portion of the curve is the same for all values of γ. This period of time corresponds to the tube transitioning from a necked-in, concave shape to a convex, bulged out profile. The material provides little resistance as it snaps through until the pressure draws the membrane tight again; the volume at which this happens clearly depends on γ.

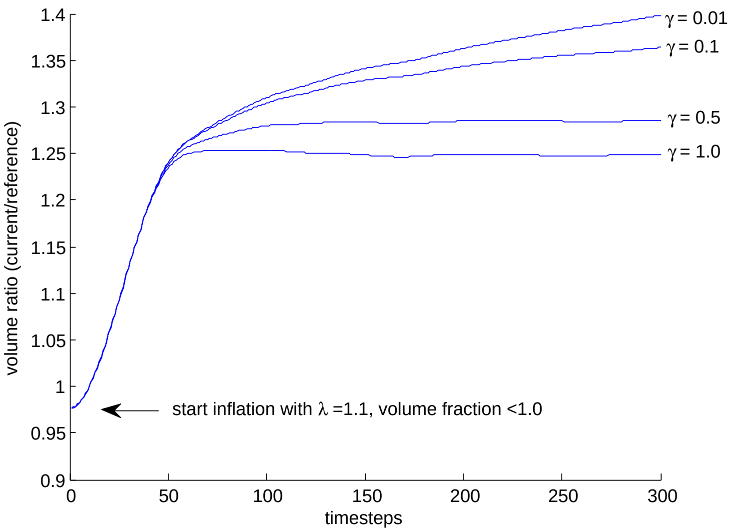

Figure 3.7: Modeling deformed segment volume as a function of material stiffness for fixed internal pressure and axial stretch

Investigation 2 - Axial stretch with incremented pressure

Fix $\gamma = 0.5$ and increment the axial stretch λ to 10%. The dimensionless pressure is then incremented to a maximum of $\bar{P} = 2.5$. As this model is viscoelastic, it may be useful to conduct a parameter study on the effects of various stretch or inflation *rates* on the overall deformation of the tube. The following is one such example of the deformation given certain material parameters (i.e. γ and the kinematic viscosity, ν) and a rate of stretch and inflation. The unsymmetrical deformation of the tube is due to dynamic effects from first stretching, then inflating. That is, a wave is propagating along the material from the initial stretch (a viscoelastic effect) which causes the bulge to sway axially as the pressure is increased.

Investigation 3 - Inflation *rate* effects on final tube volume as seen by varying the kinematic viscosity coefficient, $\bar{\nu}$

Here we fix the axial stretch, $\lambda = 1.1$ (i.e. a 10% stretch) and inflate at a fixed *rate* to a dimensionless pressure, arbitrarily set to $\bar{P} = 3.0$. We then vary the dimensionless kinematic viscosity coefficient of the material, $\bar{\nu}$. Figure (3.9) shows traces of the material response. As would be expected, as the viscosity coefficient is increased, the material is more resistant to our particular rate of inflation. Hence, the volume at our end pressure is lower. We can see that below $\bar{\nu} = 0.005$, the slope increases more dramatically indicating the material undergoing very large

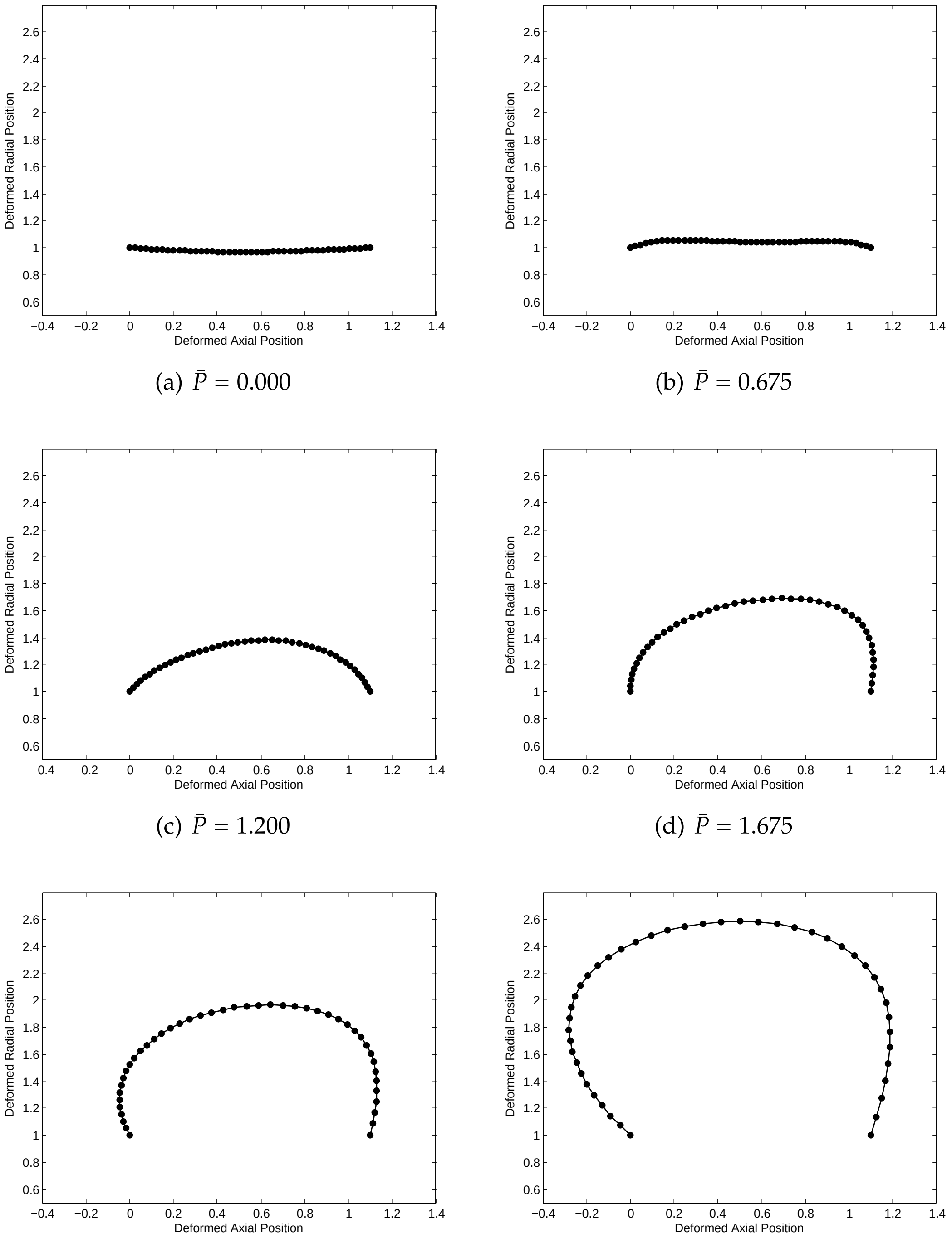

(a) $\bar{P} = 0.000$

(b) $\bar{P} = 0.675$

(c) $\bar{P} = 1.200$

(d) $\bar{P} = 1.675$

(e) $\bar{P} = 2.000$

(f) $\bar{P} = 2.500$

Figure 3.8: An example of viscoelastic effects

strains in a short time - eventually leading to material rupture, or membrane burst. Also recall that we are implementing our viscosity through the definition of our first Piola-Kirchhoff stress (equation (3.23)) rather than through the particular constitutive equation we are using.

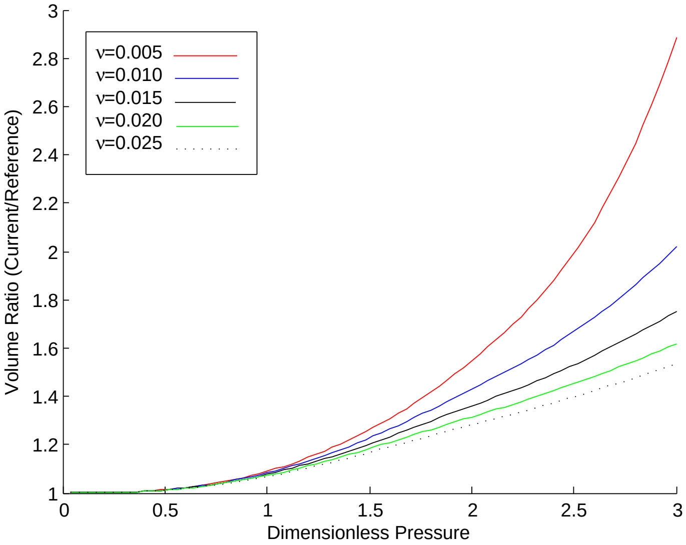

Figure 3.9: Modeling viscoelastic effects related to segment volume

Investigation 4 - How local changes in material properties (i.e. γ) change the overall inflation profile

Here we again increment the axial stretch to a maximum of 10 % (i.e. $\lambda = 1.1$) and inflate at a fixed rate to a dimensionless pressure, arbitrarily set to $\bar{P} = 5.0$. We prescribe a region on the network where the material constant that represents the stiffness or health of the tissue, γ, for our constitutive equation $\bar{\omega}(\lambda, \mu) = \frac{1}{2\gamma}\left(e^{\gamma(i-3)} - 1\right)$ is *lower* than for the rest of the network. Figure (3.10) shows how material inhomogeneities cause the membrane to deform considerably differently under internal pressure than a homogeneous membrane with constant γ (here, $\gamma = 10$). Note how the locally soft region (3.10 (b)) still allows a more-or-less symmetric bulge whereas the locally stiff region (3.10 (c)) creates a very different profile.

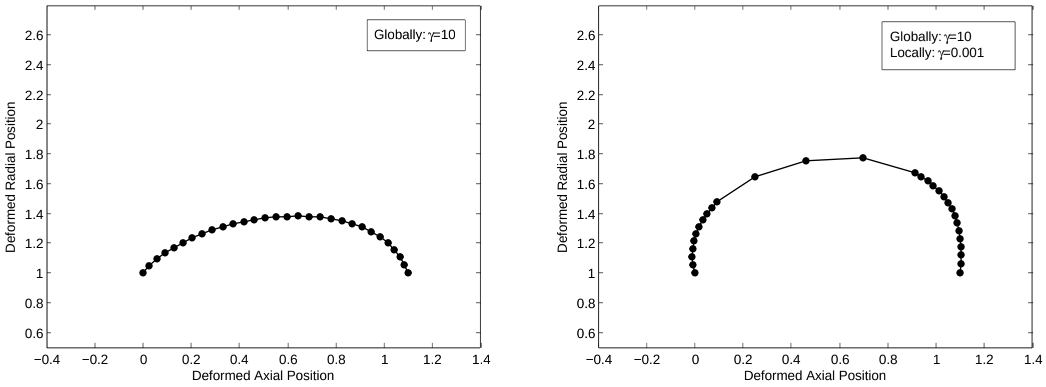

(a) Homogeneous Network (b) Heterogeneous Network - soft local region

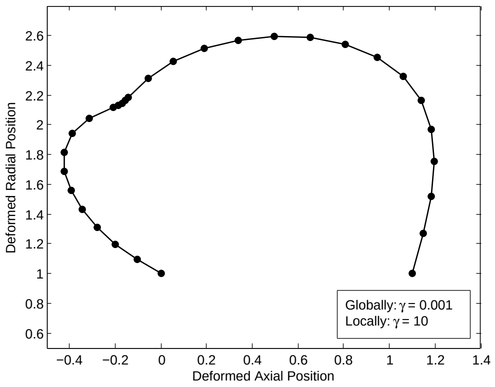

(c) Heterogeneous Network - stiff local region

Figure 3.10: Modeling inhomogeneities; local lesions in the vessel wall

Chapter 4

The Arterial Wall as a 3D, Two-Layer, Fiber-Reinforced Composite

Because of the material, structural and geometric complexities of biological tissues, as well as the spatially non-uniform and time-dependent boundary conditions, closed form solutions of the majority of relevant initial-value problems are near impossible to attain. Therefore, the study of biological tissues require a constitutive theory of finite elasticity applied to a numerical finite element framework. Consequently, these problems also require more computational resources and a post-processing graphics capability to display three-dimensional results. For a comprehensive review of other finite element models in the literature for arterial wall mechanics see Simon et al. [39].

In this section we seek to solve the continuum formulation of the equations of motion for a thick-walled cylinder (i.e. artery) under transmural (internal, radial) pressure and perivascular constraints (i.e. axial stretch) using a total Lagrangian development of the finite element method with time stepping and a fixed point iteration at each time step.

4.1 Mathematical Framework

4.1.1 Measures of Stress

Definitions of stresses used in this study

In nonlinear problems, various stress measures can be defined. We will follow the definitions given in the text by Belytschko et al. [40] and therein refer the reader for a more detailed development.

We will consider three measures of stress:

1. The (true) Cauchy stress tensor, σ

2. The nominal stress tensor **P** which we define as *the transpose* of the first Piola-Kirchhoff (PK1) stress tensor
3. The second Piola-Kirchhoff (PK2) stress tensor, **S**

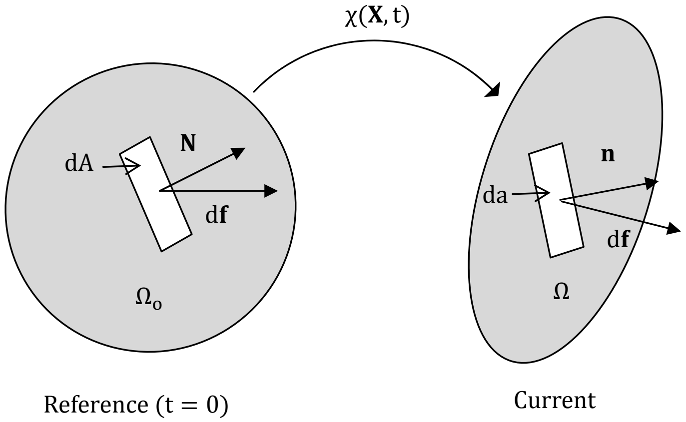

Figure 4.1: Definitions of 3D stress measures

Note that the nomenclature for the nominal stress is often contradictory; Belytschko et al. [40] and Ogden [37] use the definition given here, whereas many authors define **P** as the first Piola-Kirchhoff stress. It is important to note that the nominal stress is not symmetric.
The stresses are defined by Cauchy's law,

$$\mathbf{n} \cdot \sigma da = d\mathbf{f} = \mathbf{t} da \tag{4.1}$$

where **t** is the traction (force per unit area, *da*) in the current configuration and **n** is the unit normal to that area. In the reference configuration the counterpart to (4.1) is,

$$\mathbf{N} \cdot \mathbf{P} dA = d\mathbf{f} = \mathbf{p} dA \tag{4.2}$$

where **p** is the traction (force per unit area, *dA*) in the reference configuration and **N** is the unit normal to that area. Note that we relate the tractions by assuming the differential force $d\mathbf{f}$ is constant in both configurations; i.e. $d\mathbf{f} = \mathbf{t}da = \mathbf{p}dA$. The PK2 stress is defined as,

$$\mathbf{N} \cdot \mathbf{S} dA = \mathbf{F}^{-1} \cdot \mathbf{p} dA \tag{4.3}$$

Transformation between stresses

The relations between the stresses are obtained by using (4.1) - (4.3) as well as Nanson's law which relates the current normal to the reference normal by the following,

$$\mathbf{n}dA = J\mathbf{F}^{-T}\mathbf{N}dA \tag{4.4}$$

For brevity, we will only report the relationships between the three stresses and refer the reader to texts on continuum mechanics (e.g. [40]) for their full development. It should be noted that although, for convenience, we will formulate our initial value problem over the reference configuration of our body (i.e. artery), we will post-process certain quantities in the current configuration. Specifically, we will assess the Cauchy stress components for a measure of the "true" stress of the body at that point in time. The relations between the stresses are the following,

	Cauchy stress σ	Nominal stress $\mathbf{P}$	2nd Piola-Kirchhoff stress (PK2) $\mathbf{S}$
$\sigma =$	-	$J^{-1}\mathbf{F}\cdot\mathbf{P}$	$J^{-1}\mathbf{F}\cdot\mathbf{S}\cdot\mathbf{F}^T$
$\mathbf{P} =$	$J\mathbf{F}^{-1}\cdot\sigma$	-	$\mathbf{S}\cdot\mathbf{F}^T$
$\mathbf{S} =$	$J\mathbf{F}^{-1}\cdot\sigma\cdot\mathbf{F}^{-T}$	$\mathbf{P}\cdot\mathbf{F}^{-T}$	-

Table 4.1: Transformation between 3D stress measures

As a convenient *scalar* stress measure, we will use the Von Mises (or "equivalent tensile") stress for multiaxial loading conditions, defined as the following,

$$\sigma_{VM} = \sqrt{\frac{\left(\sigma_{11}-\sigma_{22}\right)^2 + \left(\sigma_{22}-\sigma_{33}\right)^2 + \left(\sigma_{11}-\sigma_{33}\right)^2 + 6\left(\sigma_{12}^2+\sigma_{23}^2+\sigma_{13}^2\right)}{2}} \tag{4.5}$$

The repeated subscripts indicate stress along the principal axes and the mixed subscripts indicate the components of shear stress.

4.1.2 Equations of Motion

The Lagrangian form of Cauchy's first equation of motion for a material point (i.e. the "strong form") is the following,

$$Div(\mathbf{P}) + \rho_0\mathbf{b} = \rho_0\ddot{\mathbf{u}}, \quad \textbf{or} \quad \frac{\partial P_{Ai}}{\partial X_A} + \rho_0 b_i = \rho_0 \ddot{u}_i, \tag{4.6}$$

where, $\frac{\partial P_{Ai}}{\partial X_A}$ denotes the divergence in the reference coordinates $\mathbf{X}$ of the nominal stress, $\mathbf{P}$. The body forces are $\mathbf{b}$ and the change in linear momentum is given by $\ddot{\mathbf{u}}$ (where $\ddot{()} \equiv \frac{d^2()}{dt^2}$). We also note that, according to the conservation of mass, the Jacobian $J \equiv det(\mathbf{F}) = det(\frac{d\mathbf{x}}{d\mathbf{X}})$ and density ρ are related in the current and reference configurations by the following, $\rho J = \rho_0 J_0 = \rho_0$.

We further employ the conservation of angular momentum (which says the stress field in the body must be symmetric) as defined with the deformation gradient $\mathbf{F}$ and the nominal stress as the following, $F_{iA}P_{Ak} = F_{kA}P_{Ai}$ (or equivalently, $\sigma_{ik} = \sigma_{ki}$).

In addition to the differential equations (4.6), our arterial section is subject to the following boundary and initial conditions.

4.1.3 Boundary and Initial Conditions

For any mechanical system, the same component of traction and displacement cannot be prescribed at the same point on the boundary of a body. Therefore, we will consider a partition of the boundary in the form $\Gamma = \Gamma_u \cup \Gamma_t$ (with $\Gamma_u \cap \Gamma_t = 0$). We impose a Dirichlet condition on the portion of the boundary Γ_u and a Neumann condition on the portion of the boundary Γ_t. For our Lagrangian formulation, the tractions are prescribed in units of force per unit *undeformed* area. Hence, the (Piola) traction $\mathbf{p}$ on the portion of the boundary Γ_t is defined in terms of the unit normal $\mathbf{N}$, in component form as $p_i \equiv P_{iA}N_A$. However, since our applied traction is an internal pressure that remains normal to the inner surface of the tube, we are really applying a Cauchy traction, say $\mathbf{t}^*$. Assuming some prescribed displacement on Γ_u, say $\mathbf{u}^*$, the boundary conditions are therefore summarized as the following (see Fig. 4.2),

$$\begin{aligned} \mathbf{u} = \mathbf{u}^* &\text{ on } \Gamma_u \text{ (front end)} \\ \mathbf{u} = \mathbf{0} &\text{ on } \Gamma_u \text{ (back end)} \\ \mathbf{t} = \mathbf{t}^* &\text{ on } \Gamma_t \text{ (inner surface)} \\ \mathbf{t} = \mathbf{0} &\text{ on } \Gamma_t \text{ (outer surface)} \end{aligned} \tag{4.7}$$

In this study, we require that there be no discontinuities in the traction throughout the domain of the body, or across interfaces, Γ_{int}. In other words, the traction is assumed to be continuously differentiable, i.e. C^0, everywhere in our domain. In terms of the nominal stress (i.e. $\mathbf{P}$) we can show this as,

$$[[p_i]] \equiv [[P_{iA}N_A]] = 0 \tag{4.8}$$

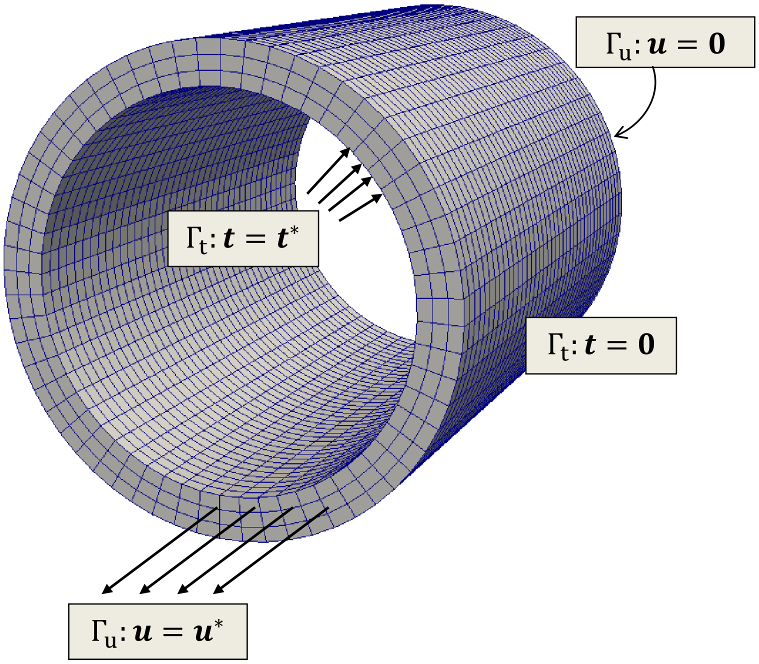

Figure 4.2: Boundary Conditions

where we define the operator $[[a]] \equiv a^{+} - a^{-}$ and in general, $a^{+/-}$ are the values of a (some general field quantity) approaching from opposite directions at a material point.

4.1.4 Referential description for the current traction

More specific to the geometry of our tube, we will rigidly constrain each capped-end (thus Γ_u is on the faces of the elements at the tube ends and this is the *only* place we will prescribe a displacement) and apply a transmural (radial, internal) pressure normal to the inner surface of the tube (which we define as Γ_t). The traction on the outside surface of the tube is set to zero (also Γ_t). Since we are applying a traction on the current, deformed configuration of the tube, we are actually applying a Cauchy traction (i.e. a force per unit *current* area). Therefore, in order to integrate this traction over the *reference* area of the element (which is necessary for our Lagrangian formulation), we will need to "pull-back" the Cauchy traction.

The Cauchy traction vector is defined as the following,

$$\mathbf{t} = -p^{*}\mathbf{n}, \tag{4.9}$$

where, p^{*} is the scalar pressure and $\mathbf{n}$ is the unit normal on the current (deformed) surface. We can relate the two surface tractions by integrating each over the surface area in the reference (Γ_o) and current (Γ) configurations.

$$\begin{aligned} \int\limits_{\Gamma_o} \mathbf{p}dA &= \int\limits_{\Gamma} \mathbf{t}da \\ &= \int\limits_{\Gamma} p^{*}\mathbf{n}da \end{aligned} \tag{4.10}$$

To relate the surface normals in the current and reference configuration, we use the familiar Nanson's formula, $\mathbf{n}da = J\mathbf{F}^{-T} \cdot \mathbf{N}dA$, and substituting into the above expression yields,

$$\int\limits_{\Gamma_o} \mathbf{p}dA = \int\limits_{\Gamma} p^{*}J\mathbf{F}^{-T} \cdot \mathbf{N}dA \tag{4.11}$$

Implementing this numerically, we will slowly increment the pressure, p^{*}, with each small time step.

4.1.5 Initial Conditions

We assume the following initial conditions for the displacement and velocity fields,

$$\mathbf{u}(\mathbf{X}, t) = \mathbf{u_o} \;\text{ on } \Gamma_{u,o} \tag{4.12}$$

$$\dot{\mathbf{u}}(\mathbf{X}, \mathbf{t}) = \dot{\mathbf{u}}_\mathbf{o} \;\text{ on }\; \Gamma_{u,o} \tag{4.13}$$

where, of course $\dot{(\;)} \equiv \frac{d}{dt}(\;)$.

4.2 The Finite Element Method

4.2.1 The total Lagrangian formulation

The weak, or dual, form of our Lagrangian formulation is obtained by multiplying the momentum equation (4.6) by a kinematically admissible test function, say $\mathbf{v}$ (i.e. for all $\mathbf{v} = \mathbf{d}$ where $\mathbf{u} = \mathbf{d}$, some arbitrary displacement, but $\mathbf{v} = \mathbf{0}$ on the boundary Γ_u) and integrating over the *reference configuration*.

Define the spaces of approximation of the test and the trial functions as the following,

$$\begin{aligned} \mathbf{u}(\mathbf{X}, t) \in H^1(\Omega_o),\; \mathbf{u}|_{\Gamma_\mathbf{u}} &= \mathbf{d} \\ \mathbf{v}(\mathbf{X}) \in H^1(\Omega_o),\; \mathbf{v}|_{\Gamma_\mathbf{u}} &= \mathbf{0} \end{aligned} \tag{4.14}$$

Where we represent the Hilbertian-Sobolev space as $H^1(\Omega_o)$; or, the usual space of scalar functions with partial derivatives of order less than unity in the space $L^2(\Omega_o)$. In other words $\mathbf{u}$ is square integrable. Mathematically (suppressing the arguments), we say this with the following,

$$\mathbf{u} \in H^1(\Omega_o)\; if\; ||\mathbf{u}||^2_{H^1(\Omega_o)} \equiv \int_{\Omega_o} \frac{\partial \mathbf{u}}{\partial \mathbf{X}} : \frac{\partial \mathbf{u}}{\partial \mathbf{X}} d\mathbf{X} + \int_{\Omega_o} \mathbf{u} \cdot \mathbf{u} d\mathbf{X} < \infty \tag{4.15}$$

Recall that a norm has three main characteristics for any vectors $\mathbf{u}$ and $\mathbf{v}$ such that $||\mathbf{u}|| < \infty$ $||\mathbf{v}|| < \infty$ (i.e. the norms remain bounded):

1. $||\mathbf{u}|| > 0$ and $||\mathbf{u}|| = 0$ iff $\mathbf{u} = \mathbf{0}$

2. $||\mathbf{u} + \mathbf{v}|| \leq ||\mathbf{u}|| + ||\mathbf{u}||$ and

3. $||\alpha\mathbf{u}|| \leq |\alpha|||\mathbf{u}||$ where α is a scalar

Henceforth we will develop our equations in indicial (or component) notation to keep track of the reference and current bases of various tensors more easily. Therefore, multiplying (4.6) by our test function and integrating over the initial configuration of the domain yields,

$$\int\limits_{\Omega_o} \left(\frac{\partial P_{Ai}}{\partial X_A} + \rho_0 b_i - \rho_0 \ddot{u}_i \right) v_i \, d\Omega_o = 0 \tag{4.16}$$

In the above equation, the nominal stress is a function of the trial displacements via the strain energy function and the strain-displacement equation. Therefore, this weak form is not useful as it requires the trial displacements be C^1 continuous (we want continuously differentiable, or C^0). To eliminate the derivative on the nominal stress in (4.16), we can use the following,

$$\frac{\partial P_{Ai}}{\partial X_A} v_i = \frac{\partial}{\partial X_A} \left(P_{Ai} v_i \right) - \frac{\partial v_i}{\partial X_A} P_{Ai} \tag{4.17}$$

Therefore, we have,

$$\int\limits_{\Omega_o} \frac{\partial}{\partial X_A} \left(P_{Ai} v_i \right) d\Omega_o - \int\limits_{\Omega_o} \frac{\partial v_i}{\partial X_A} P_{Ai} d\Omega_o + \rho_0 \int\limits_{\Omega_o} b_i v_i d\Omega_o - \rho_0 \int\limits_{\Omega_o} \ddot{u}_i v_i d\Omega_o = 0 \tag{4.18}$$

We seek to express the first integral, above, over the boundary of our domain, Ω_o. If we define the function $f(\mathbf{X}) \equiv \mathbf{Pv}$, we must then ask ourselves if $f(\mathbf{X})$ is continually differentiable, i.e. a C^0 function, over Ω_o. Here, we will allow for the possibility that $f(\mathbf{X})$ *may have* derivatives that are *discontinuous* on surfaces in three dimensions. Therefore, Ω_o must be split into subdomains so that the function $f(\mathbf{X})$ is C^0 within each subdomain. Discontinuities in the derivatives of $f(\mathbf{X})$ will then occur on the interfaces between the subdomains. If we use Gauss's theorem and apply it to each of the subdomains then sum the result we obtain the following,

$$\int\limits_{\Omega_o} \frac{\partial}{\partial X_A} \left(P_{Ai} v_i \right) d\Omega_o = \int\limits_{\Gamma_o} N_A P_{Ai} v_i \, d\Gamma_o + \int\limits_{\Gamma_{o,int}} [[P_{iA} N_A]] v_i \, d\Gamma_o \tag{4.19}$$

By (4.8), the last integral in (4.19) is zero and our weak form becomes,

$$\int\limits_{\Gamma_o} p_i v_i \, d\Gamma_o - \int\limits_{\Omega_o} \frac{\partial v_i}{\partial X_A} P_{Ai} d\Omega_o + \rho_0 \int\limits_{\Omega_o} b_i v_i d\Omega_o - \rho_0 \int\limits_{\Omega_o} \ddot{u}_i v_i d\Omega_o = 0 \tag{4.20}$$

We then split the first integral in (4.20) into the traction and displacement reference domains (i.e. $\Gamma = \Gamma_u \cup \Gamma_t$) as follows,

$$\begin{aligned}\int\limits_{\Gamma_o} p_i v_i \, d\Gamma_o &= \int\limits_{\Gamma_{o,u}} p_i v_i \, d\Gamma_o + \int\limits_{\Gamma_{o,t}} p_i v_i \, d\Gamma_o \\ &= \int\limits_{\Gamma_{o,t}} p_i v_i \, d\Gamma_o \end{aligned} \tag{4.21}$$

The first integral on the RHS of (4.21) is zero as we know that there is *no traction* on the displacement portion of the boundary, or, $\mathbf{p} = \mathbf{0}$ on Γ_u.
We then have the following weak Lagrangian formulation,

$$\int\limits_{\Gamma_{o,t}} p_i v_i \, d\Gamma_o - \int\limits_{\Omega_o} \frac{\partial v_i}{\partial X_A} P_{Ai} \, d\Omega_o + \rho_0 \int\limits_{\Omega_o} b_i v_i \, d\Omega_o - \rho_0 \int\limits_{\Omega_o} \ddot{u}_i v_i \, d\Omega_o = 0 \tag{4.22}$$

4.2.2 Three Dimensional Discretization

We consider a Lagrangian mesh of the domain Ω_o. The finite element approximation to the motion $\mathbf{x}(\mathbf{X}, t)$ is given (in component form) by,

$$x_i(\mathbf{X}, t) = \sum_{I=1}^{N} x_{iI}(t) \Phi_I(\mathbf{X}) \tag{4.23}$$

Lower case subscripts are used for components, and the upper case subscripts for nodal values. The nodal coordinates in the current configuration are given by x_{iI} and in the reference configuration by X_{iI}, where, $I = 1$ to N (i.e. for three dimensions, there are eight nodes so N=8). Φ_I are the (interpolation) basis functions that are functions of the material (i.e. Lagrangian) coordinates: X_1, X_2, X_3.
We will define the nodal displacement field by the following,

$$u_i(\mathbf{X}, t) = x_i(\mathbf{X}, t) - X_i = \sum_{I=1}^{N} u_{iI}(t) \Phi_I(\mathbf{X}) \tag{4.24}$$

where, $u_{iI}(t)$ are time-dependent scalar displacements at each of the nodes.
We will use a similar form for a set of test functions (note the test functions are not a function of time),

$$v_i(\mathbf{X}) = \sum_{I=1}^{N} v_{iI} \Phi_I(\mathbf{X}). \tag{4.25}$$

4.2.3 Internal and External Forces via Virtual Work

We can define the internal and external forces in and on our domain with the concept of virtual work. That is, any force (i.e. external or internal), appropriately multiplied by an arbitrary increment of displacement (i.e. "test function"), v_i, produces an increment of work, say W. We can note that the integrals in our weak form (4.22) are of this quality. Coupled with the approximations for our trial and test functions (4.24), (4.25), respectively, we can define the internal nodal forces through the internal virtual work, by the following,

$$W^{int} \equiv v_{iI} f_{iI}^{int} = v_{iI} \int\limits_{\Omega_o} \frac{\partial \Phi_I}{\partial X_A} P_{Ai} \, d\Omega_o \tag{4.26}$$

Clearly,

$$\begin{aligned} f_{iI}^{int} &= \int\limits_{\Omega_o} \frac{\partial \Phi_I}{\partial X_A} P_{Ai} \, d\Omega_o \\ &= \int\limits_{\Omega_o} \frac{\partial \Phi_I}{\partial X_A} F_{ik} S_{Ak} \, d\Omega_o \\ &= \int\limits_{\Omega_o} \left(\frac{\partial \Phi_I}{\partial X_A} F_{ik} \right)_{sym(A,k)} S_{Ak} \, d\Omega_o \\ &= \int\limits_{\Omega_o} \left(\frac{\partial \Phi_I}{\partial X_A} \frac{\partial x_i}{\partial X_k} \right)_{sym(A,k)} S_{Ak} \, d\Omega_o \\ &= \int\limits_{\Omega_o} B_{AkiI} S_{Ak} \, d\Omega_o \end{aligned} \tag{4.27}$$

We use the familiar deformation gradient, $\mathbf{F}$, which is defined as, $F_{ik} = \frac{\partial x_i}{\partial X_k}$. For convenience, we have chosen to use the second Piola stress, $\mathbf{S}$, given by $P_{iA} = F_{ik} S_{Ak}$. Since $\mathbf{S}$ is symmetric, it is further convenient to define a tensor, $\mathbf{B}$, (following Belytschko et al. [40]) as the following,

$$B_{AkiI} = \left(\frac{\partial \Phi_I}{\partial X_A} \frac{\partial x_i}{\partial X_k} \right)_{sym(A,k)} \tag{4.28}$$

Similarly, we can define the define the virtual work done by the *external* nodal forces as,

$$W^{ext} \equiv v_{iI} f_{iI}^{ext} = v_{iI} \left[\rho_0 \int\limits_{\Omega_o} \Phi_I b_i \, d\Omega_o + \int\limits_{\Gamma_{o,t}} \Phi_I p_i \, d\Gamma_o \right] \tag{4.29}$$

Thus,

$$f_{iI}^{ext} = \rho_0 \int\limits_{\Omega_o} \Phi_I b_i \, d\Omega_o + \int\limits_{\Gamma_{o,t}} \Phi_I p_i \, d\Gamma_o \tag{4.30}$$

Defining a nodal force that is equivalent to an inertial force, together with our approximations from (4.24), (4.25), we can write,

$$W^{kin} \equiv v_{iI} f_{iI}^{kin} = \int\limits_{\Omega_o} v_i \rho_0 \ddot{u}_i \, d\Omega_o = v_{iI} \int\limits_{\Omega_o} \rho_0 \Phi_I \Phi_J d\Omega_o \ddot{u}_{jJ} \tag{4.31}$$

Define the mass matrix (which is time invariant in our Lagrangian mesh) by the following,

$$M_{ijIJ} \equiv \delta_{ij} \int\limits_{\Omega_o} \rho_0 \Phi_I \Phi_J d\Omega_o. \tag{4.32}$$

Substituting the above expressions into the weak form, (4.22), we have,

$$v_{iI} \left(f_{iI}^{ext} - f_{iI}^{int} - M_{ijIJ} \ddot{u}_{jJ} \right) = 0, \; \forall \, (I, i) \notin \Gamma_{o,u} \tag{4.33}$$

The above applies to all arbitrary values of nodal displacements, v_{iI}, that *are not constrained* by displacement boundary conditions, therefore it follows that,

$$M_{ijIJ} \ddot{u}_{jJ} + f_{iI}^{int} = f_{iI}^{ext}, \; \forall \, (I, i) \notin \Gamma_{o,u} \tag{4.34}$$

Note that (4.34) represent the discrete equations for the total Lagrangian formulation.

Substituting our expressions above into (4.34) and rearranging, we find our new weak form to be the following,

$$\delta_{ij} \int\limits_{\Omega_o} \rho_0 \Phi_I \Phi_J d\Omega_o \ddot{u}_{jJ} = \rho_0 \int\limits_{\Omega_o} \Phi_I b_i \, d\Omega_o + \int\limits_{\Gamma_{o,t}} \Phi_I p_i \, d\Gamma_o - \int\limits_{\Omega_o} B_{AkiI} S_{Ak} \, d\Omega_o \tag{4.35}$$

4.2.4 Mapping to the Parent Element

In order to numerically integrate (with, say, Gaussian quadrature) our Lagrangian weak form (4.35), we must first map our domain into a parent element. In three dimensions, our parent element is a unit cube with a body centered coordinate system of (ξ_1, ξ_2, ξ_3) (see Fig. 4.3).

We can define our mapping from reference element coordinates, $\mathbf{X}$, to parent element coordinates, $\widetilde{\mathbf{X}}$, by the following relation,

$$\mathbf{X} = \left(\widetilde{X}_{1I}\ \hat{\Phi}_I(\xi), \widetilde{X}_{2I}\ \hat{\Phi}_I(\xi), \widetilde{X}_{3I}\ \hat{\Phi}_I(\xi)\right) \tag{4.36}$$

The vector above is represented in component form where the first indice indicates the component $(1, 2, 3)$ and there is a sum over the eight nodes (per local element), $I = 1, 2, ..., 8$. From this relation, we can note the I^{th}-node basis function is equivalent to the I^{th}-node shape function,

$$\Phi_I(\mathbf{X}(\xi)) = \hat{\Phi}_I(\xi) \tag{4.37}$$

The eight master element shape functions form a nodal bases of trilinear approximation given by the following (see Fig. (4.3)),

$$\boxed{\begin{aligned}
\hat{\phi}_1 &= \tfrac{1}{8}(1-\xi_1)(1-\xi_2)(1-\xi_3)\\
\hat{\phi}_2 &= \tfrac{1}{8}(1+\xi_1)(1-\xi_2)(1-\xi_3)\\
\hat{\phi}_3 &= \tfrac{1}{8}(1+\xi_1)(1+\xi_2)(1-\xi_3)\\
\hat{\phi}_4 &= \tfrac{1}{8}(1-\xi_1)(1+\xi_2)(1-\xi_3)\\
\hat{\phi}_5 &= \tfrac{1}{8}(1-\xi_1)(1-\xi_2)(1+\xi_3)\\
\hat{\phi}_6 &= \tfrac{1}{8}(1+\xi_1)(1-\xi_2)(1+\xi_3)\\
\hat{\phi}_7 &= \tfrac{1}{8}(1+\xi_1)(1+\xi_2)(1+\xi_3)\\
\hat{\phi}_8 &= \tfrac{1}{8}(1-\xi_1)(1+\xi_2)(1+\xi_3)
\end{aligned}}$$

Table 4.2: shape functions

The mapping of infinitesimal line elements between the parent and reference domains is given by another deformation gradient defined as,

$$\mathbf{F}_\xi = \frac{\partial \mathbf{X}}{\partial \xi} \tag{4.38}$$

The Jacobian (the determinant of the deformation gradient) relates the volumes between the parent $(d\hat{\Omega}_0)$ and reference $(d\Omega_0)$ domains and is given by the following,

$$J_\xi \equiv det(\mathbf{F}_\xi) = \frac{d\Omega_0}{d\hat{\Omega}_0} \tag{4.39}$$

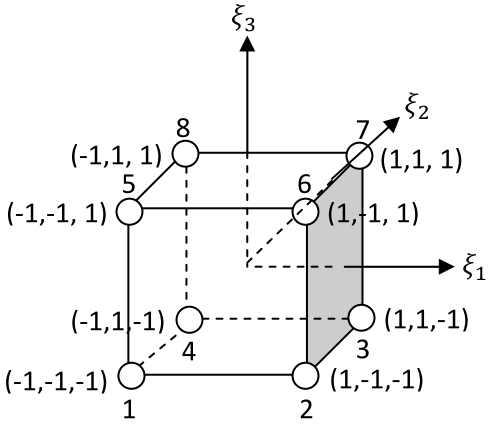

Figure 4.3: The master element: a trilinear hexahedron

Similarly, the surface Jacobian relates the surface areas between the parent ($d\hat{\Gamma}_o$) and reference ($d\Gamma_o$) domains and is given by,

$$J_{s\xi} = \frac{d\Gamma_o}{d\hat{\Gamma}_o} = \frac{d\Gamma_o}{4} \tag{4.40}$$

Note that the parent surface area of any face of the hexagonal element is 4.

It is useful to further modify our equation for the component form of B_{iAkI} given in (4.28) by expanding the first partial derivative and using the definitions of our deformation gradients,

$$\begin{aligned} B_{AkiI} &= \frac{\partial \Phi_I}{\partial X_A}\frac{\partial x_i}{\partial X_k} \\ &= \frac{\partial \hat{\Phi}_I}{\partial \xi_l}\frac{\partial \xi_l}{\partial X_A}\frac{\partial x_i}{\partial X_k} \\ &= \frac{\partial \hat{\Phi}_I}{\partial \xi_l}\left(F^{\xi}_{lA}\right)^{-1}\left(F_{ik}\right) \end{aligned} \tag{4.41}$$

Rearranging our equations of motion in (4.34) and substituting for each expression gives the following final result,

$$M_{ijIJ}\ddot{u}_{jJ} = f^{ext}_{iI} - f^{int}_{iI} \tag{4.42}$$

Where,

$$
\begin{aligned}
M_{ijIJ} &= \delta_{ij} \int\limits_{\hat{\Omega}_o} \rho_0 \hat{\Phi}_I \hat{\Phi}_J J_\xi d\hat{\Omega}_o \\
f_{iI}^{ext} &= \rho_0 \int\limits_{\hat{\Omega}_o} \hat{\Phi}_I b_i \, J_\xi d\hat{\Omega}_o \; + \int\limits_{\hat{\Gamma}_{o,t}} \hat{\Phi}_I p_i \, J_{s\xi} d\hat{\Gamma}_o \\
f_{iI}^{int} &= \int\limits_{\hat{\Omega}_o} \left(\frac{\partial \hat{\Phi}_I}{\partial \xi_l} \frac{\partial \xi_l}{\partial X_A} \frac{\partial x_i}{\partial X_k} \right) S_{Ak} \, J_\xi d\hat{\Omega}_o
\end{aligned}
\tag{4.43}
$$

4.3 Numerical Methods

4.3.1 A Fixed-Point Iteration at Each Time Step

In order to avoid computing the stiffness matrices of the body in solving for our displacement field (i.e. u_{jJ} in equation (4.42)), which is necessary if implementing numerical methods such as Newton's method or the Conjugate Gradient method (see Belytschko et al. [40]), we will utilize a fixed-point iteration (in time) scheme. The basic steps for this algorithm follow,

1. Consider the displacement field of the body to be represented by the vector, $\mathbf{u}$ and to simplify the notation, denote the displacement at times t, $t - \Delta t$ and $t + \Delta t$, by $\mathbf{u}^L$, $\mathbf{u}^{L-1}$ and $\mathbf{u}^{L+1}$, respectively.

2. Guess a displacement field, say $\mathbf{u}_o$, for all times: $\mathbf{u}^{L-1} = \mathbf{u}_o$, $\mathbf{u}^L = \mathbf{u}_o$ and $\mathbf{u}^{L+1} = \mathbf{u}_o$.

3. Define a tolerance for the iteration (i.e. some small scalar value), for example $TOL = 0.001$. Define another *relative* tolerance to be (initially) larger than TOL, for example $REL = 10$.

4. Now solve for the displacement $\mathbf{u}^{L+1}$ (if we are using an implicit method) based on a convergence criteria that $\mathbf{u}^{L+1}$ is sufficiently close to our guess $\mathbf{u}_o$. Use the letter K to indicate the iteration number.

   The algorithm for this would look something like the following,

   - For the first iterate (K=0) initialize the solution at all times with guess $\mathbf{u}_o$:
     $\mathbf{u}^{L-1,K} = \mathbf{u}_o$

$\mathbf{u}^{L,K} = \mathbf{u}_o$
$\mathbf{u}^{L+1,K} = \mathbf{u}_o$

- Set a relative tolerance and the desired iteration tolerance:
  REL = Large Number, TOL = Small Number

- Loop until REL < TOL (i.e. while REL > TOL, perform the following):
  Solve at the next iteration: $\mathbf{u}^{L+1,K+1} = F(\mathbf{u}^{L-1,K}, \mathbf{u}^{L,K}, \mathbf{u}^{L+1,K})$
  Compute the difference in iterates: REL = $\frac{\left(||\mathbf{u}^{L+1,K+1}||_2 - ||\mathbf{u}^{L+1,K}||_2\right)}{||\mathbf{u}^{L+1,K}||_2}$
  where, F represents some function of the displacements at each time.
  Update the solution: $\mathbf{u}^{L+1,K} = \mathbf{u}^{L+1,K+1}$

5. Note that we have used $|| \cdot ||_2$ to denote the 2-norm defined as,

$$||\mathbf{u}||_2 \equiv \left(\sum_{i=1}^{n} |u_i|^2 \right)^{1/2}, \tag{4.44}$$

   where, n represent the degrees of freedom of our system of equations.

4.3.2 Model Validation

Homogeneous Deformations

A useful check that we have implemented our numerical method correctly is by enforcing a homogeneous deformation on the boundary of the body and post-processing the average value of the deformation gradient over every element in the body. This procedure is outlined by the following steps.

1. Prescribe a homogeneous displacement, **u** to the *entire* boundary of the body (i.e. the artery). Mathematically, this would look like the following,

$$\mathbf{u} = \mathbf{A} \cdot \mathbf{X}, \tag{4.45}$$

   where **A** is a matrix of constants applied to the boundary in the reference configuration, **X** of the body. From the definition of displacement (i.e. $\mathbf{u} = \mathbf{x} - \mathbf{X}$, where **x** is the position vector in the current configuration), we may then say the following,

$$\begin{aligned} \mathbf{A} \cdot \mathbf{X} &= \mathbf{x} - \mathbf{X} \\ \mathbf{x} &= \mathbf{A} \cdot \mathbf{X} + \mathbf{X} \\ \mathbf{x} &= \big(\mathbf{A} + \mathbf{I}\big)\mathbf{X}. \end{aligned} \tag{4.46}$$

2. Taking the referential gradient of $\mathbf{x}$, gives us the deformation gradient $\mathbf{F}$,

$$Grad(\mathbf{x}) \equiv \mathbf{F} = \mathbf{A} + \mathbf{I}. \tag{4.47}$$

3. The average value over the body (mathematically shown by $\langle \cdot \rangle_\Omega$) of the deformation gradient should then equal our prescribed displacement of the boundary on the body. In other words,

$$\langle \mathbf{F} \rangle_\Omega = \mathbf{A} + \mathbf{I}. \tag{4.48}$$

4.3.3 Mesh Refinement

To convince ourselves that we have converged on the true solution, we must first conduct a numerical mesh refinement study. We will employ the commonly used energy criteria of successively refining the mesh until the total potential energy of the body is within a prescribed tolerance. Note that we are omitting the contribution of the kinetic energy as the loading in this study, for both modes of deformation (i.e. pure extension and extension with internal pressure) is extremely slow (e.g. 10% stretch and/or incremental pressure over 5-10 seconds) and thus, adds very little energy, relative to the potential energy, to the total system energy. The "final mesh" resolution, or converged-solution mesh, in general, depends on the specific mode of deformation of the body. However, our two modes of deformation, pure extension and extension with internal pressure, produce physically similar overall geometries; that is, purely stretching the cylindrical tube causes axisymmetric necking, whereas stretching and inflating produces axisymmetric bulging. Therefore, we will conduct only one successive mesh refinement and use this mesh for all subsequent loading scenarios.

Due to numerical stability concerns, the total number of elements is dictated by the aspect ratio of each element, or, the more "cubic" the element, the smoother and more stable the solution. Therefore, since the radial wall thickness is the smallest (by comparison) length scale of our body, the radial mesh (or number of elements in the radial direction) sets a lower bound on the number of elements in both the circumferential and axial directions. In other words, an element should have comparable length in each direction. Using the minimum number of radial elements (i.e. one element) for each layer (media $N_r^m = 1$, adventitia $N_r^a = 1$), we have found that the model remains stable, using a time step on the order of 10^{-7} seconds, with a lower bound of 12 elements in the circumferential (i.e. $N_\theta = 12$) and 6 elements in the axial (i.e. $N_z = 6$) directions (i.e."Mesh 1" in Tab. (4.3)). Hence, we consider this our coursest mesh. To refine the mesh, we add elements radially and adjust the number of elements in the other two directions to maintain stability. We have converged on the final mesh when the total strain energy (averaged over all the elements) of the body changes only by a small (prescribed) amount from successive refinements. Figure 4.4 illustrates the successive mesh refinements for pure axial extension.

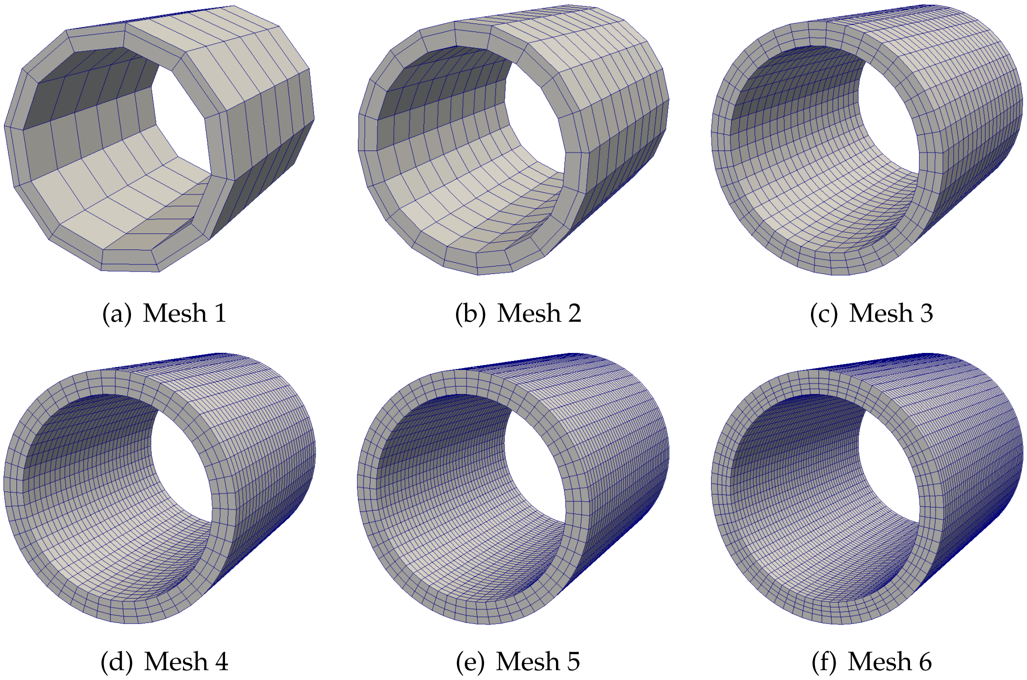
(a) Mesh 1 (b) Mesh 2 (c) Mesh 3

(d) Mesh 4 (e) Mesh 5 (f) Mesh 6

Figure 4.4: Refining the mesh

Table 4.3 summarizes the mesh refinement scheme for pure extension. Note that the column titled "P.E." lists the total *strain* energy of the body (in Joules) as there is no pressure applied in this mode of deformation and the kinetic energy is neglected due to the quasi-static nature of the loading (as described above).

This study will use Mesh number 5 as the CPU time for a more refined mesh (e.g. Mesh 6) prohibits efficient parameter studies.

Note that the Degrees of Freedom (DOF) for the system are found by the following formula, DOF= $(N_\theta)(N_{rm} + N_{ra} + 1)(N_z + 1)$. Figure 4.5 shows the convergence of the mesh for pure axial extension.

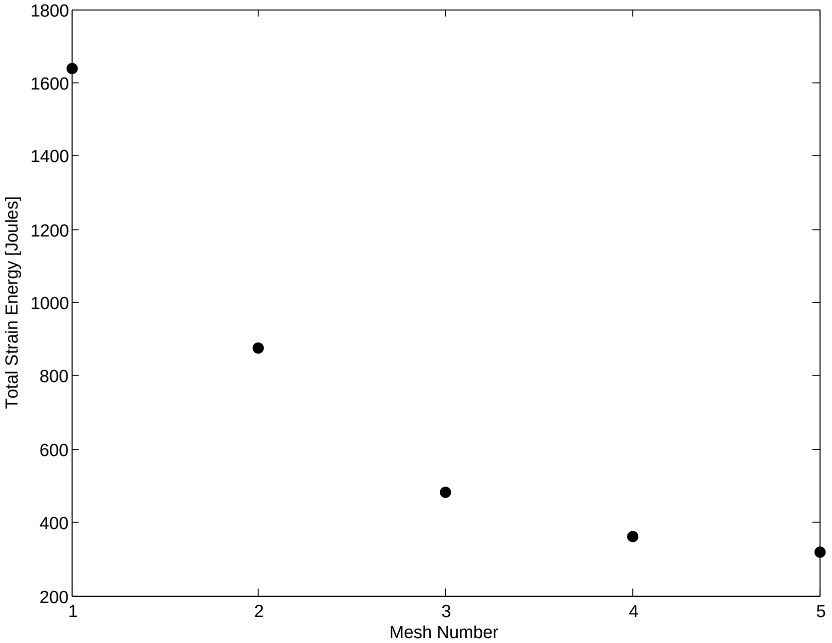

Figure 4.5: Refining the mesh; total system strain energy for 10% axial stretch (see Table 4.3)

Mesh No.	N_θ	N_{rm}	N_{ra}	N_z	DOF	P.E. [Joules]	CPU Time [hrs]
1	12	1	1	6	756	1,636.96	2.5
2	20	1	1	10	1,980	875.97	6.7
3	40	2	1	20	10,080	480.60	36.7
4	50	2	1	30	18,600	361.87	75
5	60	2	1	40	29,520	318.20	111.7
6	70	3	1	50	53,550	unk	215

Table 4.3: Mesh refinement for pure axial stretch

4.4 Basic Constitutive Laws for Infinitesimal and Finite Strains

4.4.1 Infinitesimal Strain

Kirchhoff Saint-Venant

The simplest small-strain constitutive law is by Kirchhoff-Saint Venant (K-SV). In terms of a strain energy function, the model has the following quadratic (in deformation) form,

$$W = \frac{1}{2}\mathbf{E} : \bar{\mathbf{C}} : \mathbf{E} \tag{4.49}$$

where, $\bar{\mathbf{C}}$ is a fourth-order tensor of elastic material constants and $\mathbf{E} = \frac{1}{2}(\mathbf{F}^T \cdot \mathbf{F} - \mathbf{I})$ is the Lagrangian strain. The second Piola-Kirchhoff stress can be expressed by the following general form, or in terms of the Lame constants, λ and μ,

$$\begin{aligned} \mathbf{S} &= \bar{\mathbf{C}} : \mathbf{E} \\ &= \lambda tr(\mathbf{E})\mathbf{I} + 2\mu\mathbf{E} \end{aligned} \tag{4.50}$$

The stress components are given by $S_{AB} = C_{ABCD}E_{CD}$. For small deformations, the material constants in a given hyperelastic constitutive equation must match those of the K-SV model at small strains (for more detail on this see Ciarlet [41]). We will use the K-SV material model as a template to match specific bio-strain energy functions at small strains. In other words, we will plot a deformation measure (e.g. axial stretch) versus the strain energy density reported in the literature and compare this to the simplest K-SV model to identify if the models match at very low (i.e. under $\approx 2\%$) strains (our requirement).

4.4.2 Finite Strain (Hyperelasticity)

Deriving a Measure of Stress

A material is called hyperelastic if there exists a stored energy function, W, that is only a function of the mechanical deformation (independent of rigid body rotations) and where the stresses are defined by, $\mathbf{S} = 2\frac{\partial W}{\partial \mathbf{C}} = \frac{\partial W}{\partial \mathbf{E}}$ or $\mathbf{P} = \frac{\partial W}{\partial \mathbf{F}}$. These relations come from the first law of thermodynamics (i.e. conservation of energy) which states that for an adiabatic, isothermal, closed system, the work must be non-negative or exactly zero. Different definitions for a non-negative stored energy (in the undeformed configuration) function follow from the Clausius-Plank inequality, i.e.,

$$\begin{aligned}
\underbrace{\int_{t_o}^{t_1}\Big(\int_{\omega_o}\dot{W}d\omega_o\Big)dt}_{WORK} &= \int_{t_o}^{t_1}\Big(\int_{\omega_o}\dot{F}_{iA}P_{Ai}d\omega_o\Big)dt \\
&= \frac{1}{2}\int_{t_o}^{t_1}\Big(\int_{\omega_o}\dot{C}_{AB}S_{BA}d\omega_o\Big)dt \\
&= \int_{t_o}^{t_1}\Big(\int_{\omega_o}\dot{E}_{AB}S_{BA}d\omega_o\Big)dt \geq 0. \qquad (4.51)
\end{aligned}$$

The integrals are arbitrary so we have $\dot{W} = \dot{F}_{iA}P_{Ai}$, $2\dot{W} = \dot{C}_{AB}S_{BA}$ and $\dot{W} = \dot{E}_{AB}S_{BA}$.

Fundamental Requirements for Finite-Strain Constitutive Equations

In addition to being invariant under rigid body rotations, every stored energy function must obey the following criteria:

1. $W \geq 0$ (as previously stated)
2. $\mathbf{C} = \mathbf{F}^T\mathbf{F} = \mathbf{I} \Leftrightarrow W = 0$ (zero deformation corresponds to the strain energy being identically zero)
3. $\mathbf{C} = \mathbf{I} \Rightarrow \mathbf{S} = \mathbf{0}$
4. The parameters in a finite deformation constitutive equation must be such that they match hyperelastic responses with known material constants (for example in the isotropic case, the Lame constants $\lambda(= \kappa - \frac{2\mu}{3})$ and μ, where

κ and μ are the bulk and shear modulus, respectively, when the material is perturbed around the undeformed configuration).

Note that the first three conditions for an admissible strain energy function are satisfied by construction.

Defining Isotropic and Anisotropic Hyperelastic Materials

By way of a brief introduction to the isotropy or anisotropy of hyperelastic materials, we will follow the main points of the development given in the text by Holzapfel [42], Section 6.2, and refer the reader there for a more complete development.

We seek to restrict the strain energy function to describing only the class of materials that behave *isotropically* (i.e. with the same material response, or stress-strain behavior, in every direction). As such, since the strain energy function is itself a function of the deformation of the body (e.g. through the right Cauchy tensor, $\mathbf{C}$ or the Green-Lagrange strain $\mathbf{E}$, hence the deformation gradient $\mathbf{F}$, as $\mathbf{C} = \mathbf{F}^T\mathbf{F}$ and $\mathbf{E} = \frac{1}{2}(\mathbf{C} - \mathbf{I})$), we must develop a requirement based on $\mathbf{F}$. Therefore, consider an arbitrary point with position vector $\mathbf{X}$ of an elastic continuum body in the reference configuration Ω_o at some initial time, $t = 0$. Then consider a rigid body motion (i.e. the body is translated by a vector, $\mathbf{c}$ and rotated by an orthogonal tensor, $\mathbf{Q}$) superimposed on the reference configuration such that we move to a new position given by the position vector $\mathbf{X}^* = \mathbf{c} + \mathbf{Q}\mathbf{X}$, where $\mathbf{X}^* \in \Omega_o^*$ (our new configuration). We now demand that a different motion $\mathbf{x} = \chi^*(\mathbf{X}^*, t)$ moves Ω_o^* to the current configuration, Ω so that $\mathbf{x} = \chi(\mathbf{X}, t) = \chi^*(\mathbf{X}^*, t)$; mapping $\mathbf{X}^*$ to the position described by $\mathbf{x}$.

By the chain rule, the deformation gradient $\mathbf{F}$ may be written as the following,

$$\mathbf{F} = \frac{\partial \mathbf{x}}{\partial \mathbf{X}} = \frac{\partial \mathbf{x}}{\partial \mathbf{X}^*}\frac{\partial \mathbf{X}^*}{\partial \mathbf{X}} = \frac{\partial \mathbf{x}}{\partial \mathbf{X}^*}\mathbf{Q} = \mathbf{F}^*\mathbf{Q}, \tag{4.52}$$

where, $\mathbf{F}^* = \frac{\partial \mathbf{x}}{\partial \mathbf{X}^*}$ is defined as the deformation gradient relative to the region Ω_o^*. We can rearrange (4.52 - (4)) to get $\mathbf{F}^* = \mathbf{F}\mathbf{Q}^T$. Therefore, we say that a hyperelastic material is *isotropic* relative to the reference configuration Ω_o if the values of the strain energy $W(\mathbf{F})$ and $W(\mathbf{F}^*)$ are the same for all orthogonal tensors $\mathbf{Q}$. Hence, we may write,

$$W(\mathbf{F}) = W(\mathbf{F}^*) = W(\mathbf{F}\mathbf{Q}^T). \tag{4.53}$$

In other words, a superposed rigid body motion should lead to the same value of the strain energy function at time, t. Conversely, if a superposed rigid body motion *does* change the value of the strain energy function at time t in the sense that

$W(\mathbf{F}) \neq W(\mathbf{F}^*)$, the material is said to be *anisotropic*. For a more general discussion of this the reader is referred to the text by Ogden [37].

4.5 A Survey of Constitutive Equations for Biological Tissues

Soft tissues are primarily composed of water and have negligible permeability (see Chuong and Fung [24]). Chuong and Fung investigated the incompressibility of the healthy arterial wall and found that it behaves as a nearly incompressible material in the range of stresses experienced *in vivo* (Chuong and Fung [7]). Stergiopulos et al. ([43]) showed that the medial layer of a pig aorta has similar mechanical properties through the wall thickness as well as an even matrix of smooth muscle cells. For these reasons, we will model the arterial tissue as an elastic, homogeneous medium that undergoes finite deformations (i.e. is hyperelastic). Although arteries exhibit viscoelastic characteristics (creep, stress relaxation and slight hysteresis), the assumption of hyperelasticity is sufficient in most physiologic and pathophysiologic cases. The assumption of hyperelasticity for arterial tissue has been shown by many researchers (Fung [31]; Patel and Fry [44]; Vito and Hickey [33]; Chuong and Fung [7]; Vorp et al. [34]; Raghavan and Vorp [45]). For the present research, both layers (media and adventitia) of the arterial wall are herein assumed to be incompressible, homogeneous, hyperelastic material undergoing finite deformations. Speirs et al. [46] report the performance of two anisotropic strain-energy functions formulated by Zulliger et al. [47] and Holzapfel et al. [48] in the framework of a finite element model. Both material models are a function of the collagen fiber angles in the arterial tissue and the reader is referred to those studies for additional detail. The most common strain energy functions are of exponential type (see Chuong and Fung [7]; Delfino et al. [5]) although polynomial forms (Vaishnav et al. [32]), logarithmic forms (Takamizawa and Hayashi [49]) and mixed forms (Holzapfel and Weizs*ä*cker [8]; Holzapfel, Gasser and Ogden [1]) are also popular.

The following sections outline these various material models from the simplest (K-SV) to the more complicated (Holzapfel). This last strain-energy function (Holzapfel) will be used in our finite element model to investigate the effects of simple pressure/axial stretch combinations with and without local regions of material variation (i.e. lesions where are material softer or stiffer than the surrounding regions).

4.5.1 On residual stresses in the load-free arterial segment

With regard to arterial wall mechanics, one of the most important contributions is that the load-free arterial ring is not stress-free; it opens when sliced along the axis of the vessel. It appears the first to publish this discovery were Vaishnav and Vossoughi [50]. Chuong and Fung [24] showed this to be important in computing transmural (radially normal to the tissue wall) stresses and quantify this effect by assuming a reference (load-free) configuration as an open sector (also stress-free) with a defined opening angle. Numerous studies have included residual stresses in their mathematical formulation of the arterial wall (e.g. Masson et al. [51], Holzapfel et al. [1]). In general, however, even the open-sector is *not* stress free as each distinct arterial layer (i.e. intima-media and adventitia) has a unique opening angle (see Vossoughi et al. [52], Greenwald et al. [53], and more theoretical work by Taber and Humphrey [54]). A study by Holzapfel et al. [48] shows the influence of residual stress in the arterial wall on the stress and strain distributions through the deformed wall thickness in the physiological (i.e. *in vivo*) state. They report a considerable difference between the presence and absence of residual stresses on the principal Cauchy stress components (σ_{rr}, $\sigma_{\theta\theta}$, σ_{zz}; radial, circumferential and longitudinal, respectively) through the deformed wall thickness. Interestingly, they contend that the circumferential and longitudinal Cauchy stresses (i.e. $\sigma_{\theta\theta}$, σ_{zz}, respectively) are substantially reduced (by almost 50%) in the medial layer in the presence of residual stresses in the arterial wall (i.e. Figure 4 of Holzapfel et al. [48]).

We will *not* include residual stresses in our mechanical description of the vessel wall for the following reasons: (1) it is not clear these added circumferential (i.e. axisymmetric) residual stresses will affect the relative behavior or stress and strain fields between healthy tissue and local irregularities in tissue material properties (though this remains an interesting topic of inquiry), (2) as mentioned above, the load-free configuration of an open sector is in fact not stress-free due to the different opening angles for each arterial wall layer and (3) for reasons of modeling simplicity.

4.5.2 On growth and remodeling of the arterial wall

The pulsetile (time-varying) blood flow through an arbitrary arterial segment induces both a pressure-driven circumferential stress and a fluid-flow related shear stress at a material point in the arterial wall. The pressure-induced wall stress is commonly characterized by the mean circumferential stress, $\sigma_{\theta\theta} = \frac{Pr}{t}$ (P is the internal pressure, r is the deformed inner radius and t is the deformed wall thickness) (from Laplace) and assuming the blood to be a Newtonian fluid, the mean shear stress at the inner surface is characterized by $\tau = \frac{4\eta Q}{\pi r^3}$ (η is the blood viscosity and Q

is the mean blood flow rate). It is generally accepted that endothelial cells, smooth muscle cells and fibroblasts in the intimal layer of the arterial wall are regulated in part by these stresses. Pathological changes such as hypertension (chronic increase in blood pressure), atherosclerosis (narrowing of the arterial lumen) and aneurysms (focal wall dilations) can lead to changes in the pressure and/or blood flow and hence, the mechanical environment of the arterial wall tissue. If these changes are sustained, the arterial wall will adapt by changing its structure or composition. Added mass from these changes is called growth, whereas a decrease in tissue mass is termed atrophy. Similarly, any irreversible change in the structure or material properties of the tissue is referred to as remodeling. Remodeling is the product of either reorganizing existing tissue constituents, or synthesizing new constituents. For example, in hypertension, the wall thickness increases in order to maintain or restore circumferential stresses that are uniform within each layer (Matsumoto and Hyashi [55]). For simplicity, growth and remodeling contributions to the arterial wall stress and strain fields are not considered in this study *although* the presence of local lesions on the inside of the arterial wall may lead to irregularities (under stretch and pressure) that can be assumed to change the blood flow at the arterial wall and hence, the growth and remodeling of the intima and media layers.

4.5.3 Isotropic Hyperelastic Material Laws

The following are two isotropic hyperelastic material laws used in the literature to study the overall stress-strain behavior of arterial walls under large deformations. As arterial walls are considered highly *anisotropic* due to the presence of collagen fibers (see [1]), these models lack the histological information possibly necessary for a more accurate description of a given stress-strain state. Nevertheless, they are commonly used and can provide simple comparisons to more complicated, hence error-prone, (anisotropic) material models.

The Mooney-Rivlin Model for Rubber-Like Materials

Possibly the most generic and commonly used isotropic, hyperelastic strain energy function for materials undergoing large deformations (e.g. rubber or biological tissues) is the compressible Mooney-Rivlin model. Though this model represents a necessary departure into modeling finite deformations, it lacks the strong stiffening effect of arteries in the large strain domain and the important anisotropy exhibited by the arterial wall (see Fung [31]). In other words, the strain energy function is only a polynomial function of the deformation invariants, I_1, I_2 and I_3. Hence, we present it only as a comparison to more phenomenological exponential and logarithmic-type strain energy functions for biological tissues found in literature.

The Mooney-Rivlin potential employs a convenient decomposition of incompressible and compressible constituents in order to facilitate easier numerical implementation (i.e. we don't have an indeterminate Lagrange multiplier we must solve for as part of an incompressibility constraint). The general form is as follows,

$$W = K_1(\bar{I}_1 - 3) + K_2(\bar{I}_2 - 3) + \frac{\kappa}{2}(\sqrt{I_3} - 1)^2. \tag{4.54}$$

Where, I_1, I_2 and I_3 are the three scalar invariants of $\mathbf{C}$ defined as,

$$\begin{aligned} I_1 &= tr(\mathbf{C}) \\ I_2 &= \frac{1}{2}\Big[(tr(\mathbf{C}))^2 - tr((\mathbf{C})^2)\Big] \\ I_3 &= det(\mathbf{C}) \end{aligned} \tag{4.55}$$

In this model, the first and second invariants of $\mathbf{C} = \mathbf{F}^T \cdot \mathbf{F}$ (I_1 and I_2) have been scaled by a power of the third invariant to ensure that they contribute nothing to the compressible part of the material response. Formally,

$$\begin{aligned} \bar{I}_1 &= I_1 I_3^{-1/3} = I_1 J^{-2/3} \\ \bar{I}_2 &= I_2 I_3^{-2/3} = I_2 J^{-4/3} \end{aligned} \tag{4.56}$$

where, $J = det(\mathbf{F})$. We can also define an incompressible deformation gradient, $\overline{\mathbf{F}} \equiv J^{1/3}\mathbf{F}$ and the associated Cauchy-Green strain tensor, $\overline{\mathbf{C}} = \overline{\mathbf{F}}^T \cdot \overline{\mathbf{F}} = J^{-2/3}\mathbf{C}$. The second Piola-Kirchhoff stress is then,

$$\begin{aligned} \mathbf{S} &= 2\Big(\frac{\partial W}{\partial I_1}\frac{\partial I_1}{\partial \mathbf{C}} + \frac{\partial W}{\partial I_2}\frac{\partial I_2}{\partial \mathbf{C}} + \frac{\partial W}{\partial I_3}\frac{\partial I_3}{\partial \mathbf{C}}\Big) \\ &= 2\Big(\frac{\partial W}{\partial \bar{I}_1}\frac{\partial \bar{I}_1}{\partial I_1}\mathbf{I} + \frac{\partial W}{\partial \bar{I}_2}\frac{\partial \bar{I}_2}{\partial I_2}\Big(I_1\mathbf{I} - \mathbf{C}\Big) + \frac{\partial W}{\partial I_3}I_3\mathbf{C}^{-1}\Big) \end{aligned} \tag{4.57}$$

where, the following derivatives of the principal invariants with respect to the Cauchy-Green strain tensor, $\mathbf{C}$, have been substituted,

$$\begin{aligned}\frac{\partial I_1}{\partial \mathbf{C}} &= \mathbf{I}\\ \frac{\partial I_2}{\partial \mathbf{C}} &= I_1\mathbf{I} - \mathbf{C}\\ \frac{\partial I_3}{\partial \mathbf{C}} &= I_3\mathbf{C}^{-1}\end{aligned} \tag{4.58}$$

The derivatives of the scaled with respect to the principle invariants are the following,

$$\begin{aligned}\frac{\partial \bar{I}_1}{\partial I_1} &= I_3^{-1/3}\\ \frac{\partial \bar{I}_2}{\partial I_2} &= I_3^{-2/3}\end{aligned} \tag{4.59}$$

The reader is referred to Ciarlet ([41]) for proofs of these derivatives. There is a very specific relationship between the material constants, K_1 and K_2 in the above model of $\mu = 2(K_1 + K_2)$, were μ is the shear modulus of the material. It should be noted that when $K_1 = \mu/2$ and $K_2 = 0$, the material is called a compressible Neo-Hookean material. The suitability of the Neo-Hookean material law (i.e. $W = \frac{\mu}{2}(I_1 - 3)$) to model elastin in the arterial wall (assuming the elastin behaves like a rubber-like material) has a sound theoretical basis (Treloar [8]). It is a generalization of Hooke's law (small strains) to the case of finite strains (Rivlin [9]).

A Phenomenological Material Model by Delfino et al. [5]

A potential for rubber-like (isotropic) materials was proposed by Delfino et al. [5] for carotid arteries which is able to model the typical stiffening effects in the high pressure domain. The strain energy has the form,

$$W = \frac{a}{b}\Big(exp\Big[\frac{b}{2}(\bar{I}_1 - 3)\Big] - 1\Big), \tag{4.60}$$

where $a > 0$ is a stress-like material parameter and $b > 0$ is a non-dimensional parameter. The first invariant of the modified right Cauchy-Green tensor $\bar{\mathbf{C}}$ is defined as $\bar{I}_1 = \bar{\mathbf{C}} : \mathbf{I}$. The material parameters for a human carotid artery, as reported in [5], are the following,

It is worth noting that the potential (4.60) increases monotonically with $\bar{I}_1$ and therefore guarantees strict local convexity (i.e. that the second derivative of W with respect to $\mathbf{E}$ is positive definite). This fundamental physical requirement in

Elastic Constants	
a =	44.2 kPa
b =	16.7 [-]

Table 4.4: Elastic constants of healthy human common carotid (HCC) artery for model by Delfino et al. [5]

hyperelasticity ensures that undesirable material instabilities are precluded. For 2D contour plots (that show this convexity) of (4.60) and other convex potentials used to model arteries, the reader is referred to Holzapfel et al. [1].

4.5.4 Anisotropic Hyperelastic Material Laws

A Choi-Vito-Type 2D Phenomenological Material Model by Vande Geest et al. [6]

In 2006, Vande Geest et al. [6] performed biaxial tests on a series of non-diseased human aortic samples and the highly nonlinear responses were described well by a 2D phenomenological Choi-Vito strain energy function, namely,

$$W = c\Big(exp[c_1 E_{\theta\theta}^2] + exp[c_2 E_{zz}^2] + exp[2c_3 E_{\theta\theta} E_{zz}] - 3\Big), \tag{4.61}$$

where, E_{AB} are principal values of Green-Lagrange strain $\mathbf{E}$. Mean values of the material parameters are shown in table (4.5).

Elastic Constants	
c =	0.32 kPa
c_1 =	70.6 kPa
c_2 =	71.7 kPa
c_3 =	64.0 kPa

Table 4.5: Elastic constants of healthy human artery for Choi-Vito-Type 2D model by Vande Geest et al. [6]

The second Piola-Kirchhoff stress is again found by taking the derivative with respect to the Green-Lagrange strain; $\mathbf{S} = \frac{\partial W}{\partial \mathbf{E}}$. It is worth noting that the material response is similar in the longitudinal and circumferential directions of healthy arterial tissue (see Humphrey et al. [56]). Vande Geest et al. also concluded this and state that aneurysmal degeneration of the abdominal aorta is associated with an increase in mechanical anisotropy, with preferential stiffening in the circumferential direction. Hence, the values of the material constants reported here are really only applicable for modeling healthy aortic tissue (which we assume in this study).

The exponential material laws such as Choi-Vito (4.61) show a more aggressive increase in material stiffness at higher strains than polynomial models such as Mooney-Rivlin (4.54). Due to the fact that arteries also exhibit this behavior (i.e. from the contribution of the collagen fibers in the adventitia layer, mainly), these exponential-type constitutive laws are perhaps more suited for investigations on the supraphysiological distention and inflation of the arterial wall.

Fig. (4.6) shows the behavior of a typical polynomial-type hyperelastic material law (Mooney-Rivlin) and an exponential law (Choi-Vito) from an applied triaxial stretch. Fig. (4.7) compares the K-SV material law for *infinitesimal* deformations to a hyperelastic model (Choi-Vito) in order to show the narrow range of strain in which a typical small-strain material law matches a hyperelastic one.

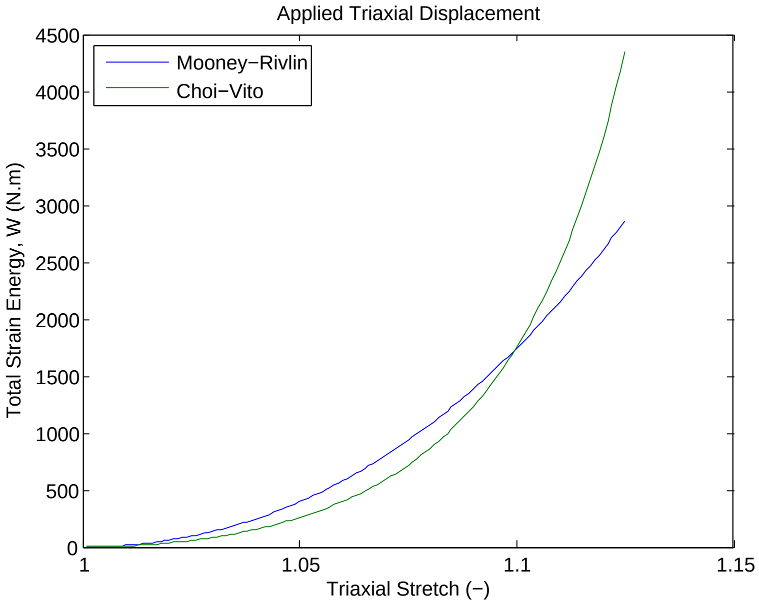

Figure 4.6: Strain energy responses of typical polynomial and exponential-type material models for arterial tissue

A Fung-Type 3D Phenomenological Material Model by Chuong and Fung [7]

The most concise two-dimensional potential used in literature to describe the non-linear stress-strain behavior of arterial wall tissue is the exponential potential proposed by Fung et al. [57]. A generalization to three-dimensions was proposed by Chuong and Fung [7], which assumes the principal directions of the stress tensor coincide with the radial, circumferential and axial directions of the artery. Deng et al. [58] proposed an extension of the classical two-dimension function given in

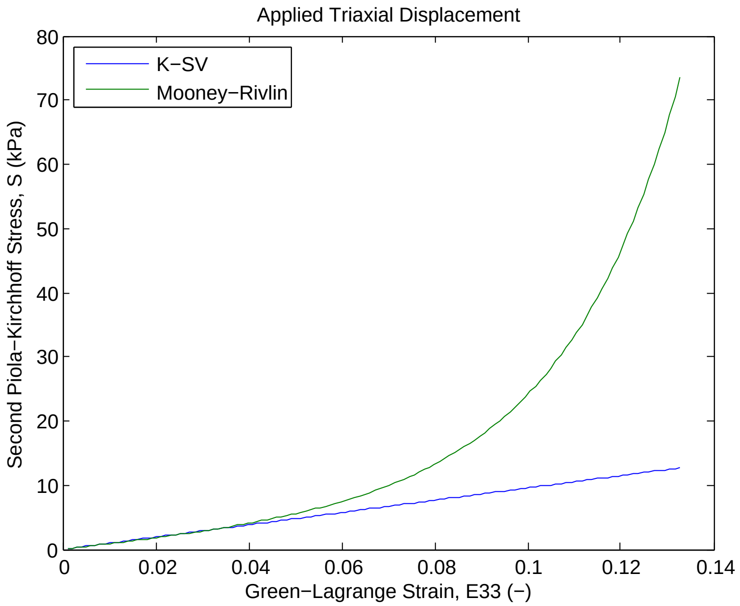

Figure 4.7: Hyper versus infinitesimal elasticity; what is ”large” strain?

[57] to include shear deformations in the z = constant plane; hence, incorporating torsional effects.

There have been many subsequent modifications to these functions that have been published. The most general three-dimensional strain energy function of *Fung's* type is formulated by Humphrey [3] and has the form,

$$W = \frac{c}{2}\Big(exp[Q] - 1\Big) \tag{4.62}$$

where c is a material parameter and Q denotes a quadratic function of the components of the Green-Lagrange strain tensor,

$$Q = b_1E_{\theta\theta}^2 + b_2E_{zz}^2 + b_3E_{rr}^2 + 2b_4E_{\theta\theta}E_{zz} + 2b_5E_{zz}E_{rr} + 2b_6E_{\theta\theta}E_{rr} + 2b_7E_{\theta z}^2 + 2b_8E_{rz}^2 + 2b_9E_{\theta r}^2 \tag{4.63}$$

where, $b_1, ..., b_9$ are non-dimensional material parameters characterizing the blood vessel and E_{IJ}, where $I, J = r, \theta, z$ are the Green-Lagrange strain components. According to Holzapfel, Gasser and Ogden [1], there is no *a priori* restriction on the material parameters presented in Chuong and Fung [7]. They go on to mention that it is important to note that in order for the anisotropic function W to be polyconvex in the sense of Ball [59], the material parameters $b_1, ..., b_9$ must not be chosen arbitrarily.

Holzapfel et al. [1] go on to show both a convex set of material constants (for a rabbit carotid artery) and an alternative set that leads to non-convexity. The convex values are summarized below (note that we list only $b_1, ..., b_7$ as experiment 71 in [7] only includes shear effects from torsion; or, $E_{\theta z}$) .

Elastic Constants
c = 26.95 kPa
b_1 = 0.9925 [-]
b_2 = 0.4180 [-]
b_3 = 0.0089 [-]
b_4 = 0.0749 [-]
b_5 = 0.0295 [-]
b_6 = 0.0193 [-]
b_7 = 5.0000 [-]

Table 4.6: Elastic constants of healthy rabbit carotid artery for 3D Fung-type model by Chuong et al. [7]

The second Piola-Kirchhoff stress is again found by taking the derivative with respect to the Green-Lagrange strain; $\mathbf{S} = \frac{\partial W}{\partial \mathbf{E}}$.

A 3D Two-Layer Fiber-Reinforced Material Model by Holzapfel et al. [1]

So far in this section we have presented only material models that, although anisotropic, represent a homogeneous continuum and do not include any of the histological features of the arterial wall. Holzapfel et al. [8] proposes modeling each (thick-walled) layer as a composite reinforced by two families of fibers that are arranged in symmetric spirals. They assume that each layer (i.e. the media and adventitia) respond with similar mechanical characteristics and therefore use the same strain energy function although with different material constants. We will adopt this material model, although we will *not* impose an incompressibility constraint on the material due to the inherent numerical complications involved in implementing it within the finite element method. For simplicity, we will also neglect residual strains in the material and consider the reference configuration of the artery to be stress-free.

Following [1], we suggest using an additive split of the strain energy function, W, into W_{iso}, associated with purely *isotropic* deformations and W_{aniso}, associated only with *anisotropic* deformations. At low pressures, the energy contribution of the wavy collagen fibers within each layer of the arterial wall is assumed to be negligible and the mechanical response is mainly governed by the noncollagenous matrix material (i.e. elastin), which we assume to be isotropic and modeled by W_{iso}. According to Roach et al. [60], the resistance to stretching at large deformations (e.g. pressures) is almost entirely due to collagenous fibers and this response is therefore governed entirely by the anisotropic function W_{aniso}. Information about the orientation of the collagen fibers, which render the material orthotropic, is incorporated. Hence, the two-term potential is the following,

$$W(\mathbf{C}, \mathbf{M}^{(1)}, \mathbf{M}^{(2)}) = W_{iso}(\mathbf{C}) + W_{aniso}(\mathbf{C}, \mathbf{M}^{(1)}, \mathbf{M}^{(2)}) \tag{4.64}$$

The three-dimensional, statistical distribution of the collagen fibers are modeled as two major families of symmetrically-arranged fibers having mean directions represented by the unit vectors $\mathbf{M}^{(1)}$ and $\mathbf{M}^{(2)}$ which specify preferred directions in the reference configuration of the material. It is these directions that render the material layers anisotropic. We can express the strain energy functions in terms of the principal invariants and we assume the following form,

$$W(I_1, I_4, I_6) = W_{iso}(I_1) + W_{aniso}(I_4, I_6) \tag{4.65}$$

The isotropic invariant is defined as $I_1 = trace(\mathbf{C}) = C_{11} + C_{22} + C_{33}$. The anisotropic invariants I_4 and I_6 employ structural tensors $\mathbf{A}^{(1)}$ and $\mathbf{A}^{(2)}$ that are defined by the dyadic product of the unit vectors $\mathbf{M}^{(1)}$ and $\mathbf{M}^{(2)}$ as $\mathbf{A}^{(1)} = \mathbf{M}^{(1)} \otimes \mathbf{M}^{(1)}$ and $\mathbf{A}^{(2)} = \mathbf{M}^{(2)} \otimes \mathbf{M}^{(2)}$. These invariants have clear physical interpretations as the squares of the stretches in the directions of the associated families of collagen fibers. They are defined as,

$$\begin{aligned} I_4 &= \mathbf{C} : \mathbf{A}^{(1)} = \mathbf{C} : (\mathbf{M}^{(1)} \otimes \mathbf{M}^{(1)}) = \mathbf{M}^{(1)} \cdot \mathbf{C}\mathbf{M}^{(1)} && (4.66) \\ I_6 &= \mathbf{C} : \mathbf{A}^{(2)} = \mathbf{C} : (\mathbf{M}^{(2)} \otimes \mathbf{M}^{(2)}) = \mathbf{M}^{(2)} \cdot \mathbf{C}\mathbf{M}^{(2)} && (4.67) \end{aligned}$$

For simplicity, we will use a Neo-Hookean material for $W_{iso}(I_1)$ to model the isotropic hyperelastic matrix material and for $W_{aniso}(I_4, I_6)$ we use an exponential function to model the highly nonlinear response to large deformations from the families of collagen fibers. In addition, we assume that the responses of the two families of fibers to be uncoupled. Therefore, the general strain energies are the following,

$$\begin{aligned} W_{iso}(I_1) &= \frac{c}{2}(I_1 - 3) && (4.68) \\ W_{aniso}(I_4, I_6) &= \frac{k_1}{2k_2} \sum_{\alpha=4,6} \left(exp\left[k_2 (I_\alpha - 1)^2 \right] - 1 \right) && (4.69) \end{aligned}$$

If we apply this model to each layer separately, we have six material constants; that is, c_M, k_{1M} and k_{2M} for the media and c_A, k_{1A} and k_{2A} for the adventitia. In respect of equation (4.68), our strain energy functions for each layer are explicitly,

$$R_{in} < R < (R_{in} + H_M), \begin{cases} W_{iso}(I_1)_M = \frac{c_M}{2}(I_1 - 3) \\ W_{aniso}(I_4, I_6)_M = \frac{k_{1M}}{2k_{2M}} \sum_{\alpha=4,6} \Big(exp\Big[k_{2M}(I_{\alpha M} - 1)^2 \Big] - 1 \Big) \end{cases} \tag{4.70}$$

$$(R_{in} + H_M) < R < R_{out}, \begin{cases} W_{iso}(I_1)_A = \frac{c_A}{2}(I_1 - 3) \\ W_{aniso}(I_4, I_6)_A = \frac{k_{1A}}{2k_{2A}} \sum_{\alpha=4,6} \Big(exp\Big[k_{2A}(I_{\alpha A} - 1)^2 \Big] - 1 \Big) \end{cases} \tag{4.71}$$

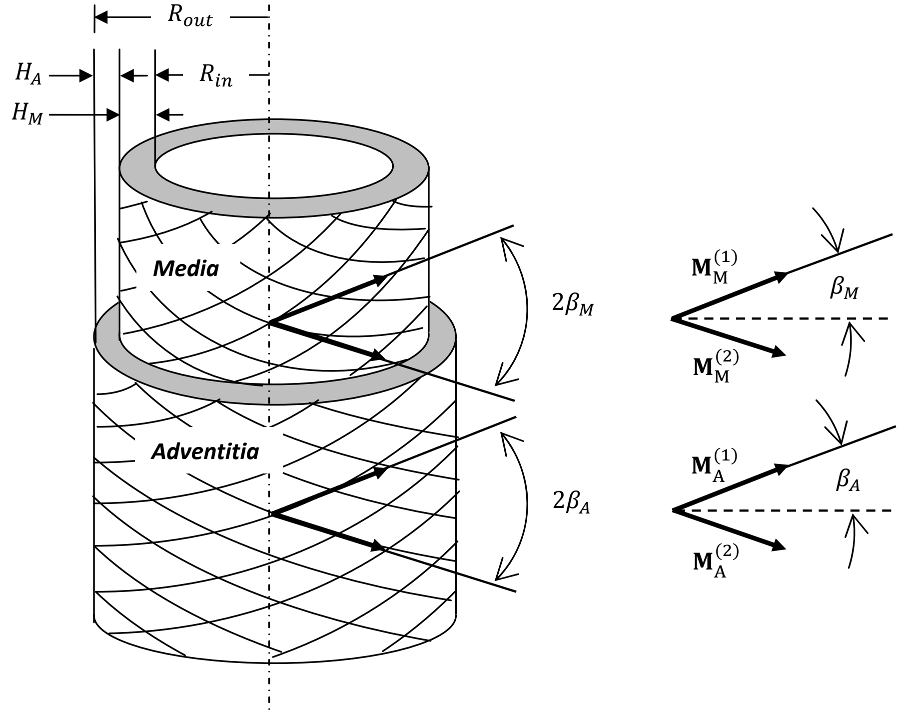

Figure 4.8: An artery as a fiber-reinforced composite: two layers of helically arranged symmetric fibers in each layer

We specify our anisotropic invariants for each layer as $I_{4j} = \mathbf{C} : \mathbf{A}_j^{(1)} = \mathbf{M}_j^{(1)} \cdot \mathbf{C}\mathbf{M}_j^{(1)}$ and $I_{6j} = \mathbf{C} : \mathbf{A}_j^{(2)} = \mathbf{M}_j^{(2)} \cdot \mathbf{C}\mathbf{M}_j^{(2)}$ where, $j = M, A$. We use material and geometrical data for a carotid artery from a rabbit from experiment 71 in Fung et al. [57], which is summarized in table (4.7).

The constitutive equation for the second Piola-Kirchhoff stress $\mathbf{S}$ follows from the strain energy given in (4.65) by differentiation with respect to $\mathbf{C}$. In using the

Elastic Constants	
Media	Adventitia
$c_M = 3.0000\ kPa$	$c_A = 0.3000\ kPa$
$k_{1M} = 2.3632\ kPa$	$k_{1A} = 0.5620\ kPa$
$k_{2M} = 0.8393\ [-]$	$k_{2A} = 0.7112\ [-]$
$H_M = 0.26\ mm$	$H_A = 0.13\ mm$
$\beta_M = 29.0^o$	$\beta_A = 62.0^o$

Table 4.7: Elastic constants of healthy rabbit carotid artery for 3D Fung-type model applied to a fiber-reinforced, two-layer cylinder by Holzapfel et al. [8]

chain rule, **S** is given as a function of the three scalar invariants (in this case we are using only three of them; for a more general formula for the **S** in terms of the other invariants see [42], section 6.8) in the form,

$$\mathbf{S} = 2\frac{\partial W(\mathbf{C}, \mathbf{A}^{(1)}, \mathbf{A}^{(2)})}{\partial \mathbf{C}} = 2\sum_{\alpha} \frac{\partial W(I_1, I_4, I_6)}{\partial I_\alpha} \frac{\partial I_\alpha}{\partial \mathbf{C}}; \quad \alpha = 1, 4, 6. \tag{4.72}$$

The partial derivatives of the invariants with respect to **C** are given explicitly as the following,

$$\frac{\partial I_1}{\partial \mathbf{C}} = \frac{tr\mathbf{C}}{\partial \mathbf{C}} = \frac{\partial(\mathbf{I} : \mathbf{C})}{\partial \mathbf{C}} = \mathbf{I} \ \ or \ \ \frac{\partial I_1}{\partial C_{AB}} = \delta_{AB} \tag{4.73}$$

$$\frac{\partial I_4}{\partial \mathbf{C}} = \mathbf{A}^{(1)} = \mathbf{M}^{(1)} \otimes \mathbf{M}^{(1)} \ \ or \ \ \frac{\partial I_4}{\partial C_{AB}} = M_A^{(1)} M_B^{(1)} \tag{4.74}$$

$$\frac{\partial I_6}{\partial \mathbf{C}} = \mathbf{A}^{(2)} = \mathbf{M}^{(2)} \otimes \mathbf{M}^{(2)} \ \ or \ \ \frac{\partial I_6}{\partial C_{AB}} = M_A^{(2)} M_B^{(2)} \tag{4.75}$$

Therefore, the explicit relation for the stress may be written,

$$\mathbf{S} = 2\left[\frac{\partial W}{\partial I_1}\mathbf{I} + \frac{\partial W}{\partial I_4}\mathbf{M}^{(1)} \otimes \mathbf{M}^{(1)} + \frac{\partial W}{\partial I_6}\mathbf{M}^{(2)} \otimes \mathbf{M}^{(2)}\right]. \tag{4.76}$$

It should be noted that the potential shown in (4.68) is *incompressible* and therefore requires special finite element approaches to implement. In other words, there is a non-zero state of stress when there is zero deformation if we use merely the strain energies shown. If we are to add a penalty parameter (which we will do in the following section) to penalize the strain energy when the Jacobian deviates from unity, then we are imposing a quai-incompressibility constraint in our formulation and therefore do not need to devise special numerical methods.

A 3D Two-Layer Fiber-Reinforced Polyconvex Material Model by Balzani et. al [2]

In this section we will use a specific form of polyconvex, transversely-isotropic strain energy function for our arterial wall. The above model (4.68) by Holzapfel et. al [1] is limited in that (1) there exists a non-zero stress state at zero deformation, (2) it requires difficult numerical techniques to implement incompressibility (i.e. there is no incompressibility constraint on the isotropic-part of the strain energy itself) and (3) polyconvexity is not satisfied thereby allowing non-physical results. We therefore implement the model proposed by Balzani et. al [2] that guarantees the existence of energy minimizers of some variational principals for finite strains; in other words, is hyperelastic and polyconvex (for the proof of polyconvexity as it applies to the following strain energy function, see [2], Appendix A). They have determined the material constants of this model by matching the experimentally derived stress-stretch behavior of the medial layer of an excised human aortic artery (see [2] for more experimental details).

For a brief background, we follow the main points of Schr̈oder et. al [61] and refer the reader there for a more complete development of the concepts of polyconvexity as applies to finite-strain energy functions. As Schr̈oder points out, ″ the existence of energy minimizers of some variational principles for finite strains is based on the concept of *quasiconvextiy*, introduced by Morrey [62]″. They go on to suggest that the requirement for quasiconvexity is based on an integral-inequality that is difficult to manipulate and a more practical concept is that of *polyconvexity* which implies the acoustic tensor of a strain energy function is elliptic for all deformations. That is, we are guaranteed the existence of physical equilibrium states that sufficient conditions for the existence of minimums in the total energy of the body. For more on the general theory behind the construction of polyconvex, anisotropic strain energy functions, see Schröder [63] and Schröder and Neff [26].

Following [61], we begin by assuming the total strain energy is simply the sum of the anisotropic and isotropic strain energies,

$$W = W^{ISO} \ + \ W^{ANISO}. \tag{4.77}$$

We will impose a quasi-incompressibility constraint on the isotropic part of the strain energy function so as to avoid special finite element approaches. As before, we will use a Neo-Hookean material model for the isochoric part plus a term that penalizes any changes in the material volume. Our isotropic strain energy function is then the following,

$$W^{ISO} = \underbrace{c_1\left(I_1 I_3^{-1/3} - 3\right)}_{Neo-Hookean} + \underbrace{\epsilon\left(I_3^{\gamma} + I_3^{-\gamma} - 2\right)}_{\substack{quasi-incompressibility \\ constraint}} ; \quad c_1 > 0,\ \epsilon > 0,\ \gamma > 1 \tag{4.78}$$

Balzini uses a polynomial-type potential to represent the anisotropic portion of the material response. They go on to show that if certain conditions for the mixed invariants I_4 and I_6 are satisfied, the strain energy function is guaranteed to be *polyconvex*; thereby ensuring physical material responses distinct from possible erroneous numerical results. The requirements laid forth are the following,

$$W^{ANISO} = \begin{cases} \alpha_1(I_4-1)^{\alpha_2} + \alpha_1(I_6-1)^{\alpha_2}; & for \;\; I_4 \geq 1.0 \; and \; I_6 \geq 1.0, \\ \alpha_1(I_4-1)^{\alpha_2}; & for \;\; I_4 \geq 1.0 \; and \; I_6 < 1.0, \\ \alpha_1(I_6-1)^{\alpha_2}; & for \;\; I_4 < 1.0 \; and \; I_6 \geq 1.0, \\ 0; & for \;\; I_4 < 1.0 \; and \; I_6 < 1.0. \end{cases} \tag{4.79}$$

The invariants I_1 and I_3 are, as before, defined as $I_1 = tr(\mathbf{C})$ and $I_3 = det(\mathbf{C})$. Following Balzani et al. [2], we define the so-called mixed invariants I_4 and I_6 using equations (4.66). Note that c_1 scales the isotropic response and the parameters ϵ and γ control the volumetric deformation. The second term of (4.78) enforces quasi-incompressibility by penalizing any change in volume of the material. α_1 scales the anisotropic terms and α_2 controls the level of curvature (in stress-strain space) in the fiber directions (i.e. the level of non-linearity, or exponential-type behavior of the material).

The stresses from the isotropic and anisotropic parts are additive so we have the following general form,

$$\mathbf{S} = \mathbf{S}^{ISO} \; + \; \mathbf{S}^{ANISO} \tag{4.80}$$

Finding the stress from our strain energy function, we recall the following,

$$\mathbf{S} = 2\sum_{\alpha=1}^{8} \frac{\partial W(I_1, ..., I_8)}{\partial I_\alpha} \frac{\partial I_\alpha}{\partial \mathbf{C}} \tag{4.81}$$

Due to the particular invariants that the isotropic part W^{ISO} depends on (i.e. I_1 and I_3), the isotropic stress is then,

$$\mathbf{S}^{ISO} = 2\left(\frac{\partial W^{ISO}}{\partial I_1} \frac{\partial I_1}{\partial \mathbf{C}} + \frac{\partial W^{ISO}}{\partial I_3} \frac{\partial I_3}{\partial \mathbf{C}} \right) \tag{4.82}$$

$$or,$$

$$S^{ISO}_{AB} = 2\left(\frac{\partial W^{ISO}}{\partial I_1} \frac{\partial I_1}{\partial C_{AB}} + \frac{\partial W^{ISO}}{\partial I_3} \frac{\partial I_3}{\partial C_{AB}} \right)$$

$$\frac{\partial W^{ISO}}{\partial I_1} = c_1 I_3^{-1/3} \tag{4.83}$$

$$\frac{\partial W^{ISO}}{\partial I_3} = -\frac{1}{3}c_1 I_1 I_3^{-4/3} + \epsilon\gamma I_3^{-1}(I_3^{\gamma} - I_3^{-\gamma}) \tag{4.84}$$

$$\frac{\partial I_1}{\partial \mathbf{C}} = \mathbf{I} \quad or \quad \frac{\partial I_1}{\partial C_{AB}} = \delta_{AB} \tag{4.85}$$

$$\frac{\partial I_3}{\partial \mathbf{C}} = I_3\mathbf{C}^{-1} \quad or \quad \frac{\partial I_3}{\partial C_{AB}} = I_3 C_{AB}^{-1} \tag{4.86}$$

Substituting yields the following expression,

$$\begin{aligned} \mathbf{S}^{ISO} &= 2\Big[c_1 I_3^{-1/3}\mathbf{I} + \Big(\epsilon\gamma(I_3^{\gamma} - I_3^{-\gamma}) - \frac{1}{3}c_1 I_1 I_3^{-1/3}\Big)\mathbf{C}^{-1}\Big] \\ &or, \\ S_{AB}^{ISO} &= 2\Big[c_1 I_3^{-1/3}\delta_{AB} + \Big(\epsilon\gamma(I_3^{\gamma} - I_3^{-\gamma}) - \frac{1}{3}c_1 I_1 I_3^{-1/3}\Big)C_{AB}^{-1}\Big] \end{aligned} \tag{4.87}$$

From Table (4.1), we can represent the Cauchy stresses using the formula $\sigma = J^{-1}\mathbf{F}\cdot\mathbf{S}\cdot\mathbf{F}^T$. After simplification, we get the following,

$$\begin{aligned} \sigma^{ISO} &= \frac{2}{J}\Big[c_1 I_3^{-1/3}\mathbf{B} + \Big(\epsilon\gamma(I_3^{\gamma} - I_3^{-\gamma}) - \frac{1}{3}c_1 I_1 I_3^{-1/3}\Big)\mathbf{I}\Big] \\ &or, \\ \sigma_{ij}^{ISO} &= 2\Big[c_1 I_3^{-1/3}B_{ij} + \Big(\epsilon\gamma(I_3^{\gamma} - I_3^{-\gamma}) - \frac{1}{3}c_1 I_1 I_3^{-1/3}\Big)\delta_{ij}\Big] \end{aligned} \tag{4.88}$$

We will only explicitly show the stress for the first conditions of equation (4.79) as the other conditions are simplifications of these cases. The first condition of W^{ANISO} depends on I_4 and I_6, therefore the full expression for the stress is the following.

$$\begin{aligned} \mathbf{S}^{ANISO} &= 2\Big(\frac{\partial W^{ANISO}}{\partial I_4}\frac{\partial I_4}{\partial \mathbf{C}} + \frac{\partial W^{ANISO}}{\partial I_6}\frac{\partial I_6}{\partial \mathbf{C}}\Big) \\ &or, \\ S_{AB}^{ANISO} &= 2\Big(\frac{\partial W^{ANISO}}{\partial I_4}\frac{\partial I_4}{\partial C_{AB}} + \frac{\partial W^{ANISO}}{\partial I_6}\frac{\partial I_6}{\partial C_{AB}}\Big) \end{aligned} \tag{4.89}$$

$$\frac{\partial W^{ANISO}}{\partial I_4} = \alpha_1\alpha_2(I_4 - 1)^{\alpha_2 - 1} \tag{4.90}$$

$$\frac{\partial W^{ANISO}}{\partial I_6} = \alpha_1\alpha_2(I_6 - 1)^{\alpha_2 - 1} \tag{4.91}$$

$$\frac{\partial I_4}{\partial \mathbf{C}} = \mathbf{M}^{(1)} \otimes \mathbf{M}^{(1)} \quad or \quad \frac{\partial I_4}{\partial C_{AB}} = M_A^{(1)} M_B^{(1)} \tag{4.92}$$

$$\frac{\partial I_6}{\partial \mathbf{C}} = \mathbf{M}^{(2)} \otimes \mathbf{M}^{(2)} \quad or \quad \frac{\partial I_6}{\partial C_{AB}} = M_A^{(2)} M_B^{(2)} \tag{4.93}$$

Substituting yields the following expression,

$$\begin{aligned} \mathbf{S}^{ANISO} &= 2\alpha_1\alpha_2\Big[\Big((I_4-1)^{\alpha_2-1}\Big)\mathbf{M}^{(1)}\otimes\mathbf{M}^{(1)} + \Big((I_6-1)^{\alpha_2-1}\Big)\mathbf{M}^{(2)}\otimes\mathbf{M}^{(2)}\Big] \\ or, & \\ S_{AB}^{ANISO} &= 2\alpha_1\alpha_2\Big[\Big((I_4-1)^{\alpha_2-1}\Big)M_A^{(1)}M_B^{(1)} + \Big((I_6-1)^{\alpha_2-1}\Big)M_A^{(2)}M_B^{(2)}\Big] \end{aligned} \tag{4.94}$$

Defining $\mathbf{m} = \mathbf{FM}$, we get the following Cauchy stresses,

$$\begin{aligned} \sigma^{ANISO} &= \frac{2\alpha_1\alpha_2}{J}\Big[\Big((I_4-1)^{\alpha_2-1}\Big)\mathbf{m}^{(1)}\otimes\mathbf{m}^{(1)} + \Big((I_6-1)^{\alpha_2-1}\Big)\mathbf{m}^{(2)}\otimes\mathbf{m}^{(2)}\Big] \\ or, & \\ \sigma_{ij}^{ANISO} &= \frac{2\alpha_1\alpha_2}{J}\Big[\Big((I_4-1)^{\alpha_2-1}\Big)m_i^{(1)}m_j^{(1)} + \Big((I_6-1)^{\alpha_2-1}\Big)m_i^{(2)}m_j^{(2)}\Big] \end{aligned} \tag{4.95}$$

4.6 Results

In this section we present the overall response of our three-dimensional, nonlinear finite element model for various combinations of axial stretch, transmural pressure and presence (or absence) of material ”lesions” (locally stiffer or softer tissue) in the arterial wall. For all cases considered, we will use only the final polyconvex, transversely-isotropic hyperelastic strain energy function and associated material constants for a human arterial wall presented by Balzani et. al [2] and summarized above by equations (4.78) and (4.79). This model, as has been mentioned, captures the histology of the collagen fibers through certain structural tensors, easily implements our incompressibility constraint, is polyconvex and has been ”hand-fitted” (see [2]) to experimental data on human arterial (medial) tissue. Through it’s polyconvex construction, it avoids certain mathematical and computational deficiencies evident in many other phenomenological models. Table (4.8) lists the material constants used for the healthy medial tissue (per [2]). For the adventitia layer, we have scaled the isotropic constants to be 1/10 those for the medial layer which is consistent with what has been experimentally found by Holzapfel et. al [8].

Elastic Constants	
Media	Adventitia
$c_1 = 13.50\ kPa$	$c_1 = 1.35\ kPa$
$\epsilon = 10.00\ kPa$	$\epsilon = 1.00\ kPa$
$\gamma = 20.00\ [-]$	$\gamma = 20.00\ [-]$
$\alpha_1 = 10^{14}\ kPa$	$\alpha_1 = 10^{14}\ kPa$
$\alpha_1 = 20.0\ kPa$	$\alpha_1 = 20.0\ kPa$

Table 4.8: Material data for human aortic tissue from Balzani et. al [2].

4.6.1 Finite Element Model Geometry

We borrow from the paper by Holzapfel and Gasser ([64]) and use the arterial geometry listed for a healthy human Left Anterior Descending (LAD) coronary artery. Note that we are using the material data for aortic tissue, recall the human aorta is located in the midsection, roughly between the heart and waist), though the geometry is from the coronary artery (recall the LAD is located on the anterior side of the heart). In that study, the geometry listed is for the load-free *opened-up* configuration as they include residual stresses in their model. We will assume this geometry for our load-free *closed* configuration as we are not considering residual stresses in this study. Figure (4.9) shows a schematic of the size of the load-free configuration of the artery which will be used for all subsequent boundary and loading conditions performed. Note that the adventitia layer is approximately 33% of the total wall thickness. Further note that the arterial section length is arbitrarily chosen to be 10 mm (in general, there may be residual stresses in the axial direction as well but we do not consider these).

4.6.2 Case Studies

The main novelty of this study in inherent to the completely independent development of the three-dimensional, nonlinear finite element code. In other words, since we have constructed our numerical finite element from scratch, coding our own solvers and algorithms, the model is infinitely tunable to whatever conditions we choose to study. This is an advantage over studies that use commercial code in that there are a limited number of parameters under the user's control.

In light of this, it would be imprudent and inefficient to run a large number of parameter studies as the relevance of one study over another would be debatable. Rather, we will mimic the most common studies in literature (i.e. extension and inflation) with the most current anisotropic strain energy function (i.e. a polyconvex, invariant-based structural model for each layer) and report the stresses and strains under these conditions.

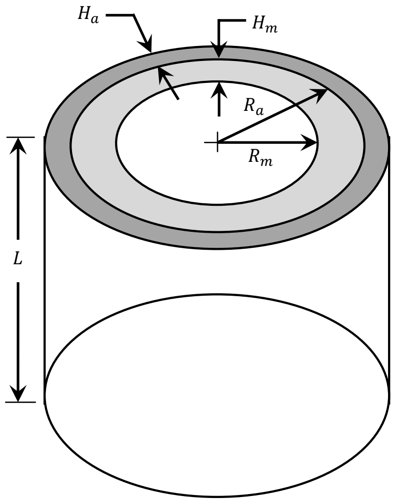

Geometric Parameters	
R_m =	3.302mm
R_a =	3.482mm
H_m =	0.493mm
H_a =	0.247mm
L =	10.0mm

Figure 4.9: Load-free configuration arterial geometry used in this study

On the Presence of Lesions in the Arterial Wall

To take advantage of the user-control of our model, we further look at the presence of lesions, or local material abnormalities, in the arterial wall under the same boundary and loading conditions as model of healthy tissue. To our knowledge, no studies have been performed that include all of these conditions simultaneously. Specifically, we will model two pathological conditions: (1) the scar-like tissue that results from a complete bisection and suturing of the artery - as modeled by a ring-like stiff region through both layers of the tissue wall and (2) a locally asymmetric stiff and soft spot-like region through both layers of the tissue. This could be interpreted as a degradation of the arterial wall (soft) or a calcification (stiff).

To achieve the desired axial stretch and transmural pressure, all degrees of freedom are held fixed for the elements at both ends (i.e. each end is considered ”glued” in-place) and one end is incrementally stretched along the axis of the artery and (depending on the case) the pressure is slowly incremented to a maximum value. The elastic constants governing the isotropic response of the adventitia layer (outer layer) is roughly *an order of magnitude* less than that of the medial layer (consistent with the literature). Note that Mesh 5 was used for all subsequent cases.

Case A. Medial and Adventitia Layers, 10% Axial Extension, No Transmural Pressure

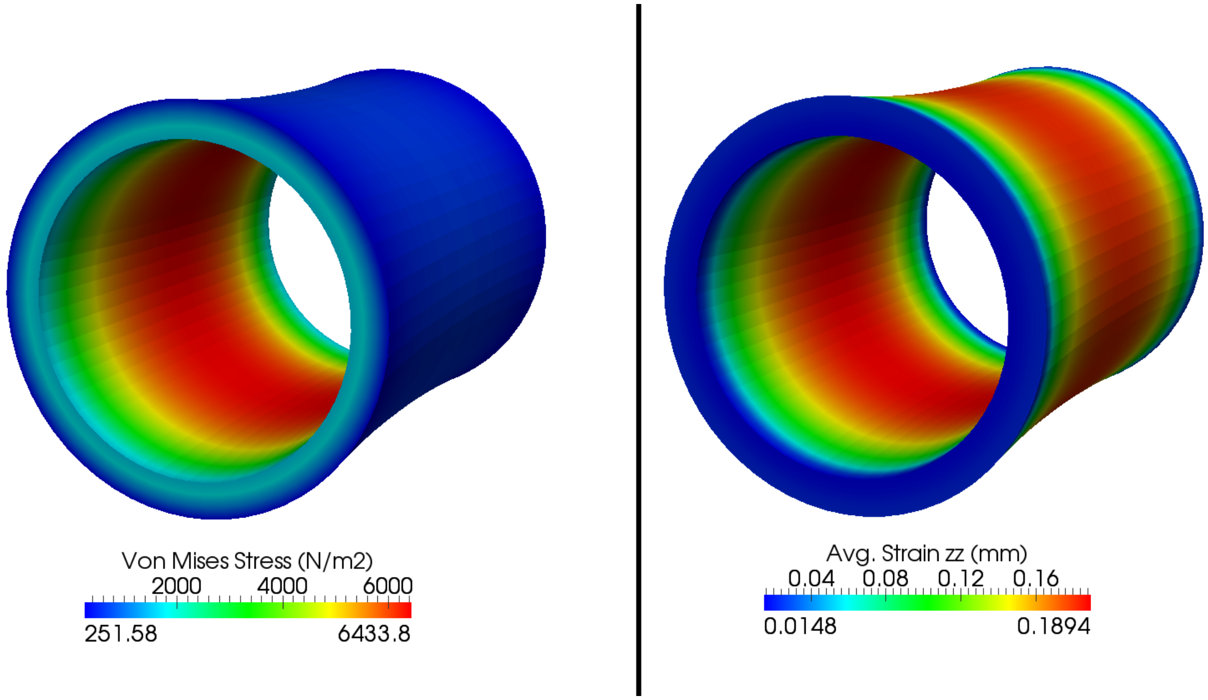

Figure 4.10: Case A: 10% Axial Extension, No Transmural Pressure

Fig.s (4.10 - 4.13) show the resulting principal (Cauchy) stresses (in $\frac{N}{m^2}$) from a physically realistic (*in vivo*) applied axial stretch of $\lambda = 1.1$ (i.e. 10%), with no transmural pressure. Note that the principal stresses are constant along the length of the artery in the adventitia layer and the medial layer shows a significant gradient. Fig. (4.10) shows the Von Mises stress (left) in Pascals and the average axial strain (mm).

Fig. (4.11) shows the through-thickness average radial stress contour of a section of the artery. Note that, as you would expect, the highest stresses occur near the ends of the vessel where the highest radial strains occur. The vessel exhibits a necking at the waist as you would expect under this mode of deformation. Fig. (4.12) shows that the circumferential stress is almost identical in magnitude and distribution to the radial stress. Fig. (4.13) shows the considerably higher longitudinal stress; the majority of which is carried in the stiffer, medial layer.

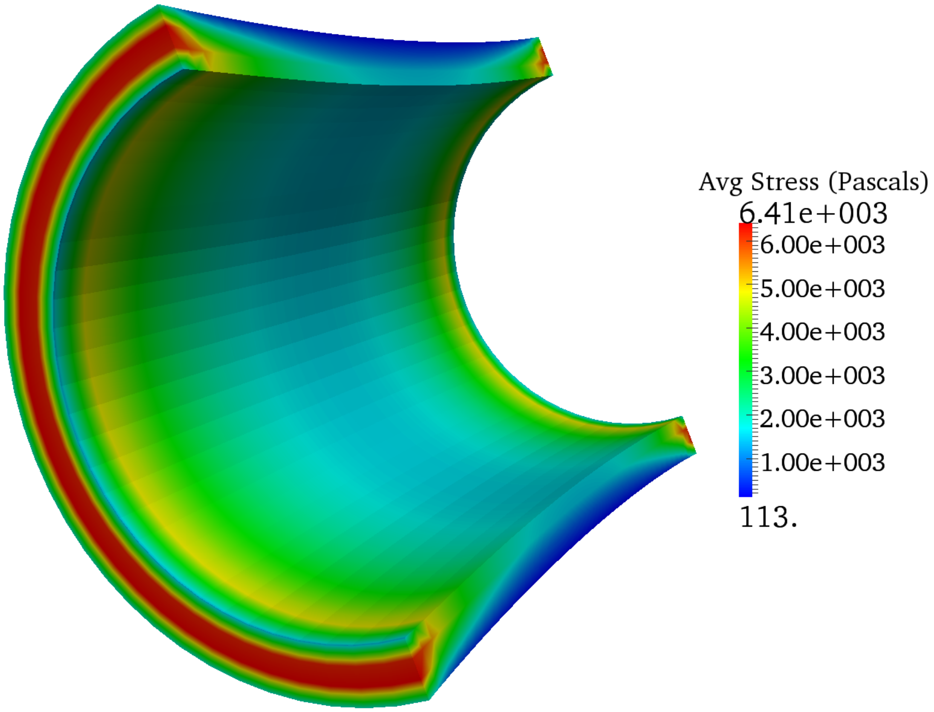

Figure 4.11: Case A: Average radial Cauchy stress, σ_{rr}

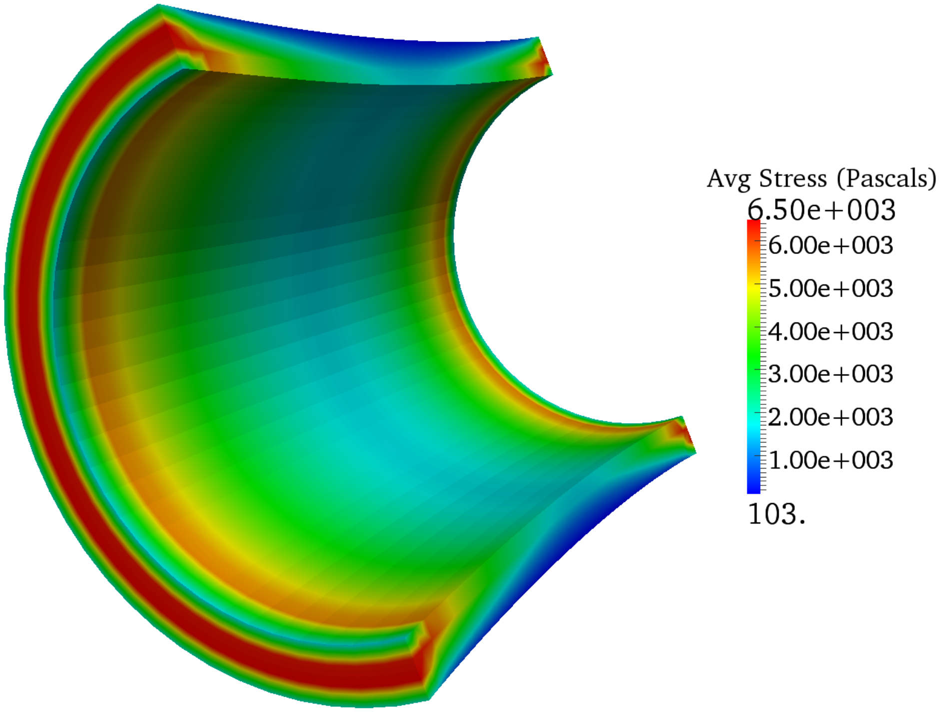

Figure 4.12: Case A: Average circumferential Cauchy stress, $\sigma_{\theta\theta}$

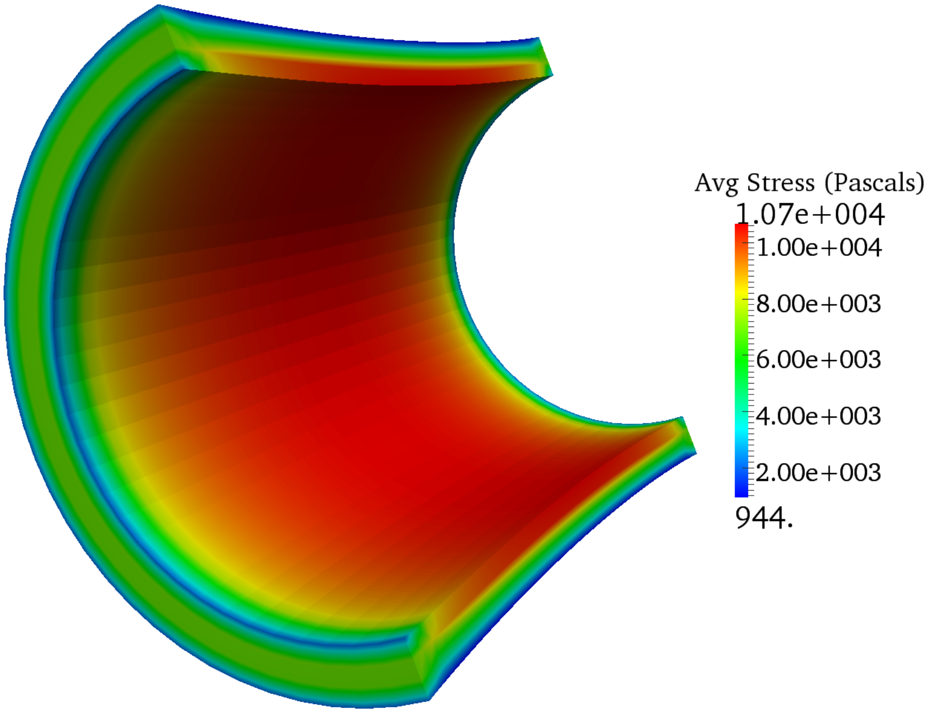

Figure 4.13: Case A: Average longitudinal Cauchy stress, σ_{zz}

Case B. Medial and Adventitia Layers, 10% Axial Extension, 20 kPa Transmural Pressure

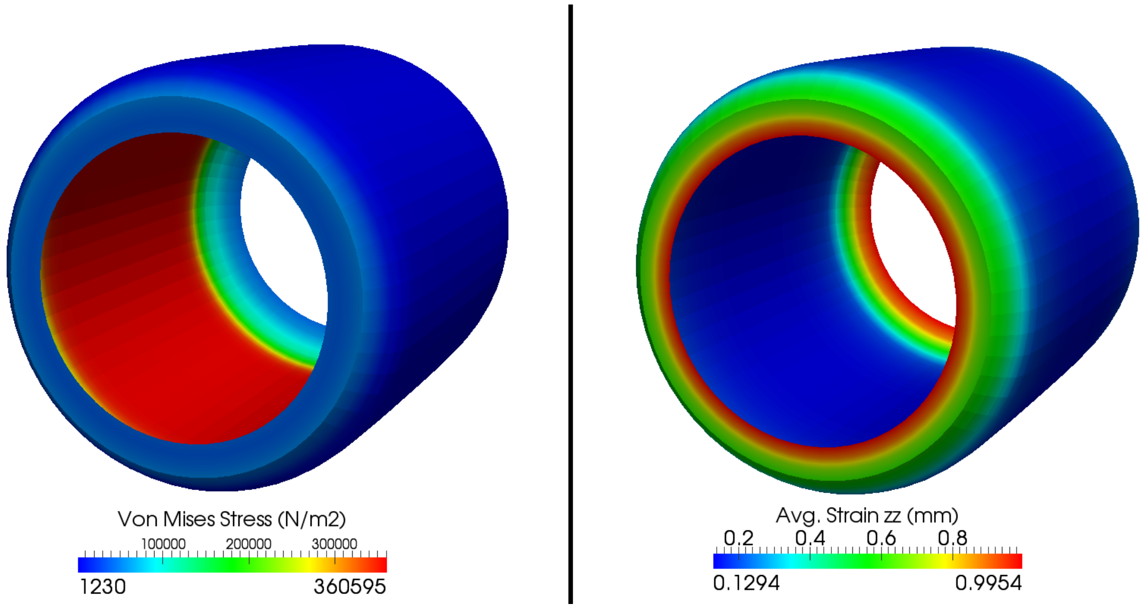

Figure 4.14: Case B: 10% Axial Extension, 20 kPa Transmural Pressure

Fig.s (4.14 - 4.17) show the resulting principal (Cauchy) stresses (in $\frac{N}{m^2}$) from a physically realistic (*in vivo*) applied axial stretch of $\lambda = 1.1$ (i.e. 10%) and transmural pressure of 20 kPa. Again, the principal stresses are constant along the length of the artery in the adventitia layer and the medial layer shows a significant gradient.

Fig. (4.15) shows how the radial distension of the vessel acts to even out the stress distribution between the two layers. Compare this to the through-thickness stress gradient shown in Figure (4.11). Now the circumferential stress, however, is predictably more and the gradient better defined (Fig. (4.16)).

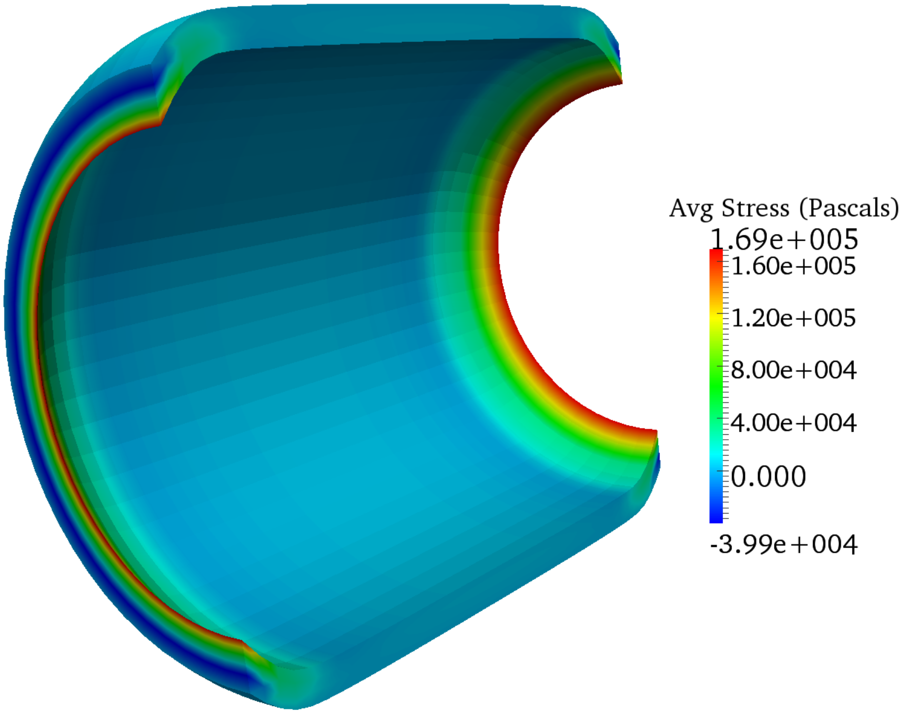

Figure 4.15: Case B: Average radial Cauchy stress, σ_{rr}

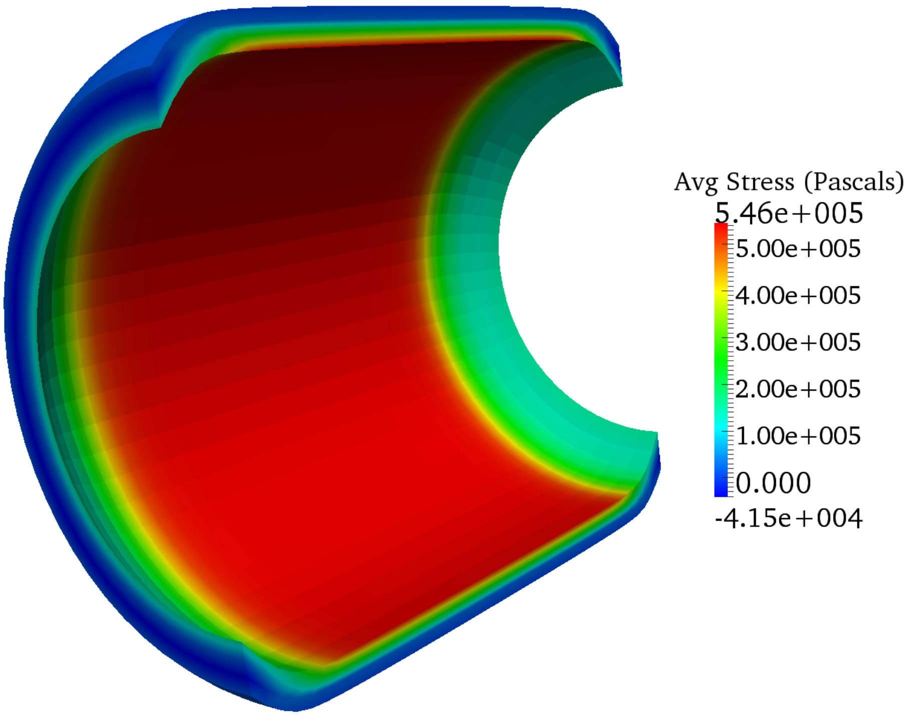

Figure 4.16: Case B: Average circumferential Cauchy stress, $\sigma_{\theta\theta}$

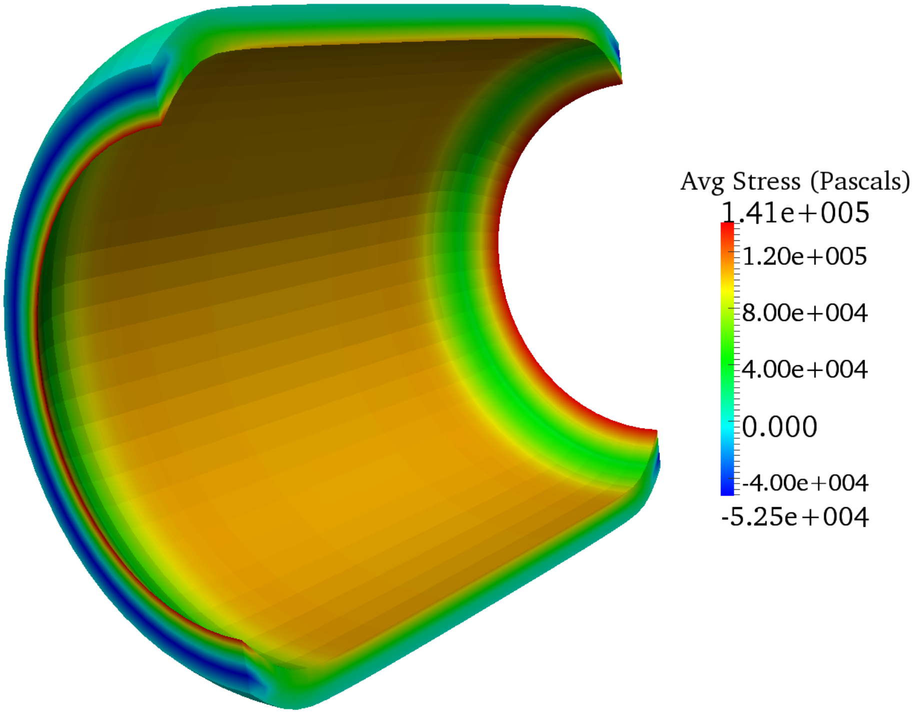

Figure 4.17: Case B: Average longitudinal Cauchy stress, σ_{zz}

Case C. Medial and Adventitia Layers, 10% Axial Extension, 20 kPa Transmural Pressure, Stiff Ring Lesion

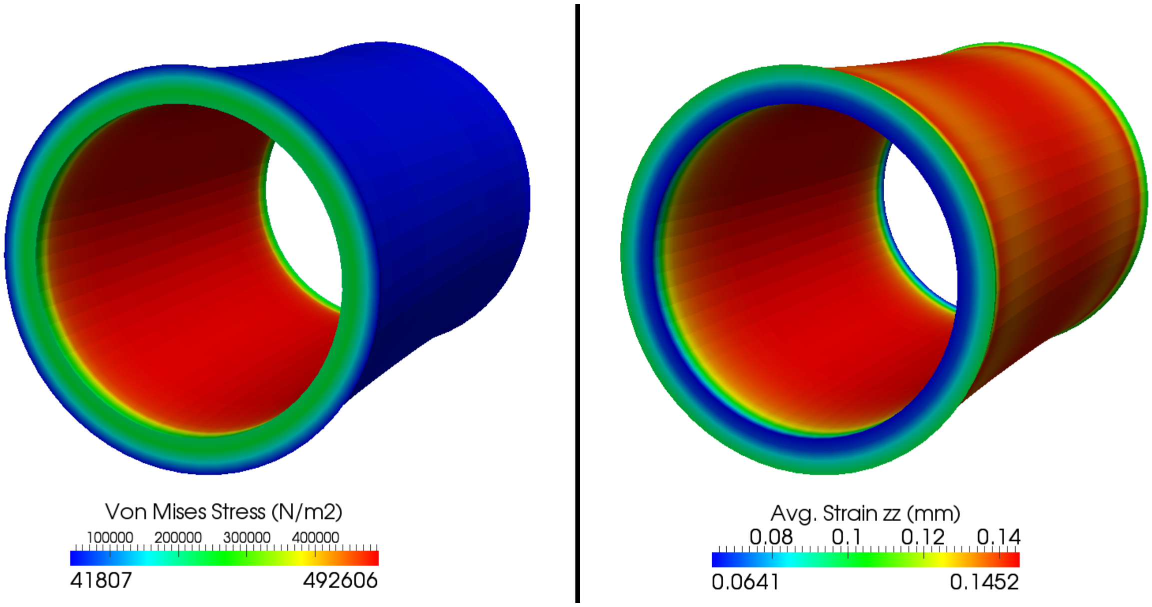

Figure 4.18: 10% Axial Extension, 20 kPa Transmural Pressure, 100X Stiff Ring Lesion

Fig.s (4.18 - 4.21) show the resulting principal (Cauchy) stresses (in $\frac{N}{m^2}$) from a physically realistic (*in vivo*) applied axial stretch of $\lambda = 1.1$ (i.e. 10%) and transmural pressure of 20 kPa and a narrow (about 2% of the overall segment length) stiff (100x) ring lesion at mid span. The elastic constants in the material description of the lesion are two orders of magnitude stiffer, for both layers, than the surrounding tissue.

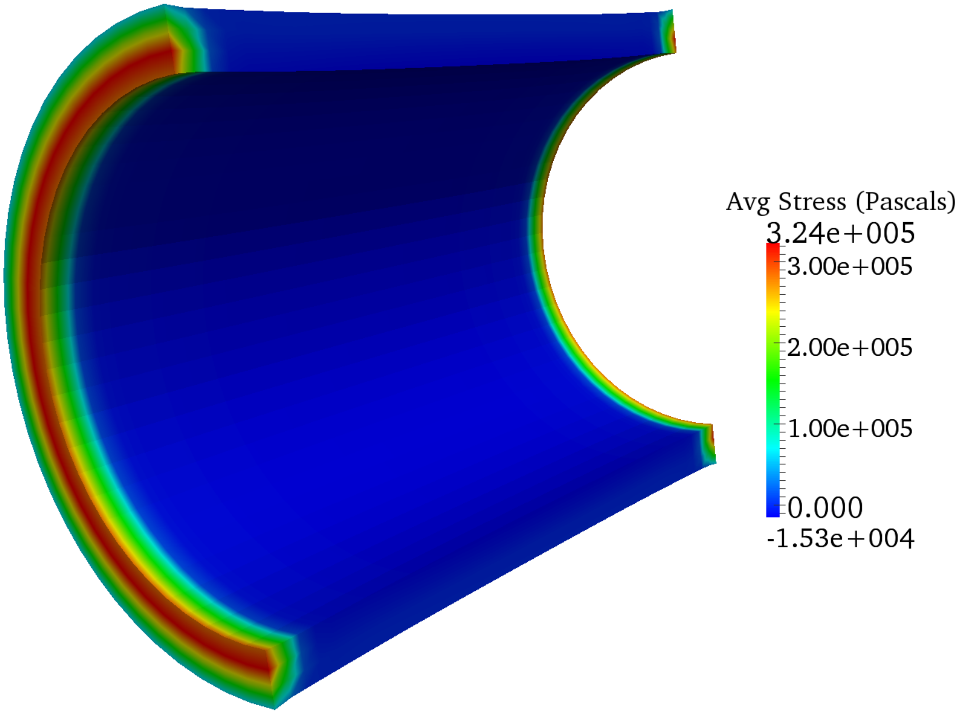

Figure 4.19: Case C: Average radial Cauchy stress, σ_{rr}

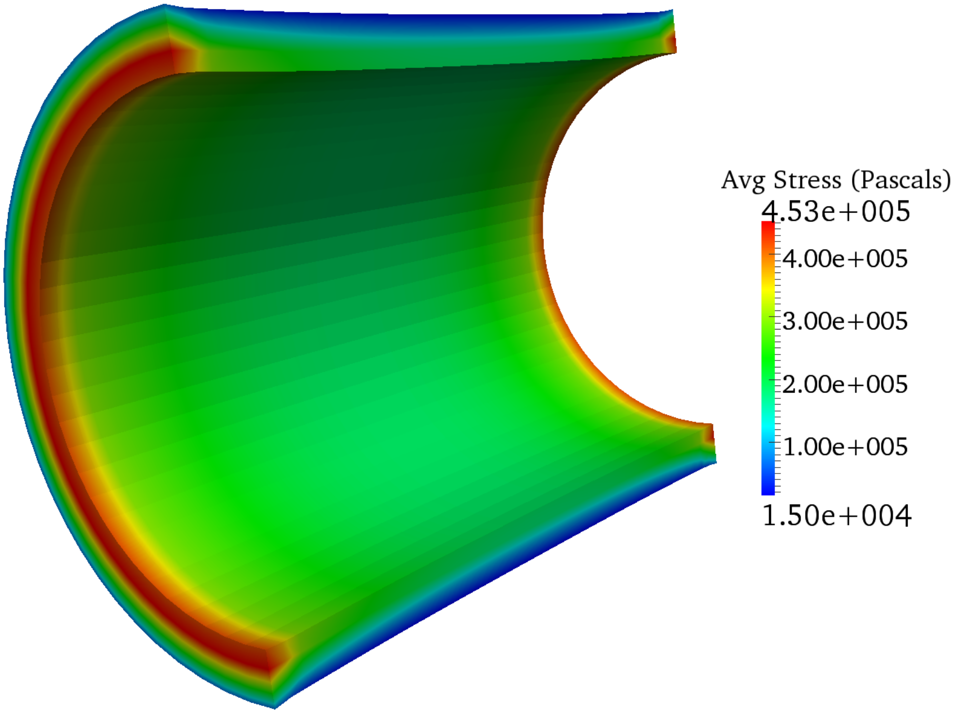

Figure 4.20: Case C: Average circumferential Cauchy stress, $\sigma_{\theta\theta}$

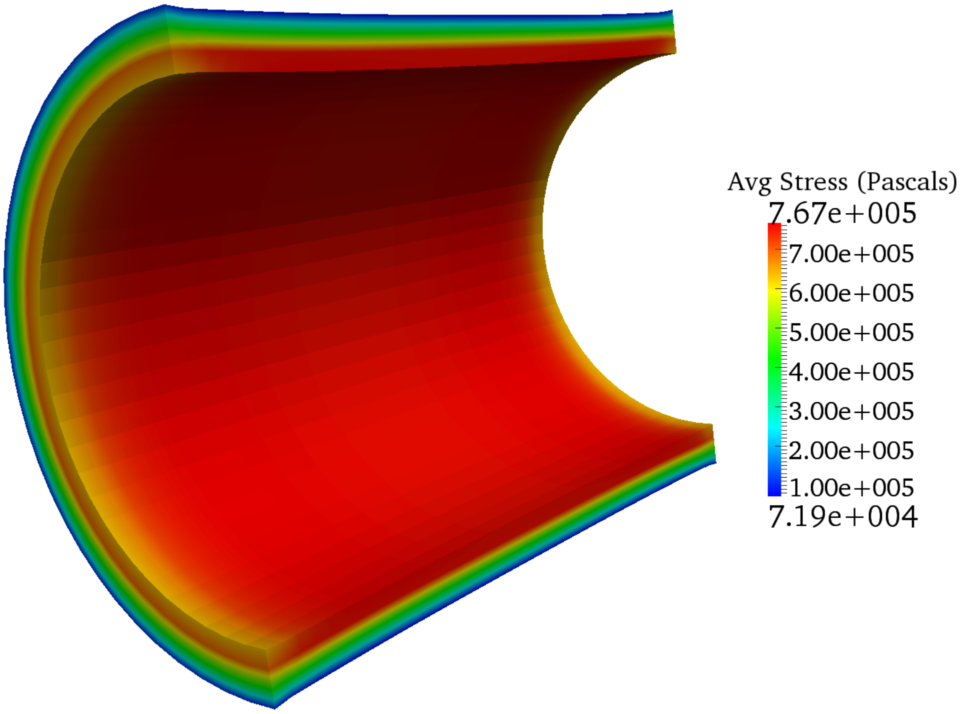

Figure 4.21: Case C: Average longitudinal Cauchy stress, σ_{zz}

Case D. Medial and Adventitia Layers, 10% Axial Extension, 20 kPa Transmural Pressure, Stiff Spot Lesion

The spot-like lesion is defined as a set of three elements in each principal direction. The lesion is three orders of magnitude stiffer (1000x) in elastic response to the surrounding tissue. Fig.s (4.23 - 4.25) show a sequence of Von Mises stress at selected times of the deformation described in Case D, leading to the final state shown in here in Fig. (4.22). The artery has been sectioned to show the stress distribution on the inner surface of the medial layer as well as the through thickness distribution. Note the stiff material spot-like lesion primarily affects the stress field on the inner medial layer, although the lesion does goes through both layers. Fig. (4.26) shows a section view of the principal stresses at the final time (3.92 sec).

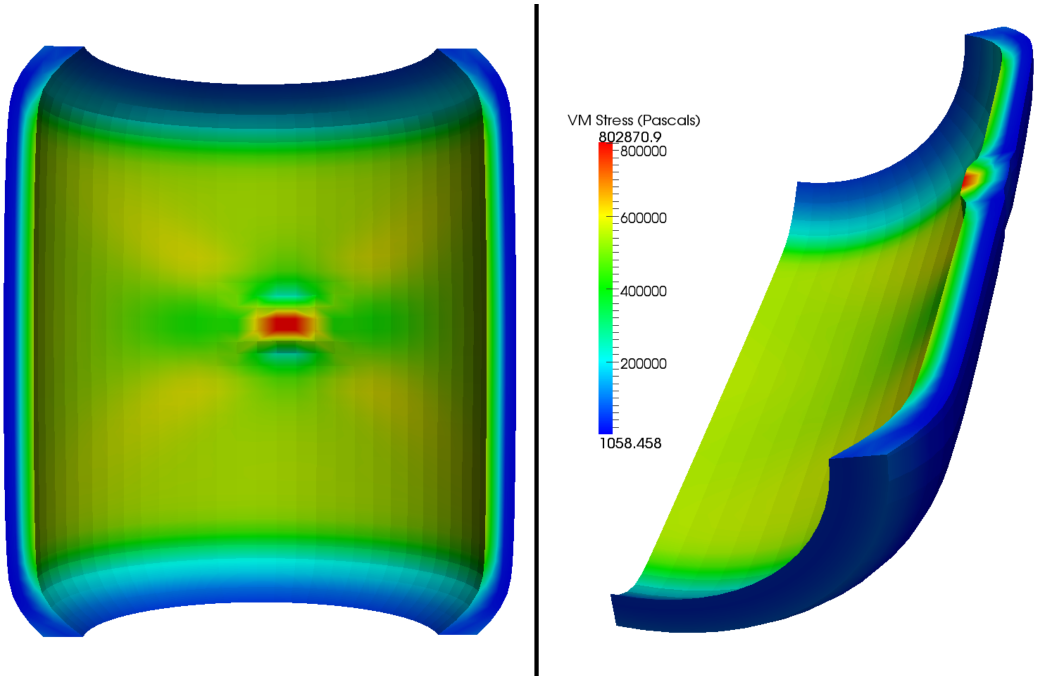

Figure 4.22: Case D: Average Von Mises stress, σ_{vm}, at time = 3.92s

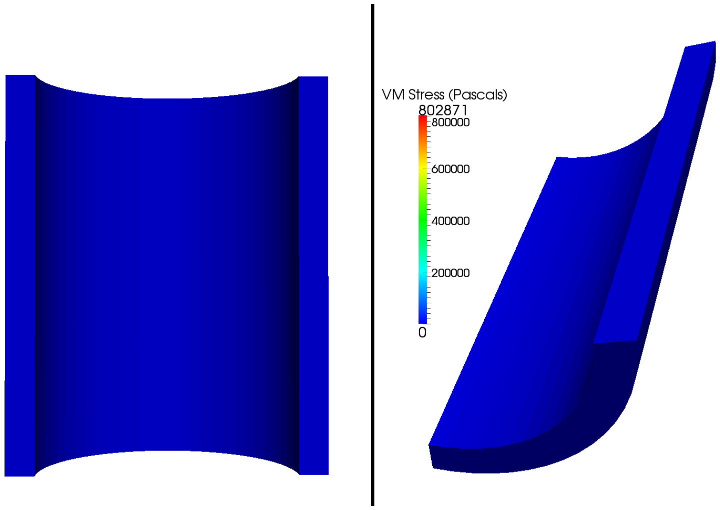

(a) t=0.0s

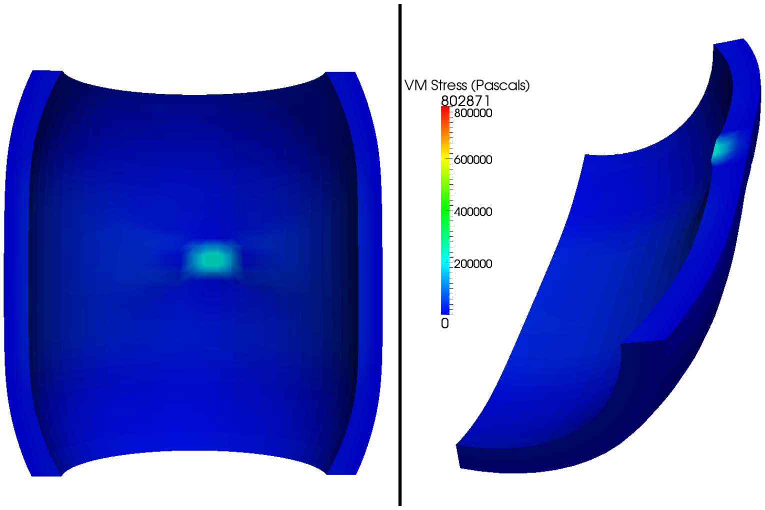

(b) t=0.4s

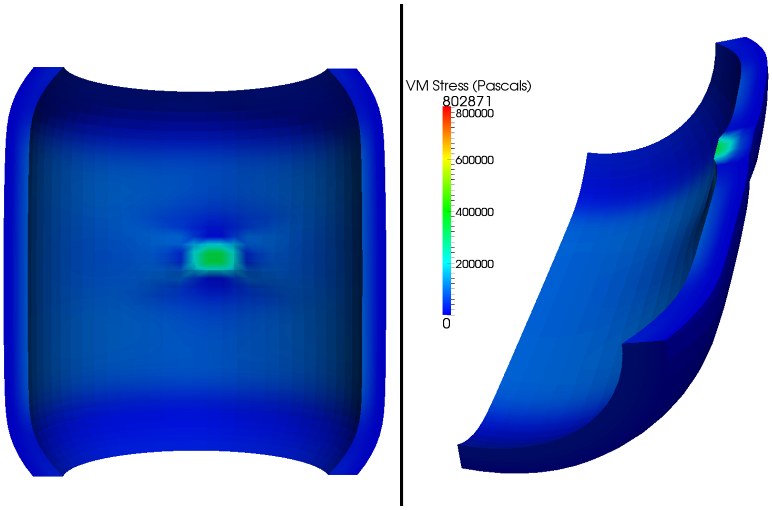

(c) t=0.8s

Figure 4.23: Spot-lesion inflation sequence - times (0.0s-0.8s)

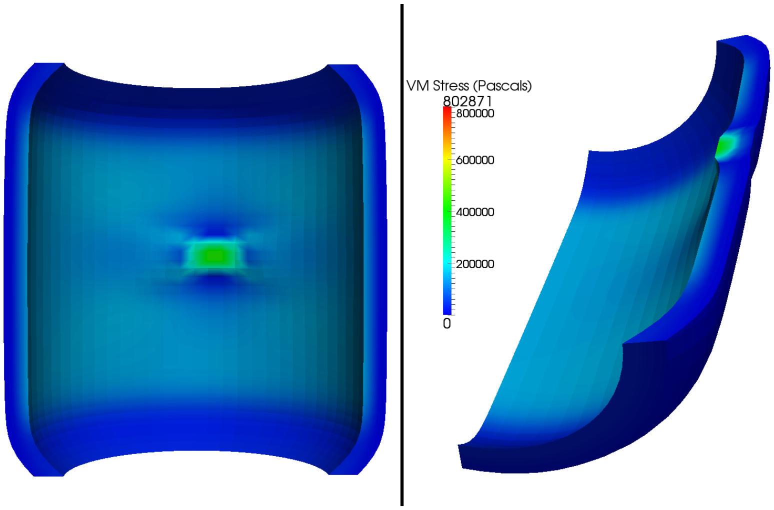

(a) t=1.2s

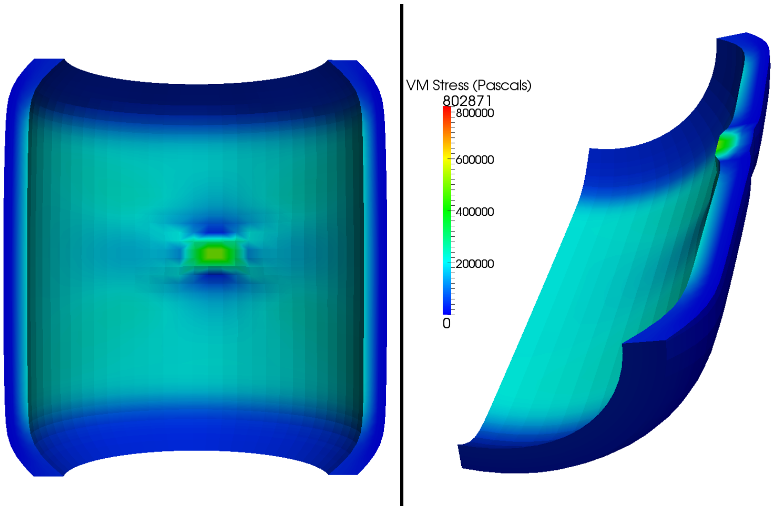

(b) t=1.6s

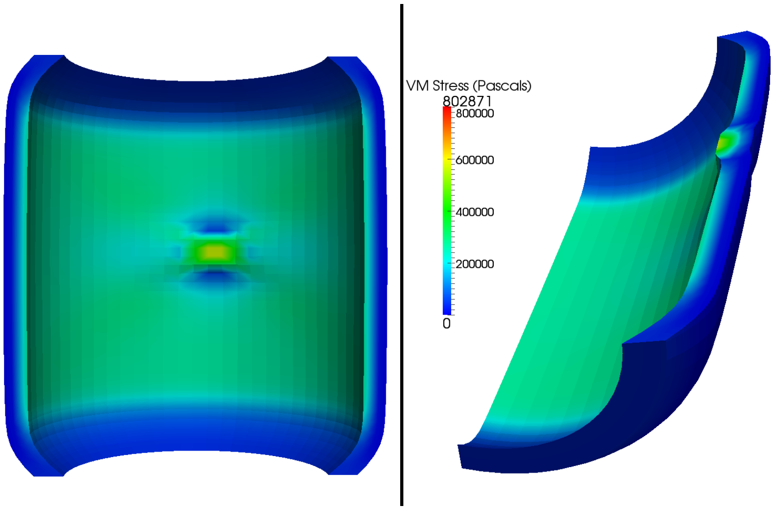

(c) t=2.0s

Figure 4.24: Spot-lesion inflation sequence - times (1.2s-2.0s)

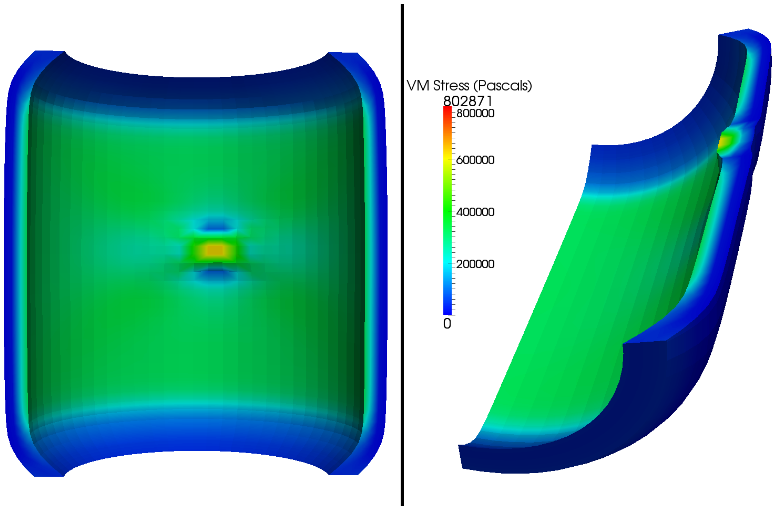

(a) t=2.4s

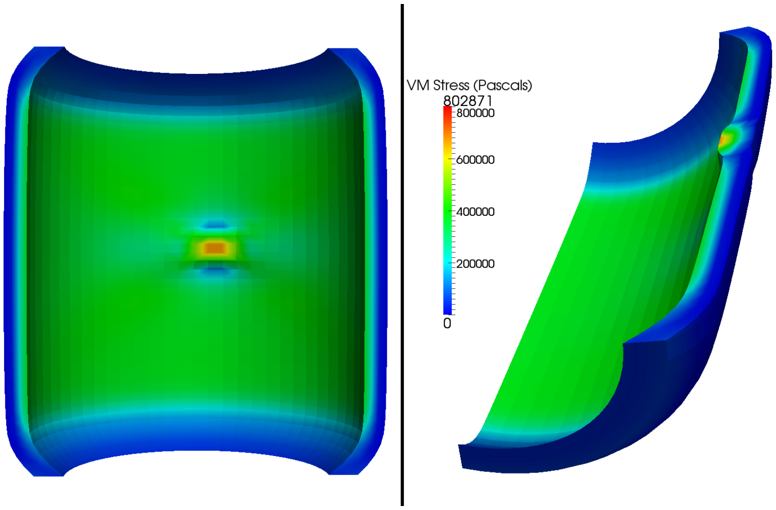

(b) t=2.8s

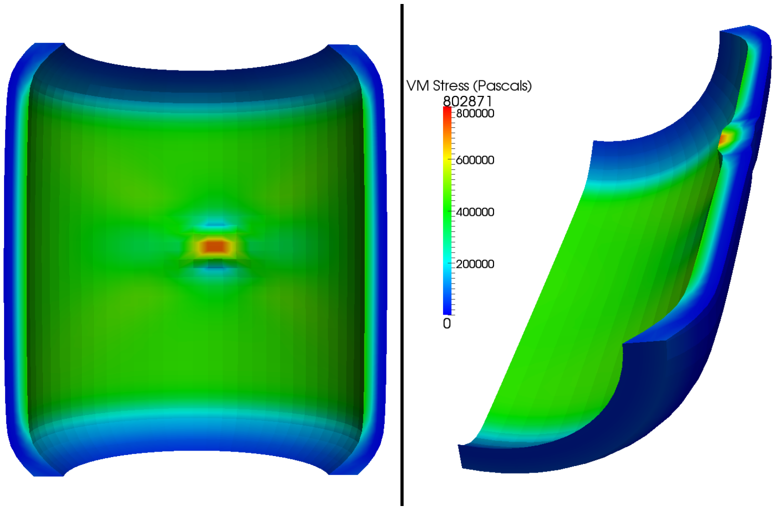

(c) t=3.2s

Figure 4.25: Spot-lesion inflation sequence - times (2.4s-3.2s)

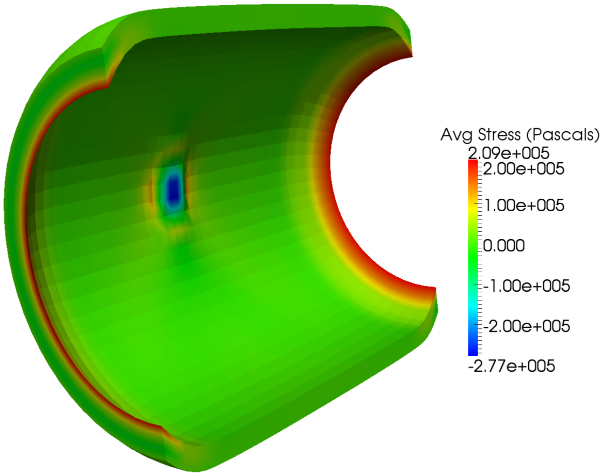

(a) σ_{rr}

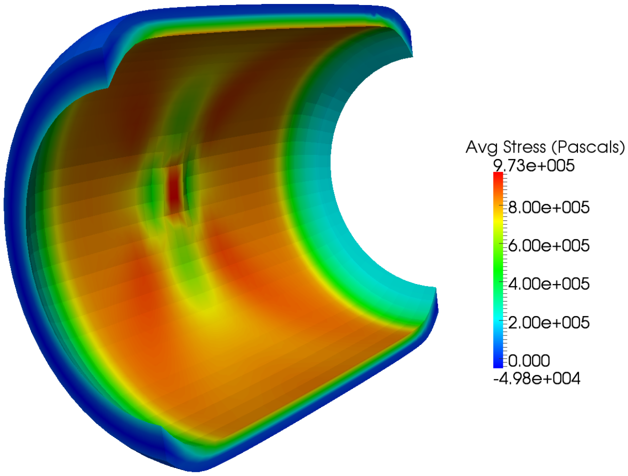

(b) $\sigma_{\theta\theta}$

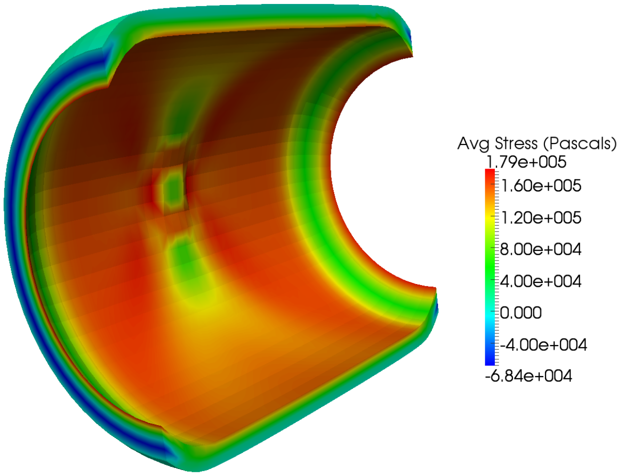

(c) σ_{zz}

Figure 4.26: Spot-lesion, inflation, extension principal stresses (σ_{rr},$\sigma_{\theta\theta}$,σ_{zz})

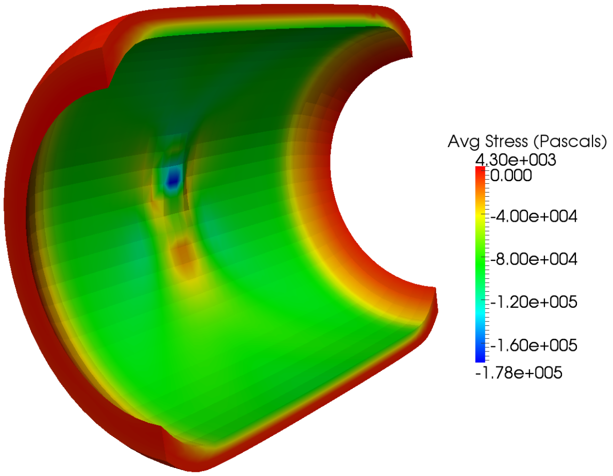

(a) $\sigma_{r\theta}$

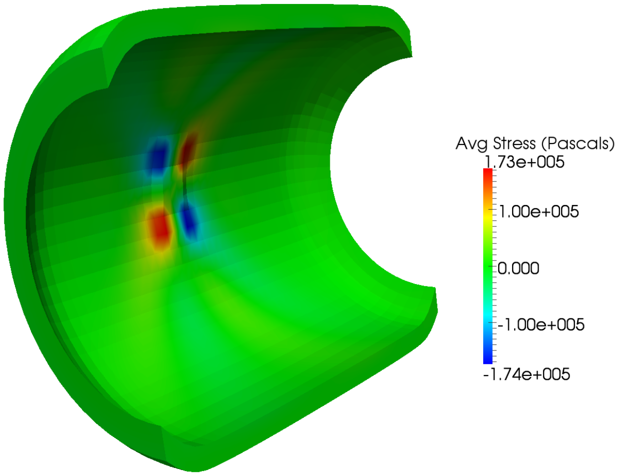

(b) $\sigma_{\theta z}$

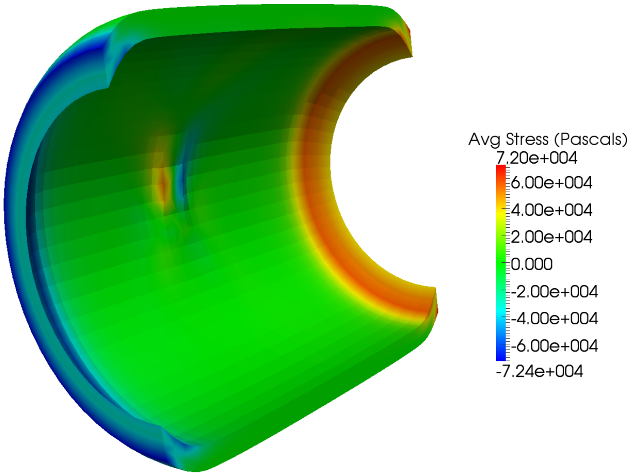

(c) σ_{rz}

Figure 4.27: Spot-lesion, inflation, extension shear stresses ($\sigma_{r\theta}$,$\sigma_{\theta z}$,σ_{rz})

Chapter 5

Discussion

5.1 Conclusions on the 2D Membrane Formulation of the Arterial Wall

We have shown that modeling the arterial wall as a two-dimensional membrane has the following benefits: 1. evaluating, in a relatively simple numerical setting, the performance of various 2D strain energy functions, 2. predicting the overall volume change given prescribed axial stretch and internal pressure (and the rates for each), and 3. exposing the influence of local material inhomogeneities on the overall deformation of the vessel.

Perhaps the most useful outcome of this portion of the study is the apparent viscoelastic behavior of the artery. As the artery is quickly stretched, then quickly inflated, the deformation is extremely acute in the regions of higher strain (the end being pulled). This bulge eventually evens out and the vessel retains a symmetric equilibrium state if the pressure is held constant, but if the pressure continually increases the artery will likely rupture at this location.

5.2 Conclusions on the 3D Finite Element Formulation of the Arterial Wall

In the absence of material lesions, the artery was shown to carry the majority of the strain, therefore stress, in the medial layer. Under pure axial stretch, the stress fields in the adventitia are constant along the segment length, whereas in the media, there is a significant gradient. For extension and internal pressure, the adventitia contributes to the load sharing more, although the majority of it is still in the medial layer.

The presence of local material lesions was shown to affect the strain, thereby stress, fields through both layers of the arterial wall under these boundary conditions. It was shown that a stiff ring-type lesion served to stabilize the radial deformation of the artery, although the stresses through the wall thickness were much higher. For a softer lesion, the stress fields appeared identical to those in the absence of a material lesion - hence the omission from including these plots in the Results. For stiff, spot-like lesions, the vessel behavior is considerably distorted. The protrusion of the stiff spot-like lesion into the vessel interior would reasonably lead to irregular blood flow at the tissue surface, subsequent irregular shear stress and resulting tissue growth and remodeling. The stress contour shows the Von Mises stress is on the order of two times higher in the lesion than the tissue surrounding it. It then increases again further from the abnormality. Clearly the acute gradients in stress could reasonably lead to irregular growth, remodeling or degradation of the vessel wall.

Bibliography

[1] G.A. Holzapfel, T.C. Gasser, and R.W. Ogden. A new constitutive framework for arterial wall mechanics and a comparative study of material models. *Journal of elasticity*, 61(1):1–48, 2000.

[2] D. Balzani, P. Neff, J. Schr
”oder, and GA Holzapfel. A polyconvex framework for soft biological tissues. Adjustment to experimental data. *International Journal of Solids and Structures*, 43(20):6052–6070, 2006.

[3] J.D. Humphrey. Mechanics of the arterial wall: review and directions. *Critical reviews in biomedical engineering*, 23(1-2):1–162, 1995.

[4] H. Gray. *Anatomy of the human body*. Lea & Febiger, 1918.

[5] A. Delfino, N. Stergiopulos, JE Moore, et al. Residual strain effects on the stress field in a thick wall finite element model of the human carotid bifurcation. *Journal of Biomechanics*, 30(8):777–786, 1997.

[6] J.P. Vande Geest, M.S. Sacks, and D.A. Vorp. The effects of aneurysm on the biaxial mechanical behavior of human abdominal aorta. *Journal of biomechanics*, 39(7):1324–1334, 2006.

[7] CJ Chuong and YC Fung. Compressibility and constitutive equation of arterial wall in radial compression experiments. *Journal of biomechanics*, 17(1):35–40, 1984.

[8] G.A. Holzapfel and H.W. Weizs
”acker. Biomechanical behavior of the arterial wall and its numerical characterization. *Computers in biology and medicine*, 28(4):377–392, 1998.

[9] C.S. Roy. The elastic properties of the arterial wall. *The Journal of Physiology*, 3(2):125, 1881.

[10] DC McGiffin, PB McGiffin, AJ Galbraith, and RB Cross. Aortic wall stress profile after repair of coarctation of the aorta. It is related to subsequent

true aneurysm formation? *The Journal of Thoracic and Cardiovascular Surgery*, 104(4):924, 1992.

[11] W.A. Marston, E. Criado, C.A. Baird, and B.A. Keagy. Reduction of aneurysm pressure and wall stress after endovascular repair of abdominal aortic aneurysm in a canine model. *Annals of vascular surgery*, 10(2):166–173, 1996.

[12] DF Elger, DM Blackketter, RS Budwig, and KH Johansen. The influence of shape on the stresses in model abdominal aortic aneurysms. *Journal of biomechanical engineering*, 118:326, 1996.

[13] YB Fu, SP Pearce, and KK Liu. Post-bifurcation analysis of a thin-walled hyperelastic tube under inflation. *International Journal of Non-Linear Mechanics*, 43(8):697–706, 2008.

[14] E. Di Martino, S. Mantero, F. Inzoli, G. Melissano, D. Astore, R. Chiesa, and R. Fumero. Biomechanics of abdominal aortic aneurysm in the presence of endoluminal thrombus: experimental characterisation and structural static computational analysis. *European Journal of Vascular and Endovascular Surgery*, 15(4):290–299, 1998.

[15] D.H.J. Wang, M.S. Makaroun, M.W. Webster, and D.A. Vorp. Effect of intraluminal thrombus on wall stress in patient-specific models of abdominal aortic aneurysm. *Journal of Vascular Surgery*, 36(3):598–604, 2002.

[16] M.M. Stringfellow, P.F. Lawrence, and R.G. Stringfellow. The influence of aorta-aneurysm geometry upon stress in the aneurysm wall. *Journal of Surgical Research*, 42(4):425–433, 1987.

[17] F. Inzoli, F. Boschetti, M. Zappa, T. Longo, and R. Fumero. Biomechanical factors in abdominal aortic aneurysm rupture. *European Journal of Vascular Surgery*, 7(6):667–674, 1993.

[18] D.A. Vorp, ML Raghavan, and M.W. Webster. Mechanical wall stress in abdominal aortic aneurysm: influence of diameter and asymmetry. *Journal of Vascular Surgery*, 27(4):632–639, 1998.

[19] W.R. Mower, L.J. Baraff, and J. Sneyd. Stress distributions in vascular aneurysms: factors affecting risk of aneurysm rupture. *Journal of Surgical Research*, 55(2):155–161, 1993.

[20] C.M. He and M.R. Roach. The composition and mechanical properties of abdominal aortic aneurysms. *Journal of vascular surgery*, 20(1):6–13, 1994.

[21] ML Raghavan, M.W. Webster, and D.A. Vorp. Ex vivo biomechanical behavior of abdominal aortic aneurysm: assessment using a new mathematical model. *Annals of biomedical engineering*, 24(5):573–582, 1996.

[22] M.F. Fillinger, ML Raghavan, S.P. Marra, J.L. Cronenwett, and F.E. Kennedy. In vivo analysis of mechanical wall stress and abdominal aortic aneurysm rupture risk. *Journal of Vascular Surgery*, 36(3):589–597, 2002.

[23] M.L. Raghavan, M.F. Fillinger, S.P. Marra, B.P. Naegelein, and F.E. Kennedy. Automated methodology for determination of stress distribution in human abdominal aortic aneurysm. *Journal of biomechanical engineering*, 127:868, 2005.

[24] CJ Chuong and YC Fung. On residual stresses in arteries. *Journal of Biomechanical Engineering*, 108:189, 1986.

[25] JP Boehler. Introduction to the invariant formulation of anisotropic constitutive equations. *Application of Tensor Functions in Solid Mechanics, CISM Courses and Lectures*, 292:13–64, 1987.

[26] J. Schröder and P. Neff. Construction of polyconvex, anisotropic free-energy functions. *PAMM*, 2(1):172–173, 2003.

[27] WW Nichols, MF O'rourke, and W.L. Kenney. McDonald's Blood Flow in Arteries: Theoretical, Experimental and Clinical Principles, ed. 3. *Journal of Cardiopulmonary Rehabilitation and Prevention*, 11(6341):407, 1991.

[28] J.D. Humphrey. *Cardiovascular solid mechanics: cells, tissues, and organs*. Springer Verlag, 2002.

[29] Y.C. Fung. *Biomechanics: mechanical properties of living tissues*. Springer, 1993.

[30] J.A.G. Rhodin. Architecture of the vessel wall. *Handbook of physiology: a critical, comprehensive presentation of physiological knowledge and concepts. The cardiovascular system: Formerly Section 2: Circulation Vascular smooth muscle*, page 1, 1980.

[31] YC Fung. Elasticity of soft tissues in simple elongation. *American Journal of Physiology*, 213(6):1532, 1967.

[32] R.N. Vaishnav, J.T. Young, J.S. Janicki, and D.J. Patel. Nonlinear anisotropic elastic properties of the canine aorta. *Biophysical Journal*, 12(8):1008–1027, 1972.

[33] R.P. Vito. The mechanical properties of soft tissues–I: A mechanical system for bi-axial testing. *Journal of Biomechanics*, 13(11):947–950, 1980.

[34] D.A. Vorp, KR Rajagopal, P.J. Smolinski, and H.S. Borovetz. Identification of elastic properties of homogeneous, orthotropic vascular segments in distension. *Journal of biomechanics*, 28(5):501–512, 1995.

[35] R. Busse, RD Bauer, T. Sattler, and A. Schabert. Dependence of elastic and viscous properties of elastic arteries on circumferential wall stress at two different smooth muscle tones. *Pfl
"ugers Archiv European Journal of Physiology*, 390(2):113–119, 1981.

[36] D.J. Steigmann. A Concise Derivation of Membrane Theory from Three-Dimensional Nonlinear Elasticity. *Journal of Elasticity*, 97(1):97–101, 2009.

[37] RW Ogden. *Non-linear elastic deformations*. Dover Pubns, 1997.

[38] CO Horgan and G. Saccomandi. A description of arterial wall mechanics using limiting chain extensibility constitutive models. *Biomechanics and modeling in mechanobiology*, 1(4):251–266, 2003.

[39] BR Simon, MV Kaufmann, MA McAfee, and AL Baldwin. Finite element models for arterial wall mechanics. *Journal of biomechanical engineering*, 115:489, 1993.

[40] T. Belytschko, W.K. Liu, and B. Moran. *Nonlinear finite element analysis for continua and structures*. Wiley New York, 2000.

[41] P.G. Ciarlet. *Mathematical elasticity: three-dimensional elasticity*. North Holland, 1988.

[42] G.A. Holzapfel. *Nonlinear solid mechanics*. Wiley New York, 2000.

[43] N. Stergiopulos, S. Vulliemoz, A. Rachev, J.J. Meister, and SE Greenwald. Assessing the homogeneity of the elastic properties and composition of the pig aortic media. *Journal of vascular research*, 38(3):237–246, 2000.

[44] D.J. PATEL and D.L. FRY. The elastic symmetry of arterial segments in dogs. *Circulation Research*, 24(1):1, 1969.

[45] ML Raghavan and DA Vorp. Toward a biomechanical tool to evaluate rupture potential of abdominal aortic aneurysm: identification of a finite strain constitutive model and evaluation of its applicability. *Journal of biomechanics*, 33(4):475, 2000.

[46] DCD Speirs, EA de Souza Neto, and D. Perić. An approach to the mechanical constitutive modelling of arterial tissue based on homogenization and optimization. *Journal of biomechanics*, 41(12):2673–2680, 2008.

[47] M.A. Zulliger, P. Fridez, K. Hayashi, and N. Stergiopulos. A strain energy function for arteries accounting for wall composition and structure. *Journal of biomechanics*, 37(7):989–1000, 2004.

[48] G.A. Holzapfel. Computational biomechanics of soft biological tissue. *Encyclopedia of computational mechanics*, 2:605–635, 2004.

[49] K. Takamizawa and K. Hayashi. Strain energy density function and uniform strain hypothesis for arterial mechanics. *Journal of biomechanics*, 20(1):7–17, 1987.

[50] R.N. Vaishnav and J. Vossoughi. Estimation of residual strains in aortic segments. In *Biomedical Engineering II: Recent Developments: Proceedings of the Second Southern Biomedical Engineering Conference*, pages 330–333, 1983.

[51] I. Masson, P. Boutouyrie, S. Laurent, J.D. Humphrey, and M. Zidi. Characterization of arterial wall mechanical behavior and stresses from human clinical data. *Journal of biomechanics*, 41(12):2618–2627, 2008.

[52] J. Vossoughi, Z. Hedjazi, and FS Borris. Intimal residual stress and strain in large arteries. *ASME-PUBLICATIONS-BED*, 24:434–434, 1993.

[53] SE Greenwald, JE Moore Jr, A. Rachev, TPC Kane, and J.J. Meister. Experimental investigation of the distribution of residual strains in the artery wall. *Journal of biomechanical engineering*, 119:438, 1997.

[54] L.A. Taber and J.D. Humphrey. Stress-modulated growth, residual stress, and vascular heterogeneity. *Journal of biomechanical engineering*, 123:528, 2001.

[55] T. Matsumoto and K. Hayashi. Stress and strain distribution in hypertensive and normotensive rat aorta considering residual strain. *Journal of biomechanical engineering*, 118:62, 1996.

[56] JD Humphrey and CA Taylor. Intracranial and abdominal aortic aneurysms: similarities, differences, and need for a new class of computational models. 2008.

[57] YC Fung, K. Fronek, and P. Patitucci. Pseudoelasticity of arteries and the choice of its mathematical expression. *American Journal of Physiology- Heart and Circulatory Physiology*, 237(5):H620, 1979.

[58] SX Deng, J. Tomioka, JC Debes, and YC Fung. New experiments on shear modulus of elasticity of arteries. *American Journal of Physiology- Heart and Circulatory Physiology*, 266(1):H1, 1994.

[59] J.M. Ball. Convexity conditions and existence theorems in nonlinear elasticity. *Archive for rational mechanics and Analysis*, 63(4):337–403, 1976.

[60] M.R. Roach and A.C. Burton. The reason for the shape of the distensibility curves of arteries. *Canadian Journal of Physiology and Pharmacology*, 35(8):681–690, 1957.

[61] J. Schröder and P. Neff. Invariant formulation of hyperelastic transverse isotropy based on polyconvex free energy functions. *International Journal of Solids and Structures*, 40(2):401–445, 2003.

[62] C.B. Morrey. Quasi-convexity and the lower semicontinuity of multiple integrals. *Pacific J. Math*, 2(1):25–53, 1952.

[63] J. Schröder and P. Neff. Application of Polyconvex Anisotropic Free Energies to Soft Tissues. In *Contribution to the Fifth World Congress on Computational Mechanics (WCCM V) in Vienna, Austria, Eds.: HA Mang, FG Rammerstorfer, J. Eberhardsteiner*, 2002.

[64] G.A. Holzapfel and T.C. Gasser. Computational stress-deformation analysis of arterial walls including high-pressure response. *International journal of cardiology*, 116(1):78–85, 2007.